KU LEUVEN

ARENBERG DOCTORAL SCHOOL
Faculty of Engineering Technology

A self adaptive algorithm for accurate strain measurements using global digital image correlation

Lukas Wittevrongel

Supervisor:
Prof. dr. ir. D. Debruyne
Prof. dr. P. Lava, co-supervisor
Prof. dr. ir S.V. Lomov, co-supervisor

Dissertation presented in partial fulfillment of the requirements for the degree of Doctor in Engineering Technology

October 2015

A self adaptive algorithm for accurate strain measurements using global digital image correlation

Lukas WITTEVRONGEL

Examination committee:
Prof. dr. ir. R. Dewil, chair
Prof. dr. ir. D. Debruyne, supervisor
Prof. dr. P. Lava, co-supervisor
Prof. dr. ir S.V. Lomov, co-supervisor
Prof. dr. ir B. Van Bael
Prof. dr. ir D. Roose
Prof. dr. ir D. Moens
Dr. ing. S. Cooreman

Prof. dr. ir. J.P.M. Hoefnagels
(University of Technology Eindhoven)

Dissertation presented in partial
fulfillment of the requirements for
the degree of Doctor
in Engineering Technology

October 2015

Uitgegeven in eigen beheer, Lukas Wittevrongel, Gebroerders Desmetstraat 1, B-9000 Ghent (Belgium)

Voorwoord

We willen een zelf adaptief DIC algoritme ontwikkelen om onze meting betrouwbaarder en accurater te maken. Ik weet niet hoe of wat, maar dit zou zeer waardevol zijn.

Eén van de eerste zinnen die ik hoorde voor de start van dit doctoraat. Zonder te weten wat DIC of zelf adaptief nu eigenlijk echt inhoudt of hoe dit werkt, heb ik deze kans met beide handen gegrepen.

In eerste plaats wil ik dan ook mijn promotor en copromotor bedanken voor het geven van deze kans. Verder wil ik hen ook bedanken om mij in te wijden in de wondere wereld van de adaptieve eindige elementen en de digitale beeldcorrelatie. Dimitri en Pascal, Prof. Debruyne en Prof. Lava, bedankt.

Ik dank Prof. Lomov voor het aanvaarden van het promotorschap in de eerste fase van mijn doctoraat. Het is pas na de oprichting van de faculteit Engineering Technology dat Prof. Debruyne mijn hoofdpromotor is geworden.

Ik wil ook graag mijn juryleden Prof. Van Bael, Prof. Roose, Prof. Moens, Dr. Cooreman en Dr. Hoefnagels bedanken voor de tijd die zij in het werk investeerden.

Verder ben ik mijn andere collega's Kristof, Koen, Rico, Ruben, Andreas, Yueqi, Renaat en Michele dankbaar voor het verlichten van de dagtaak. De vaste ochtend meeting aan het koffieapparaat en de beruchte tafelvoetbal wedstrijden tijdens de middag zijn intussen bijna rituelen geworden die ik hard zal missen. Ook de afsluiters op vrijdagavond hoorden er natuurlijk bij!

In het bijzonder wil ik mijn bureaugenoot, Kristof, nog eens extra bedanken voor de leuke werksfeer. Dankzij de 24/24u muziek van DJ Denys en Wittevrongel was het altijd feest op bureau. Ook voor de uren die we samen starend naar ons whiteboard en computerscherm hebben doorgebracht in de hoop een probleem op te lossen, heeft vaak tot de juiste inzichten geleid! Kristof, bedankt.

Ook gaat dank uit naar Prof. Van Achter voor de vele tips en tricks om de Engelse schrijfstijl te verfijnen.

Uiteraard dank ik ook het IWT, agentschap voor innovatie door wetenschap en techniek, voor het toekennen van mijn doctoraatsbeurs. Ook al was het als start van het doctoraat een serieuze horde om te nemen en heeft het me meer dan genoeg stress bezorgd, door jullie financiële steun is dit project tot een goed einde gebracht.

Naast deze professionele werkomgeving, wens ik ook nog enkele andere mensen te bedanken.

Mijn allergrootste dankbetuiging gaat uit naar Hanne. Bedankt voor de onvoorwaardelijke liefde en steun, voor het urenlang luisteren naar gepraat over dit onderzoek, maar ook voor het op tijd afleiden van mijn aandacht. Verder ook heel erg bedankt voor de uren nalezen en verbeteren van papers, abstracts en zelfs deze thesis.

Ook aan papa, moeke en broer. Bedankt om mij te steunen en sturen in deze fase van mijn leven. Jullie steun en hulp waren van onschatbare waarde.

Kwinten en Ruben, ook jullie dank ik. Met twee goede vrienden uit de studententijd kunnen doorgroeien tot collega's is ideaal om zowel serieuze als minder serieuze gesprekken en pauzes te hebben.

Ook mijn andere vrienden en familie wil ik van harte bedanken. Dankzij het sporten, de spelletjes avonden, feestjes en andere kon ik telkens nieuwe energie vinden om door te gaan.

Ik wil ook mijn grootvader vermelden als inspiratiebron. Je was zelf de meester in filosoferen en raadsels ontwikkelen. Graag had ik je nog in levende lijve laten zien dat ik eindelijk dit raadsel heb opgelost. In gedachten ben je nog steeds bij ons.

Lukas, 1 oktober 2015

Abstract

Intro Digital image correlation (DIC) is an optical-numerical technique that allows to determine full-field deformation data on the surface of an object. The deformation is obtained by using digital images of the surface, taken before and after deformation. When assuming the conservation of optical flow between both images, the deformation can be determined by comparing the gray value patterns of both images. The major advantage of this technique is its flexibility. A standard CCD camera can be used for the image registration while the test can be done both in a lab as on-site. If required, the standard CCD can be replaced with high speed cameras or even microscopes. Furthermore, the technique can be used on any arbitrary material (e.g. steel, rubber, wood, composites, ..) under arbitrary loading conditions (e.g. mechanical, thermal, electrical, ..).

Why In the traditional approach of DIC, the deformation of the surface is determined by tracking each pixel from the reference to the deformed image. To this purpose, a certain amount of information is required as the gray value of a pixel itself is not unique between two images. The information for locating the pixel is found in the so-called subsets, a group of pixels surrounding the considered pixel, hence the name: "subset method". An important drawback of this traditional (local) technique is the non-continuity of the displacement field, as the displacement of the pixels is sought separately and thus does not take any connectivity between pixels into account. This independent approach influences the calculation of the strains, as smoothing in the noisy displacement field is essential to obtain acceptable strain results. For the strain calculation usually a local polynomial smoothing is applied, where a rectangular area denoted as strain window is used. The extent of smoothing is controlled by the subset size, step size and strain window size. Therefore, the measurement of small and complex strains become cumbersome because the final result will be significantly influenced by these user-dependent parameters. To prevent the non continuity of the displacement field, a global DIC approach is developed. Compared to the traditional method, where pixels are individually tracked, the proposed method uses a global approach where all pixels within the test object are tracked simultaneously. Instead of tracking subsets, a complete finite element mesh is tracked. By using a finite element mesh in the correlation, a continuous displacement field is obtained where the strains can be calculated directly from the algorithm without any extra smoothing. The mentioned global method however, still suffers from the user dependency as the size of the elements within the mesh will heavily influence the results.

How To avoid the user dependency of results, the aim of this work is to make the global approach adaptive and automatic. To achieve these results, features from adaptive FEA are transferred to the DIC approach. First, an adaptive algorithm is needed. This is done by implementing p-elements into the finite element mesh. In this way, elements in the mesh can increase their degrees of freedom if they are not capable of representing the actual deformation field. The p-elements are implemented using hierarchical functions in order to make the procedure more effective. Secondly, the procedure is made automatic. The principle of convergence in "strain energy" is introduced to the global DIC method for controlling the mesh refinement procedure. Using both principles, an automatic adaptive global DIC procedure is achieved, capable of determining an optimal non-uniform mesh without any preknowledge of the deformation field. Because of the p-refinement, this method is denoted as p-DIC. This is in great contrast to current global DIC, where the mesh is refined in places where heterogeneity is expected by the user.

Results From an extensive validation, it is seen that the p-DIC method has a lower displacement resolution (noise floor) for the same spatial resolution (complexity of deformation) compared to the local method. From the strain validation, it can also be concluded that for the accurate measurement of high gradient strain fields the p-DIC method is more favourable than the local method. Besides the advantage in resolution at a certain spatial resolution, the adaptive method turns out to become user independent to a large extent.

Complementary In addition to the aforementioned work, the influence of strain continuity on the global DIC approach has been investigated. Although the influence of continuity in the deformation field has shown to be minimal, it can be a major advantage when specific continuous deformation fields are requested (e.g. flux calculations, curvature, ...). As a final part of this thesis, solutions are provided to solve the largest experimental influence on 2D DIC measurements. Compensation methods towards out-of-plane motions are implemented and compared both numerically and experimentally.

Beknopte samenvatting

Introductie Digitale beeldcorrelatie is een optisch-numerieke meetmethode die toelaat om de volledige vervorming van het oppervlak van een object te meten. De vervorming wordt bepaald door gebruik te maken van digitale beelden, genomen voor en na vervorming. Wanneer er wordt uitgaan van behoud van *optical flow*, dan kan de vervorming bepaald worden door het vergelijken van patronen met grijswaarde komende van beide beelden. Het grootste voordeel van deze techniek is zijn flexibiliteit. Een standaard CCD camera kan gebruikt worden voor het maken van de digitale beelden en het experiment kan zowel in het lab als op de werkvloer uitgevoerd worden. Verder kan de techniek gebruikt worden op ender welk materiaal (bv. staal, rubber, hout, composiet, ...) onder arbitraire belastingsomstandigheden (bv. mechanisch, thermisch, elektrisch,...).

Waarom In de traditionele digitale beeldcorrelatie wordt de vervorming van het oppervlak gevonden door iedere pixel van de referentie foto te traceren naar de vervormde foto. Aangezien een pixel op zich niet uniek is, is er meer informatie nodig om de traceerbaarheid van een pixel te garanderen. Deze informatie wordt gevonden in de zogenaamde *subset*, namelijk een groep van pixels rondom de gezochte pixel. Vandaar de benaming *subset-methode*. Een belangrijk nadeel van deze traditionele (lokale) methode is het niet-continue verplaatsingsveld van de pixels aangezien deze onafhankelijk van elkaar gezocht worden en dus geen connectiviteit tussen pixels in rekening is gebracht. Deze onafhankelijke aanpak heeft zijn gevolgen op de berekening van de rekken aangezien uitmiddeling van het niet-continue verplaatingsveld nodig is om aanvaardbare resultaten te verkrijgen. Om de rekken aan het oppervlak te berekenen wordt meestal gebruik gemaakt van lokale polynomische uitmiddeling met behulp van een vierkant oppervlak genaamd rekvenster. De hoeveelheid uitmiddelen wordt gecontroleerd door de grootte van de subset, stap en rekvenster. Het meten van kleine en complexe rekken wordt hierdoor zeer moeilijk aangezien de resultaten zeer afhankelijk zijn van de uitmiddeling en dus van de gebruikers afhankelijke instellingen. De niet-continuïteit van het verplaatsingsveld kan vermeden worden door gebruik te maken van de globale methode. In vergelijking met de lokale

methode, waar iedere pixel apart gezocht werd, zullen in de globale methode alle pixels tegelijkertijd gevolgd worden. In plaats van aparte subsets zal hier een net van eindige elementen beschouwd worden. Hierdoor wordt een continu verplaatsings veld verkregen en kunnen de rekken direct afgeleid worden uit het verplaatsingsveld, zonder enige uitmiddeling. Deze globale methode is echter nog steeds afhankelijk van de input van de gebruiker aangezien de grootte van de gekozen elementen de resultaten aanzienlijk zullen beinvloeden.

Hoe Het doel van dit werk is het minimaliseren van de invloed van de gebruikte instellingen op de resultaten door de globale methode adaptief en automatisch te maken. Om dit te verkrijgen zijn principes vanuit de adaptieve eindige elementen analyse geïmplementeerd in de DIC analyse. De eerste stap is het ontwikkelen van een adaptief algorithme. Hiervoor werd het principe van zogenaamde p-elementen geïmplementeerd in het eindige element net. Deze elementen kunnen stijgen in polynomische orde wanneer zij niet in staat zijn om de verplaatsing te beschrijven. De p-elementen zijn geïmplementeerd met behulp van hïerarchische functies om de DIC procedure efficïenter te maken. Vervolgens, moet de methode zelf adaptief worden. Het principe van convergentie in rek energie vanuit de EEA is geintroduceerd in DIC om het aanpassen van het net te sturen. Door gebruik te maken van deze twee principes is een zelf-adaptieve globale DIC procedure ontwikkeld die in staat is om het meest optimale net te bepalen zonder enige voorkennis van de gezochte oplossing. De methode wordt p-DIC genoemd. Dit is in groot contrast met de huidige global methode waar het net aangepast wordt door de verwachtingen van de gebruiker.

Resultaten Uit een uitgebreide validatie is gebleken dat de p-DIC methode, in vergelijking met de lokale methode, een lagere verplaatsingsresolutie (ruisniveau) heeft voor dezelfde ruimtelijke resolutie (complexiteit van de vervorming). Uit de validatie van de rek kan hetzelfde besluit getrokken worden, namelijk dat voor het accuraat meten van complexe rekken de p-DIC methode te verkiezen is boven de lokale methode. Naast het voordeel in meetresolutie is ook aangetoond dat de p-DIC methode veel minder gebruikersafhankelijk is.

Extra Naast het ontwikkelen van p-DIC werd ook de invloed van rek continuïteit in DIC onderzocht. Al blijkt rek continuïteit niet veel invloed te hebben op de meetresoluties, kan het een grote meerwaarde hebben bij toepassingen waar expliciet een continu rekveld nodig is (bv. magnetisme berekeningen, krommingen, ...). Tot slot werden in dit werk werden oplossingen aangereikt om de grootste experimentele invloed op de resultaten te minimaliseren. Compensatie methoden voor *out of plane* bewegingen zijn geïmplementeerd en gevalideerd in zowel numerieke als experimentele testen.

Abbreviations

CC	Cross Correlation
CCD	Charge-coupled Device
CMOS	Complementary Metal Oxide Semiconductor
DIC	Digital Image Correlation
DOF	Degree Of Freedom
FE-DIC	Finite Element based Digital Image Correlation
FEA	Finite Element Analysis
FEMU	Finite Element Model Updating
FOV	Field of View
HW	Hardware
NCC	Normalised Cross Correlation
NSSD	Normalised Sum of Squared Differences
OPM	Out-of-Plane Motion
Q4	4 node linear element
Q8	8 node quadratic element
RMS	Root Mean Square
ROC	Region Of Compensation
ROI	Region Of Interest
SS	Subset Size
SSD	Sum of Squared Differences
SW	Software
SW	Strain Window

VFM	Virtual Fields Method
VSG	Virtual Strain Gauge
ZNCC	Zero Normalised Cross Correlation
ZNSSD	Zero Normalised Sum of Squared Differences
ZOI	Zone Of Interest

List of Symbols

(ξ, η)	Local (natural) element coordinate
(x, y)	Global (image) coordinate
α	Allowed reconstruction error
$\approx$	Approximately
$\Delta(\bullet)$	Variation
Δ	Complete mesh
δ	Shape function parameter
$\epsilon_{Artificial_\alpha}$	Artifical strain in direction α due to out of plane motion in 2D
η	Element displacement error indicator
$\frac{\delta(\bullet)}{\delta(a)}$	Partial derivative to a
γ_0, γ_1	Stereo camera twist angles
$\hat{u}$	Discretised displacement
$\iint \bullet$	Double integration
$\in$	Element of
$\kappa_{x,y,z}$	Camera radial distortion parameters
$\mathbf{d}$	Displacement vector (u,v)
$\mathbf{e}_a$	Unit vector direction a
$\mathbf{x}$	Global (image) coordinate (x,y)
∇_a	Partial derivative to a

Ω	Element domain
$\overline{\Delta u}_g$	Global average
$\overline{\Delta u}_y$	Directional average
$\| \bullet \|$	Norm of a tensor
Φ	Shape function
Φ_D	Imposed displacement field
σ_g	Global standard deviation
σ_y	Directional standard deviation
$\sum_a$	Summation over a
$\sum_{a,b}$	$\sum_a \sum_b$
θ_0, θ_1	Stereo camera pan angles
ζ	Material coordinate
$A \xrightarrow{C} B$	From A to B in steps of C
$c_{x,y}$	Image plane sensor location
$det(\bullet)$	Determinant
e	Local displacement error
e'	Approximated local displacement error
E_i	Edge function for edge i
E_ε^e	Element e L2-norm in strain field.
E_ε^g	Global L2-norm in strain field.
E_u^e	Element e L2-norm in displacement field.
E_u^g	Global L2-norm in displacement field.
F	Deformation gradient
f	Reference image
F^e	Correlation matrix F for element e
F^s	System correlation matrix F

$f_{x,y,z}$	Camera focal lengths
G	Displacement gradient
g	Deformed image
h	Highest order shape functions
I	Identity matrix
J	Jacobian of the mapping system
K^e	Correlation matrix K for element e
K^s	System correlation matrix K
L	Vandermonde matrix
n	Number degrees of freedom
p	Polynomial order
$R(x)$	Reconstructed 1D deformation
r_{SSD}	SSD cost function
RMS_g	Global root mean square
$T_{x,y,z}$	Camera position parameters
u	Global horizontal displacement
v	Global vertical displacement
$X^e(\xi, \eta)$	Local to global mapping function for element e
z	Distance between camera and specimen
$[\bullet]^T$	Transpose of a tensor
$[\bullet]^{-1}$	Inverse of a tensor

Contents

List of Figures

List of Tables

Chapter 1

Introduction

This chapter introduces the thesis by highlighting the subject, the motivation and the objectives. It also introduces the main contributions and the structure of this dissertation.

1.1 Motivation and novelty of this work

The problem statement of this work is illustrated using an example where the deformation of a composite is measured. Currently used digital image correlation algorithms are not self adaptive and thereby results can be very dependent on algorithmic settings used during the measurement. The user dependent settings become more important when the complexity of the deformation field increases. Because the deformations within composites are both very small and complex, measuring these deformations is cumbersome using current DIC techniques.

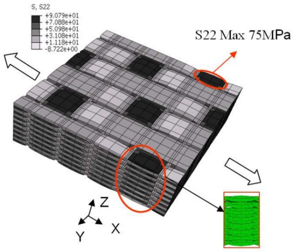

Figure 1.1: Finite element simulation of composite under tensile loading.

An example of the dependency of the results towards algorithmic settings is illustrated in Fig 1.2. Here the strain field of a carbon satin weave/PPS composite (See Fig 1.1) under tensile load is shown using different measurement settings. The images used for this example are obtained from a study by Lava et al. [6].

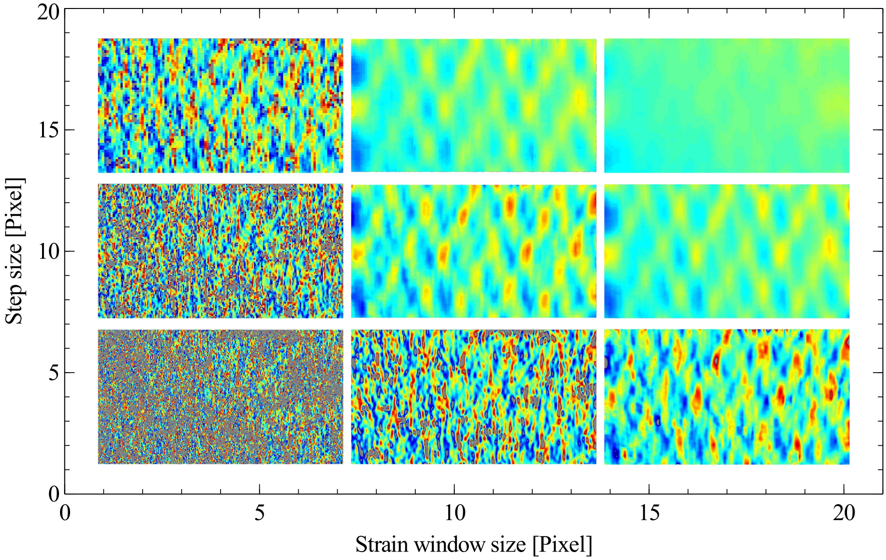

Figure 1.2: Strain Exx in composite using different combinations of algorithmic settings.

It is clearly seen that varying two measurement settings, the step size and strain windows, heavily influences the obtained strain field. The scope of this work is the development of a global self adaptive digital image correlation (DIC) algorithm to accurately measure complex deformation fields. The self adaptive algorithm is proposed to automatically adjust the initial user settings, to eventually obtain the *most beneficial* settings and so to measure the correct, independent, deformation fields. The novelty of this work lies in the development and implementation of an adaptive algorithm. The main requirements of the algorithm are:

- ✓ Provide a good trade-off between resolution and spatial resolution.
- ✓ Self adaptivity must be introduced to minimise user dependency.

During this work it will be shown how this approach is developed. What can be shown already is that the final results obtained are to a large extent user independent. The results of the example is shown for a wide range of possible user settings are shown in Fig 1.3.

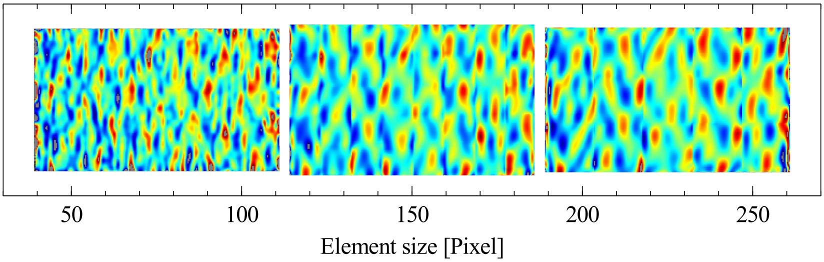

Figure 1.3: Strain Exx in composite using different initial algorithmic settings.

It is clearly seen that the results are less user dependent. The amount of user dependent settings has been reduced to one, being the element size. Furthermore, the influence of this user setting is reduced by the self adapting feature of the approach.

1.2 Objectives and original contributions

The main contributions of this work are:

- ✓ A novel adaptive digital image correlation algorithm is developed. It uses a finite element mesh to track the deformation between different images. Different from other global approaches, it uses p-elements, where the order can change during the correlation procedure. By increasing the element order instead of reducing the element size, which is common practice in FEA, several major advantages are obtained in comparison to the current global DIC methods. The method is introduced as p-DIC.
- ✓ Convergency procedures are introduced into DIC. In the past, assessment of the quality of the measurement was based on both user experience and mechanical preknowledge. With this knowledge, DIC parameters could be fine-tuned and accurate results could be obtained. Having enough user experience and mechanical preknowledge however is difficult to obtain. Convergence of *element energy* is introduced in the p-DIC algorithm to control mesh refinements and thereby to obtain more reliable and user-independent results. In this way, an automatic and self adapting algorithm is achieved and thus results become less user dependent.
- ✓ An in-depth validation is carried out to compare the introduced p-DIC algorithm towards the available algorithms. Because of the fundamental differences between the introduced algorithm and the traditional local DIC approach, an independent validation procedure is necessary. The validation introduces *methodologies* for determining displacement and spatial resolution independent of the used approach (local or global).
- ✓ The use of global DIC introduces C^0 continuity in the measured displacement field. In this work, the influence of C^1 continuity is evaluated. A novel C^1 continuous global approach is introduced and compared to the current local and global approaches. In this way a full comparison between no-, C^0- and C^1-continuity is provided.
- ✓ As a final part of this thesis, solutions are provided to solve the largest experimental error source in 2D DIC measurements. Compensation methods towards out-of-plane motions are implemented and compared both numerically and experimentally. By compensating out-of-plane motions, major improvements are achieved in the 2D DIC setup.

1.3 Structure of the thesis

The thesis is structured as follows:

Chapter 1 introduces the thesis and highlights the main objectives of the text.

Chapter 2 gives a brief overview of the used principles in the thesis. The concept of DIC is explained and local and global DIC introduced. Further, the basis of adaptive finite elements is explained.

Chapter 3 presents the mathematics and validation of the self adaptive digital image correlation algorithm.

Chapter 4 explains the implementation of FEA based convergence principles into the self adaptive global DIC aproach.

Chapter 5 investigates the potential of a C^1-continuous algorithm and compares it with the current local and global approaches.

Chapter 6 introduces the influence and possible compensation methods on out of plane motions.

Chapter 7 presents the conclusions made from this work and ideas regarding possible future works.

Chapter 2

State of the art

Chapter 2 gives a brief introduction to the DIC and the FEA method. First section introduces DIC and its different currently used approaches, while section 2 introduces the basic principles of adaptive finite element analysis.

2.1 Basic Concept of DIC

In DIC, the deformation is obtained by comparing the gray value patterns of digital images taken before and after deformation. Within the pattern, enough features have to be present to accurately determine the deformation. In this sense, DIC is a "pattern matching" algorithm where the movement of the pattern equals the measured deformation. For years, this method has been given different names such as digital speckle correlation method [7] or electronic speckle photography [8]. However, the most popular name for the method has remained DIC. The images used in DIC can be taken with classic CCD/CMOS cameras, but also with more sophisticated devices such as electron microscopes or X-ray imaging machines. When the surface itself possesses not enough features to track, an artificial speckle pattern can be applied. Such a pattern is mostly made by applying a white base coat and by introducing black speckles on the surface. The inverse (white on black) is also possible. Because almost always an artificial pattern is applied, the pattern on a surface will be called the speckle pattern. Fig 2.1 demonstrates a speckle pattern on a perforated specimen in its deformed and undeformed state.

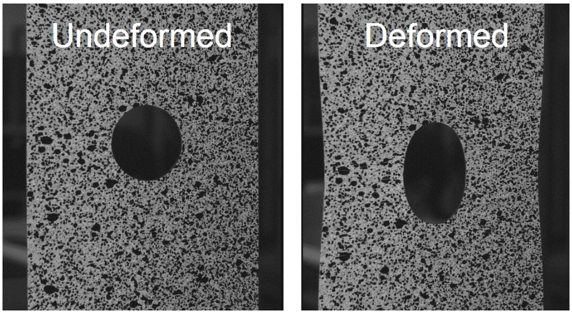

Figure 2.1: Speckle pattern on a perforated specimen before and after deformation.

Compared to other full-field measurement techniques, DIC has some specific advantages:

- Simple experimental setup: There are no specific preparations of the specimen needed. If the natural pattern is not sufficient, one can spray a pattern onto the surface using a spray can. Furthermore, in a 2D DIC setup only one CCD camera is needed.
- Robustness in environment: DIC is very suitable for both lab and field applications. Depending on the desired sensitivity, no special precautions should be made towards vibrations and a simple white light source or natural light is sufficient to perform measurements.
- Wide range of application: Since DIC only uses digital images, a wide range of applications is possible. The scale of the experiment can simply be modified by using different lenses on a standard CCD camera or by using specific imaging systems. To realise micro and nano scale measurements for example, DIC can be coupled with microscopes.

Because of this flexible and robust setup, DIC can be easily applied to different areas. The method's disadvantage however is that the measurements heavily depend on the quality of the imaging system.

Finding the deformation of a surface out of digital images is classified as an ill-posed inverse problem. The solution to this ill-posed problem can be found by assuming some unknown parameters, describing the deformation within a certain area (Zone of Interest, ZOI). The parameters act as degrees of freedom (DOF), allowing one of the images to deform to match the other image. The best match of the deformed ZOI with the reference ZOI is evaluated using a specific correlation function. A correlation function describes the remaining difference of the reference image *f(**x**)* and deformed image *g(**x**)*, using the identified deformation. The parameters for the deformation resulting in the smallest correlation function, are the optimal ones indicated as $p_{optimal}$. Defining $u(x;p)$ as the described deformation within the ZOI with parameters p and the correlation algorithm as the Sum of Squared Differences (SSD), the aforementioned procedure writes:

$$p_{optimal} = \arg\min_{p \in \Lambda} \{ \iint_{ZOI} ([f(\mathbf{x}) - g(\mathbf{x} + u(x;p))]^2) d\mathbf{x} \} \tag{2.1}$$

where Λ defines all admissible choices for p and $\mathbf{x} \in [x, y]$.

To tackle the problem of pattern matching, both a local or global approach can be used. The whole field of view to be measured will be denoted as ROI (Region of Interest). Within this ROI, a zone to match can be defined as ZOI. The difference between local and global approach is the assignment of the ZOI. In the following, both approaches are introduced.

2.1.1 Local DIC

Matching

The local method, also known as the subset method, is the most popular approach for DIC and is used in almost all commercial correlation software ([9, 10, 11, 12, 13]). In the subset method the ROI is covered by tracking each pixel within the ROI from the reference to the deformed image using a group of pixels surrounding the considered pixel (ZOI), also named the subset [1]. In this way, the ROI is discretised in multiple ZOIs. The images used in the correlation, representing the original and the deformed surface of the tested specimen, can be described by 2D functions *f(**x**)* and *g(**x**)*, defining the (interpolated) gray values at position ***x**=(x,y)*. The actual tracking of the subset from *f(**x**)* to *g(**x**)* is based on minimising a specific correlation function r (Eq. 2.2) indicating the difference of the subset between reference and deformed image [14]. If the subset is located in the deformed image, the displacement of the centre of the subset is determined as the displacement for that pixel (see Fig. 2.2).

Typical correlation functions are NSSD (Normalised Sum of Squared Differences) and ZNSSD (Zero Normalised Sum of Squared Differences) (equivalent to NCC and ZNCC [15]), described in Table 2.1. They are both used to cope with offset and scaling in light conditions [14]. To avoid complex mathematics, the subset

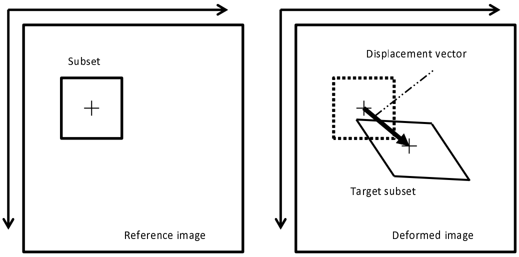

Figure 2.2: Principle of the subset-based DIC, tracking of a pixel from reference to deformed image.

method is illustrated here using the SSD (Sum of Squared Differences) r_{SSD},

$$r_{SSD} = \sum_x \sum_y (f[\mathbf{x}] - g[u(\mathbf{x};p), v(\mathbf{x}:p)])^2 \tag{2.2}$$

where $\sum_x \sum_y$ represents the summation of all pixels within the considered subset. For an affine subset [16], $u(\mathbf{x};p)$ and $v(\mathbf{x};p)$ are described by:

$$\begin{bmatrix} u(\mathbf{x};p) \\ v(\mathbf{x};p) \end{bmatrix} = \begin{bmatrix} x \\ y \end{bmatrix} + \begin{bmatrix} u \\ v \end{bmatrix} + \begin{bmatrix} \frac{\delta u}{\delta x} & \frac{\delta u}{\delta y} \\ \frac{\delta v}{\delta x} & \frac{\delta v}{\delta y} \end{bmatrix} \begin{bmatrix} \Delta x \\ \Delta y \end{bmatrix} \tag{2.3}$$

where Δx and Δx represent the distance to the subset center and with

$$s = \begin{bmatrix} u & v & \frac{\delta u}{\delta x} & \frac{\delta u}{\delta y} & \frac{\delta v}{\delta x} & \frac{\delta v}{\delta y} \end{bmatrix} \tag{2.4}$$

An affine subset accounts for translation, rotation and shear. The degree of freedom of the subset can be increased to irregular and quadratic deformations by expanding $u(\mathbf{x};p)$, $v(\mathbf{x};p)$ and s with second order derivatives of u and v [17]. It is worth noting that the displacement is most accurately known at the centres of calculated subsets, separated by the step, leading to a sparse set of data points and the lack of information around the edges, as a distance of half a subset of the pixel towards the edge needs to be preserved. Increasing the density of data is possible by decreasing the step size (e.g. 1) resulting however in a significantly longer calculation time.

Strain Calculation

An important drawback of the subset-based technique is the non-continuity of the displacement field, as the deformation of the subsets are optimised separately and thus no interconnectivity is taken into account. For the strain calculation usually a local polynomial smoothing is used, as smoothing in the biased and noisy displacement field is essential to obtain acceptable strain results [18, 19, 20]. In local polynomial smoothing, a polynomial function is fitted in the displacements of the subset and its neighbouring subsets. This function is then used to get the derived displacement fields. The amount of neighbouring subsets used in the smoothing is denoted by the strain window size. In the end, the extent of smoothing is controlled by the subset size, step size and strain window size.

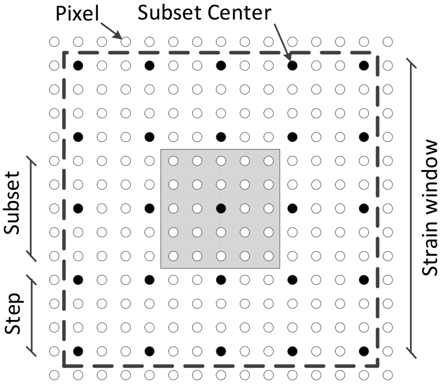

Figure 2.3: Visualisation subset size, step size and strain window size.

In Fig 2.3 the subset size (SS) is 5, the step (ST) is 3 and the strain window (SW) equals 5. If the strain window is identified by the grid of data points, then the strain can be linked to a Virtual Strain Gauge (VSG), representing the actual area of smoothing. The VSG is defined as:

$$VSG = ST(SW - 1) + 1 \tag{2.5}$$

2.1.2 Global DIC

Matching

An alternative approach to the traditional DIC approach is the global DIC method. Compared to the subset method, where pixels are tracked individually, the global method tracks all pixels within the test object simultaneously. In this way, the ZOI becomes the ROI. This method was initially proposed by Cheng et al. [21]. Later, Besnard et al. developed the FE-DIC [22], where a fixed bilinear (Q4) or quadratic (Q8) mesh is implemented. FE-DIC is probably the best known implementation of Global DIC. In the following the principle of FE-DIC is presented. The images used in the correlation are again represented by *f(**x**)* and *g(**x**)*. Using the conservation of optical flow, the problem can be described as determining $\mathbf{d}$, the unknown displacement field for an element Ω_e, so that for each point $\mathbf{x}$ element of Ω_e:

$$f(\mathbf{x}-\mathbf{d}) = g(\mathbf{x}) \tag{2.6}$$

Eq. 2.6 is valid if no external influences such as light conditions, noise or other external parameters are considered. Because these influences do act upon the images, specific cost functions are used to minimise the difference between $f(\mathbf{x}-d)$ and $g(\mathbf{x})$. The correlation functions that will be used in the implementation are the same as those used for the local method, namely SSD, NSSD and ZNSSD. Here, again to simplify, the SSD (Sum of Squared Differences) is used to present the method:

$$r_{SSD} = \iint_{\Omega_e} ([f(\mathbf{x}-\mathbf{d}) - g(\mathbf{x})]^2) d\mathbf{x} \tag{2.7}$$

When substituting the first order Taylor expansion of $f(\mathbf{x}-\mathbf{d})$ into Eq. 2.7 the cost function becomes:

$$r_{SSD} = \iint_{\Omega_e} ([-\mathbf{d}\cdot\nabla f(\mathbf{x}) + f(\mathbf{x}) - g(\mathbf{x})]^2) d\mathbf{x} \tag{2.8}$$

A pre-described function for $\mathbf{d}$ [3], the displacement within element Ω_e object of the mesh Δ, on an arbitrary basis Φ_i is introduced as

$$\mathbf{d} = \sum_{i,a} \Phi_i \, \delta_{ia} \, \mathbf{e}_a, \tag{2.9}$$

where $i \in [1, n]$ is the number of the shape function, e_a are the system directions x and y and δ_{ia} are the displacement parameters. In traditional global DIC, first order shape functions are used in this description. Each element is mapped to a natural system, a square with side 1 in the local system (ξ, η), as shown in Fig 2.4.

The basis Φ_i is then defined as:

$$\Phi_1 = (1-\xi)(1-\eta) \tag{2.10a}$$

$$\Phi_2 = \xi(1-\eta) \tag{2.10b}$$

$$\Phi_3 = (1-\xi)\eta \tag{2.10c}$$

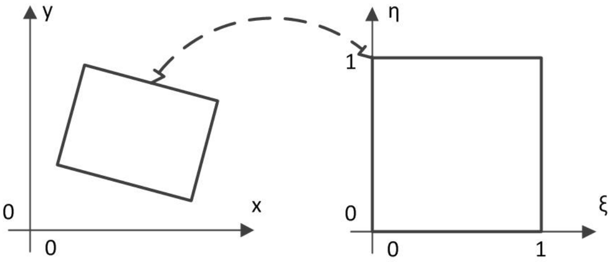

Figure 2.4: Mapping of a Q4 element on a square $[0, 1]^2$.

$$\Phi_4 = \xi\eta \tag{2.10d}$$

Minimising Eq. 2.8 with respect to δ_{ia}, yields a linear equation:

$$[K_{ijab}]^e [\delta_{ia}]^e = [F_{jb}]^e \tag{2.11}$$

with:

$$[K_{ijab}]^e = \iint_{\Omega_e} \Phi_i \; [\nabla_a f] \, \Phi_j \; [\nabla_b f] \; d\mathbf{x} \tag{2.12}$$

$$[F_{jb}]^e = \iint_{\Omega_e} [g(\mathbf{x}) - f(\mathbf{x})] \, \Phi_j \, [\nabla_b f] \; d\mathbf{x} \tag{2.13}$$

Here, e is the element number and ∇_a is the derivative of the function to a. Note that $a, b \in \{x, y\}$. Iterative calculation is critical as a Taylor expansion is used, and thus the calculated displacements are an approximation of the real displacements. In [22] this was carried out by re-correlating a deformed image that is shifted with the integer value of the previously calculated displacement.

In this work, no image shifting is used as it introduces extra uncertainties. Instead an extra displacement **d'** is introduced, to our knowledge not used in current implementations, representing the previous displacement field. The equation used in this proposed algorithm (in contrast to Eq. 2.6):

$$f(\mathbf{x} - \mathbf{d}) = g(\mathbf{x} + \mathbf{d}'). \tag{2.14}$$

Resulting in element equations:

$$[K_{ijab}]^e = \iint_{\Omega_e} \Phi_i \; (\nabla_a f) \, \Phi_j \; (\nabla_b f) \; d\mathbf{x} \tag{2.15}$$

$$[F_{jb}]^e = \iint_{\Omega_e} (g(\mathbf{x} + \mathbf{d}') - f(\mathbf{x})) \, \Phi_j \, (\nabla_b f) \; d\mathbf{x} \tag{2.16}$$

Summarised, the extra displacement relative to the previous calculated displacement $\mathbf{d}'$ can be determined by solving the equation 2.11 containing a matrix [K] and a matrix [F] which are both based on the gray values of the reference and deformed image. Obtaining $\mathbf{d}$ using δ_{ia} and adding $\mathbf{d}'$ results in the complete displacement field. The identified displacement field can then be used as $\mathbf{d}'$ in the next iteration. One iteration is thus described as solving

$$f(\mathbf{x} - \mathbf{d_i}) = g(\mathbf{x} + \mathbf{d'_i}) \tag{2.17}$$

to d_i where $d'_i = d'_{i-1} + d_{i-1}$. In this scheme $d_i \longrightarrow 0$ while $d'_i \longrightarrow d$. It is worth noting that at this stage no interconnectivity between elements is included and that although the equation contains a K and F matrix, similar to stiffness and force matrix in finite element analysis (FEA), no constitutive material laws are used. The solution of the element equation (Eq. 2.11) to δ_{ia}, results in $\mathbf{d}$ (described by Eq. 2.9) representing a displacement field within Ω_e.

Solving the system for all the elements of mesh Δ results in a displacement field for each element in the mesh separately without any interconnectivity, and therefore no C^0-continuity is taken into account. To include this connectivity, all element equations are assembled to one linear "system equation":

$$[K]^s[\delta] = [F]^s \tag{2.18}$$

It is common practice to combine the element matrices into the system matrix as it is analogous to FEA [3]. Solving this system will result in a matrix δ containing all separate δ^e_{ia}, but now with the connectivity taken into account.

To increase the convergence range of the FE-DIC approach, Besnard et al. developed the so called multi-scale scheme [22]. In this approach the correlation starts on down sampled images. By doing so, the displacement is reduced to several pixels so that iterations can start from zero values for the unknown DOF ($\mathbf{d}'$=0). Once the down-sampled images are correlated, the images and their displacements are up-scaled. The up-scaled images are re-correlated using the deformation of the down-scaled images as $\mathbf{d}'$.

A possible advantage of the FE-DIC could be the link towards FE-simulations. The use of nodal points and shape functions in both DIC and FEA definitely creates a clear link. In practice though, elements in FE-simulations should be chosen wisely to represent a converged solution of the simulated problem [23]. In FEA smaller elements will almost always lead to better results. The use of small elements however is not desirable in global DIC as it is known that the displacement resolution is inversely related to the element size [24]. Therefore small elements will lead to poor measurements, and at a certain size suffer from correlation issues as the amount of speckles included in the element decreases.

While most of the studies using FE-DIC implemented Q4 or Q8 elements (Q4-DIC or Q8-DIC), many variations on this method have been developed. Recently, the FE-DIC approach has been extended to higher-order FE shape functions. For example, Hild et al. used beam elements to directly measure DOF obeying the kinematics defined by the Euler-Bernoulli beam hypothesis [25]. This type of variation is now called integrated DIC (i-DIC) [26] where, by using very specific shape functions, the DOF used in the global approach are directly linked to mechanical properties. The downside of these methods is that they include pre-knowledge of the solution and only work for specific cases. Besides the use of special shape functions, Langerholc et al. [27] introduced a higher order FE-DIC approach by introducing isoparametric elements with 24 DOF to ensure the strain continuity across the elements. Another variation is Extended FE-DIC, an approach specially developed to identify displacement heterogeneities or other forms of displacement discontinuities in the neighbourhood of a crack or shear bands [28]. In Extended DIC, no mesh refinement is performed but additional DOF for nodes of elements, split by the crack line, are introduced. The additional DOF allows discontinuities without the need for mesh refinements.

Aside from this popular FE-DIC some other approaches exist. For example B-Spline functions were used by Cheng et al. [21] to make displacement fields with continuous derivatives. These functions are piece-wise polynomials that possess a certain continuity making them extremely usable for measuring smooth deformation fields. However, the main problem is the significantly more complex code and the loss of the clear link towards finite element simulations.

Strain Calculation

In contrast to the local method, a continuous displacement field is obtained. Therefore strains are derived directly from the displacement field without performing local smoothing. It should be noted that the displacement field is only C^0-continuous and thus a non continuous deformation field is obtained. The non-continuities in the strain field are found at the elements boundaries, while the strains within the elements are continuous. Using Eq. 2.9 as displacement function, the derivative to α can be calculated as:

$$\frac{\delta d}{\delta \alpha} = \sum_i \frac{\delta \Phi_i}{\delta \alpha} \delta_i \tag{2.19}$$

Remark that if a Q4 element is used, strains within an element are constant (see Chapter 5).

2.1.3 Error Sources

Although DIC is a very robust technique, the accuracy of the measurement is very dependent on the quality of the test and data processing. Below an overview is given of the most important error contributions in DIC.

Interpolation

To obtain a sub-pixel displacement accuracy in DIC, the gray levels and their gradients have to be interpolated from the regular grid structure. The error introduced by the interpolation scheme is most often obtained by performing a rigid body motion test. The positional error caused by the interpolation is dependent on the sub-pixel value of the actual displacement. The systematic error is typically a sinusoidal function between displacement 0 and 1 pixel. The error for three different interpolation schemes is found in Fig 2.5.

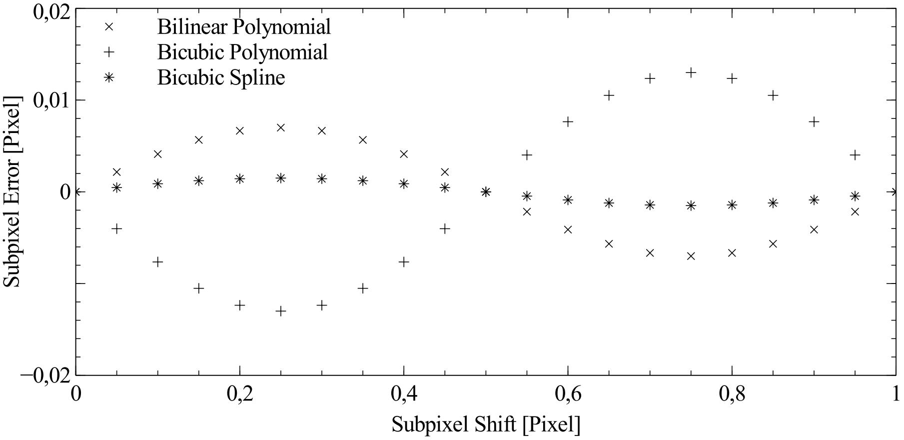

Figure 2.5: Systematic error in the displacement field using different interpolation schemes.

The comparison of different interpolations used in DIC has been made in [29][18]. A higher order interpolation scheme is highly recommended.

Subset/element size, Shape function and Strain window

One problem related to the local approach is the selection of the optimal subset size. It should be large enough to contain sufficient features while - at the same time - small enough to represent the underlying deformation [30][18]. Increasing the order of the shape functions of the subset in order to enhance the capability of representing the deformation is possible, but it will also increase the sensitivity to noise [31]. It has been shown though, that using a quadratic subset reduces the systematic error with approximately the same random error [17]. In literature, quite some research has focussed on the optimal subset size and shape function. Using these studies, a particular subset size for a certain speckle pattern and application can be advised [32][33]. The second problem is the choice of strain window size. The strain window is used to smooth the displacement field prior to differentiation, in order to reduce the influence of the displacement noise. The same reasoning as for the subset size and shape function can be made for the strain window and polynomial order. A large strain window and low polynomial order reduces noise sensitivity but also reduces spatial resolution (see section 2.1.4). The other way around, a small higher-order window is capable of representing complex deformations but has very high noise sensitivity. In global DIC, the same trade-off is present, but only at displacement level. Because strains are derived directly from the displacement field, no choice of strain windows has to be made. For the displacement, the same question of ideal element size versus element order exists hence the importance of this work.

It is the aim of this work to limit the influence of these user dependent parameters, in an attempt to achieve a complete automatic measurement procedure that provides results that are to a large extend user independent.

Camera noise

In DIC, digital images are used for tracking the deformation. During the recording of these images, noise is inevitably present. This noise, introducing gray level fluctuations not related to any deformation, will result in artificial displacements when the difference between reference and deformed image is minimised. A theoretical model has been developed to evaluate the influence of noise on the final deformation field [24][34][35]. The study indicates that an increase of noise in the images results in a proportional increase of random error in the measured displacement field. The effects of noise can be reduced considerably using one of the following methods:

- High performance hardware: The use of high performance hardware such as cooled CCD cameras can reduce the noise considerably.
- Filtering: The use of a filter or smoother can reduce the noise contained in the image. Reducing noise in this way has to be done with care as the

signal is altered and thus possible actual deformation can be modified.

- Averaging: As noise is shown to be random, averaging multiple images taken at the same deformation state can reduce the noise.

Light conditions

Perfect homogeneous light conditions are hard to obtain. In most applications, a change in lighting is present across the image. Also during the capturing of the digital images, a change in illumination can occur. This change of light influences the correlation procedure. However, the influence of the change in lighting can be resolved by using appropriate correlation criteria [14][15]. In Table 2.1, the main correlation criteria are introduced.

Criteria	**Value**	**Light change**
SSD	$\sum \left[f(\mathbf{x}-\mathbf{d}) - g(\mathbf{x}+\mathbf{d}')\right]^2$	None
ZSSD	$\sum \big[(f(\mathbf{x}-\mathbf{d}) - \bar{f}) - (g(\mathbf{x}+\mathbf{d}') - \bar{g})\big[^2$	Offset
NSSD	$\sum \left[\frac{f(\mathbf{x}-\mathbf{d})}{\sqrt{\sum f(\mathbf{x}-\mathbf{d})^2}} - \frac{g(\mathbf{x}+\mathbf{d}')}{\sqrt{\sum g(\mathbf{x}+\mathbf{d}')^2}}\right]^2$	Scale
ZNSSD	$\sum \left[\frac{(f(\mathbf{x}-\mathbf{d})-\bar{f})}{\sqrt{\sum (f(\mathbf{x}-\mathbf{d})-\bar{f})^2}} - \frac{(g(\mathbf{x}+\mathbf{d}')-\bar{g}))}{\sqrt{\sum (g(\mathbf{x}+\mathbf{d}')-\bar{g})^2}}\right]^2$	Scale + offset

Table 2.1: Correlation criteria and their robustness to light.

Note that using more complex correlation functions to handle light conditions will increase the measurements resolution (see section 2.1.4) as more DOF are introduced in the correlation procedure [30].

Out of plane motion

Having the camera perpendicular to the specimen is an absolute requirement for a successful 2D DIC measurement. Because a 2D setup does not provide any depth information, movements towards the camera (out of plane motions) are disadvantageous for the surface measurement. The effects of out of plane motions and possible methods for compensating them are discussed in Chapter 6.

Lens distortions

One of the key features in the experimental setup for DIC is the lens. As is well known, lenses introduce distortions into the images. The errors from this source are gradually being acknowledged and methods to compensate them have been described. For example, using the camera parameters obtained from a single camera system, the displacements can be corrected for radial and tangential (or decentering) distortions [6]. An alternative method for determining lens distortion coefficients is based on measuring additional in-plane displacements, introduced by the lens distortions, when rigid body motions are conducted [36]. In [37], a single cross-grating is used as a calibration reference. Using a two-dimensional Fourier transformation, the phases of the grating pattern are analysed and lens distortion distribution is obtained from the unwrapped phase maps. The lens distortions are more important when special hardware is used such as light microscopes [4][38] or electrone microscopes [39][40][41]. In the present dissertation, a procedure is used to compensate out of plane motions (See Chapter 6). Here, an extra region of interest is attached to the specimen[42], denoted as Region of Compensation (ROC). This method is developed to compensate out of plane motions, but has the extra advantage to directly compensate the lens distortions. Note that here the distortion coefficients are not explicitly determined, but the distortions are compensated during the test using the ROC. The extra region is assumed to follow the rigid body motions of the specimen but not the deformations. In this way, similar to the methods presented above, all artificial deformations can be corrected.

Speckle pattern

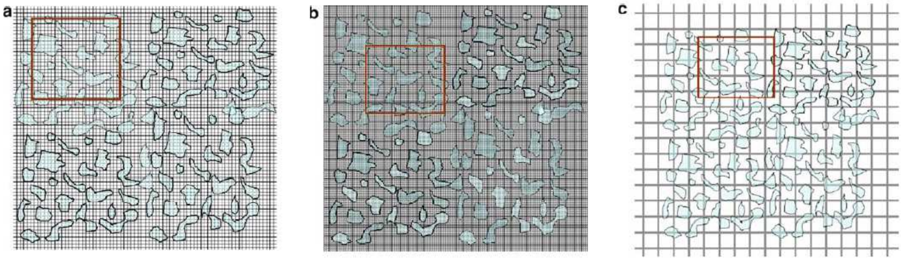

Figure 2.6: Three examples representing (a) near-optimal sampling, (b) slight over-sampling and (c) under-sampling, of a fixed portion of the object speckle pattern defined by the specified subset region [1].

As DIC tracks features, denoted as speckles, from the reference to the deformed image, the quality of the measurement will be closely related to the quality of the speckle pattern. A pattern can vary in characteristics such as contrast, gradients or speckle size. Many different parameters were proposed to assess the quality of the speckle pattern. Amongst those speckle size [43], subset entropy [33] and sum of square of subset intensity gradients [32]. A key property of a speckle is its size. It should be large enough to be represented by the pixels, while at the same time it should remain small to increase the accuracy of the measurement. A rule of thumb is a speckle should be 3 by 3 pixels. In Fig. 2.6 three different sizes are presented. In Fig. 2.6a the speckle is 5 pixels, which is near optimal. In Fig. 2.6b the speckles are 10 pixels large, which is slight over sampling. 2.6. Fig. 2.6c represents under sampling as a speckle is smaller than a pixel.

2.1.4 Resolutions

To describe the performance of a full-field measurement, the resolution and spatial resolution can be used. As the terms will be used quite frequently in the present dissertation, the quantities are defined as [44]:

- **Resolution**: The resolution of the measured displacement is the smallest change in the displacement (strain) to be measured that produces a perceptible change in the measured displacement (strain). In this sense, the resolution is quantified by the level of noise in the measured displacement (strain) field. The noisy field originates from numerous sources of error including (but not limited to) the image noise, gray level quantisation and image distortions coming from the optical technique. In physical units (other than pixels), it is also a function of the sampling resolution (magnification) of the imaging system.
- **Spatial resolution**: The spatial resolution is defined as the smallest distance between two points for which two independent measurements can be obtained. Similarly, the spatial resolution is the area needed to identify a measurement point. The spatial resolution of a full-field measurement algorithm (more generally measurement system) determines how many independent measurement points the full-field technique can provide. Note that this resolution is defined in the spatial domain and is therefore inversely related to the well-known frequency-domain resolution. Consequently, as opposed to the intuitive understanding, a smaller spatial resolution is more favourable.

It is well known that there is a compromise between the displacement (strain) resolution and the spatial resolution (See Section 3.5.1). It should be equally noted that when the displacement is smoothed to determine strains, the spatial resolution for the strains increases (less desirable) (see 2.1.1 - Strain calculation).

2.1.5 Applications

In traditional strain measurements usually strain gauges or extensometers are used. The advantage of DIC over these methods is the full field information compared to the local strain of the strain gauge or the averaged global strain of the extensometer. Within the full field measurements, the advantage of DIC is usually the easy to use and robust setup. Furthermore, the method does not require any special equipment and has a wide range of applicability. In essence, the following applications occur:

- Strain mapping: The main application of DIC is quantitatively determining the deformation field of various materials [14]. E.g. composites [45][46], rubbers [47], biological materials [48], ... Machine monitoring or structural testing can be placed in this category.
- Surface shape reconstruction: With the stereo version of DIC, the shape of a specimen can be reconstructed. Hereby, the shape of products can be validated using DIC [49].

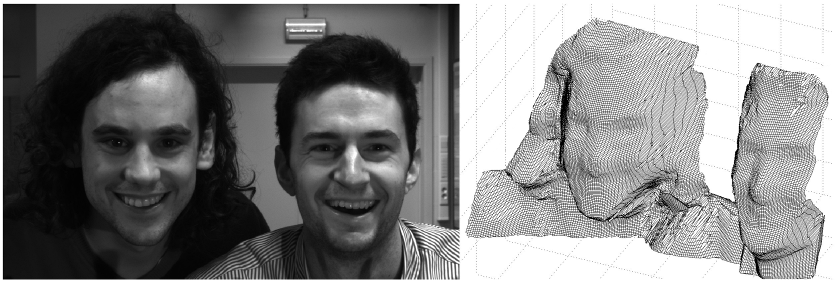

Figure 2.7: Shape reconstruction by stereo setup.

- Validation: The deformation field obtained with DIC can be used for the validation of models or theories. The results obtained from an experimental test can be compared to the finite element models when for example complex materials are implemented [50].
- Material identification: The deformation fields can also be used to perform material identification of the tested specimen [51][52][53][54]. One method

in determining material behaviour is Finite Element Model Updating (FEMU) [55], where a finite element model is created with unknown material parameters. By coupling the measured and simulated deformation field, a change to the current simulated parameters can be made. When performing this procedure iteratively, the final material properties of the specimen can be derived. Another approach is directly using the deformation field for obtaining the material parameters. The most known example of this approach is the Virtual Fields Method (VFM) [56].

2.2 Adaptive Finite Element Method

In the finite element method, a continuous domain is subdivided into a finite number of discrete subregions defined by the finite element mesh. For finite element simulations in solid mechanics, this domain represents a continuous displacement field. This displacement field is expressed by shape (approximation) functions at certain points in the element space. If the shape functions are denoted as Φ, then the displacement in an element can be denoted as:

$$\mathbf{d} = \sum_{i}^{N} \Phi_i \, \delta_i = [\Phi_i]\{\delta_i\} \tag{2.20}$$

where i denotes the function number and N the amount of functions used in the approximation. $\{\delta_i\}$ is a vector containing the unknown displacements. An element is characterised by its size h and polynomial order p. In the simplest approximation, $p = 1$, $\{\delta_i\}$ represents the unknown corner displacements. Introducing an approximated description, inevitably results in discretisation errors in the finite element solution [57].

This error can be reduced by introducing adaptivity in the finite element mesh. Adaptivity in FEA means gradually introducing more DOF and thus refining the mesh. Several approaches can be used to achieve mesh refinement. The most common ones are h-, r- and p-refinement [23]. Using the h-method, mesh refinement is obtained by reducing the element size in order to cope with more complex deformations while the element order remains constant. This approach is the most attractive to FEA as the mathematics remain unchanged. Only the re-meshing of the ROI is needed to obtain a more accurate solution. The principle of h-refinement is shown in Fig 2.8.

Another approach is r-refinement, where the nodes are moved to obtain a more appropriate mesh. This method is less used because the amount of DOF is

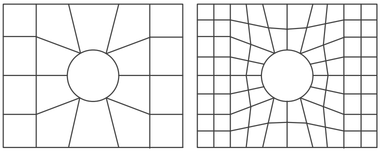

Figure 2.8: h-refinement of a finite element mesh where nodes are added to mesh to represent more complex deformations.

fixed and therefore adaptivity is limited by the initial mesh. The principle of r-refinement is shown in Fig 2.9.

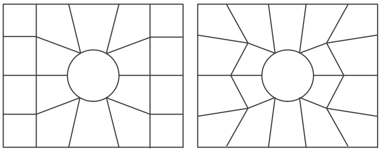

Figure 2.9: r-refinement of a finite element mesh where nodes are moved to represent more complex deformations.

In the p-refinement approach, refinement is obtained by upgrading the elements to a higher polynomial order and thus adding extra DOF to the elements. Increasing the element order improves the approximation of the initial displacement field, again reducing the discretisation error. The principle of p-refinement is shown in Fig 2.10.

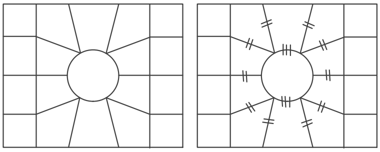

Figure 2.10: p-refinement of a finite element mesh where higher order shape functions are used. The number of lines through the edge indicate the edge order.

Increasing the element order can be done in two ways. The conventional approach for obtaining a higher order element is adding more nodes and deriving a new set of shape functions for this element. Here, the best known set of shape functions is derived from the Lagrange polynomial [3]. The element in its first, second and third order configuration is shown in Fig 2.11

The displacement description then becomes

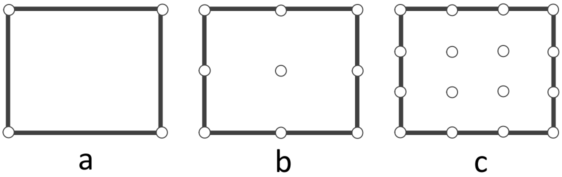

Figure 2.11: Element refinement, Lagrange element. Each dot represents a node within the element.

$$\mathbf{d} = \sum_{i}^{N'} \Phi'_i \, \delta'_i = [\Phi'_i]\{\delta'_i\} \tag{2.21}$$

where $\{\delta'_i\}$ now represents the unknown displacements of all element nodes. The second approach to obtain higher order elements is expanding the set of shape functions without altering the previous shape functions or without adding extra nodes. This can be achieved using hierarchical functions. The best known and used set of hierarchical functions are generated from the Legendre polynomial. Φ can be found by a linear combination of $P_a(\chi)$ (See Appendix A)

$$P_0(\chi) = \frac{1}{2}(1-\chi) \tag{2.22}$$

$$P_1(\chi) = \frac{1}{2}(1+\chi) \tag{2.23}$$

The higher order functions for $p \geq 2$:

$$P_p(\chi) = \frac{1}{(p-2)!2^{p-2}} \frac{d^{p-2}}{d\chi^{p-2}}[(1-\chi^2)^{p-1}] \tag{2.24}$$

The advantage of this approach is that shape functions are only added and not altered, resulting in a very efficient refinement scheme. The process is illustrated in Fig 2.12.

Literature indicates that using a p-refinement scheme the finite element mesh converges faster than using a h-refinement scheme [3]. The use of p-refinement does have some disadvantages. First of all, the non-uniform p-refinement procedure creates a very complex database of shape functions and element parameters. The database is complex because the extra DOF, introduced by the refinement, are added through the mesh without any logical numbering

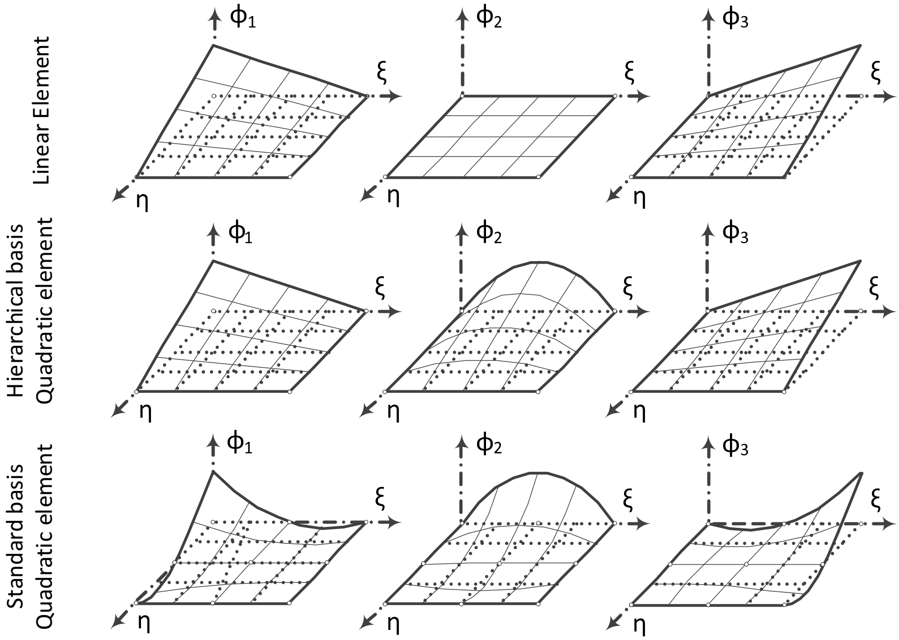

Figure 2.12: Three shape functions for a linear and quadratic element using a standard en hierarchical bases.

plan. Randomly introducing DOF also results in stiffness matrices which have no fixed description any more. They vary as the DOF are introduced into the mesh. Another disadvantage of p-elements is that the displacement vector δ_i does not represent simple nodal displacements. The values within the vector now indicate the amplitude of the associated shape function (See Chapter 3). For obtaining the final displacement field, one should always use the relation 2.20.

2.3 Kinematics of deformation

Coordinates

As DIC is an optical measurement method for determining surface deformation, an introduction to 'Kinematics of deformation' is presented. A continuous body can be considered in two conditions as shown in Fig 2.13. The first condition is the undeformed state B_0, the second refers to the actual or deformed state B.

Within the body, a material point is described by its material coordinates ζ. The position vector x of a material point P within the body can be written as a function χ of its material coordinate ζ and time t:

$$x = \chi(\zeta, t) \tag{2.25}$$

Using Eq. 2.25, material points in their initial state can be identified as:

$$x_0 = \chi(\zeta, t_0) \tag{2.26}$$

In continuum mechanics, points are often marked by their position in the initial state rather than by their material coordinate. Function χ then becomes:

$$x = \chi(x_0, t) \tag{2.27}$$

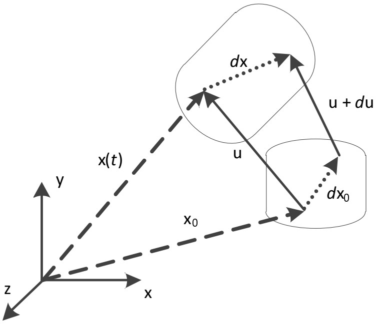

Figure 2.13: A continuous body in its undeformed and deformed state.

Deformation tensor

From the position vector, a displacement vector u can be defined as shown in Fig 2.13.

$$u = \chi(x_0, t) - x_0 \tag{2.28}$$

The deformation of the body can be obtained by moving the point on the body over an infinitesimal distance dx_0. The actual position of the moved point is then $x + dx$, where dx and dx_0 are related by the deformation gradient F:

$$dx = F.dx_0 \tag{2.29}$$

where

$$F = \frac{dx}{dx_0} = \begin{bmatrix} \frac{\delta x}{\delta x_0} & \frac{\delta x}{\delta y_0} & \frac{\delta x}{\delta z_0} \\ \frac{\delta y}{\delta x_0} & \frac{\delta y}{\delta y_0} & \frac{\delta y}{\delta z_0} \\ \frac{\delta z}{\delta x_0} & \frac{\delta z}{\delta y_0} & \frac{\delta z}{\delta z_0} \end{bmatrix} \tag{2.30}$$

From the deformation gradient F, displacement gradient G can be defined as:

$$G = F - I = \begin{bmatrix} \frac{\delta x}{\delta x_0} - 1 & \frac{\delta x}{\delta y_0} & \frac{\delta x}{\delta z_0} \\ \frac{\delta y}{\delta x_0} & \frac{\delta y}{\delta y_0} - 1 & \frac{\delta y}{\delta z_0} \\ \frac{\delta z}{\delta x_0} & \frac{\delta z}{\delta y_0} & \frac{\delta z}{\delta z_0} - 1 \end{bmatrix} = \begin{bmatrix} \frac{\delta u_x}{\delta x_0} & \frac{\delta u_x}{\delta y_0} & \frac{\delta u_x}{\delta z_0} \\ \frac{\delta u_y}{\delta x_0} & \frac{\delta u_y}{\delta y_0} & \frac{\delta u_y}{\delta z_0} \\ \frac{\delta u_z}{\delta x_0} & \frac{\delta u_z}{\delta y_0} & \frac{\delta u_z}{\delta z_0} \end{bmatrix} \tag{2.31}$$

Strain tensors

Using the deformation or displacement gradient, strain tensors can be derived. The definition of strain tensor is not unique. Several frequently used are:

- Green Lagrange tensor:

$$\epsilon^{GL} = \frac{1}{2}(F^T F - I) = \frac{1}{2}(G + G^T) + \frac{1}{2}G^T G \tag{2.32}$$

- Logarithmic Euler-Almansi:

$$\epsilon^{lnEA} = ln(\sqrt{FF^T}) \tag{2.33}$$

In this work, unless specified differently, the logarithmic Euler-Almansi tensor is used as strain tensor.

Chapter 3

A self adaptive digital image correlation algorithm

In Chapter 3, the main principles for adaptive digital image correlation are presented. Both the mathematical framework and the implementation are discussed. Further the new approach is validated in numerical experiments.

Wittevrongel L., Lava P., Lomov S.V. and Debruyne D. A Self Adaptive Digital Image Correlation Algorithm. *Experimental Mechanics,* 55(2): 361-378, 2015
Some parts of the original publication are left out or modified to avoid redundancy.

3.1 Abstract

In the present paper, a novel Digital Image Correlation algorithm is presented, focussing on accurately determining small strains with high strain gradients. Principles from p-adaptive finite element analysis are implemented to obtain a self adapting higher order mesh. The self adapting principle reduces the dependency of the results on the user's input and the higher orders ensure sufficient degrees of freedom. Performance of the algorithm, in terms of resolution and spatial resolution, is checked and compared to the traditional local method. The results indicate that the introduced method is appropriate for accurately measuring highly heterogeneous deformations and that the obtained data is to a large extent user independent.

3.2 Introduction

The global description was mainly developed by Besnard et al. [22]. A comparison with the local DIC method [58] proved this concept of global DIC. Several algorithms based on the global DIC method have been developed over the last years ([21][22][26][25][59]), all leaving the polynomial degree of the mesh fixed ranging from linear (Q4) elements to higher order elements. The matching algorithm uses a fixed mesh, with the pre-described degree of freedom (DOF) determined by the element order, to determine the displacement field as described before. The element size and pre-described DOF are critical for a good solution as they influence the displacement/strain and spatial resolution the same way a subset does [59]. When extra spatial resolution is needed, refinement of the mesh is done by the user based on his experience. In this context, refinement refers to reducing the element size. This type of refinement is called h-refinement, where h denotes the element size. In our proposed method principles from the adaptive finite element are adopted in the algorithm to overcome this problem of user based refinement.

The new approach is developed to fulfil the desire of minimising the error due to discretisation [60], caused by meshing and refinement based on the user's instinct. In the local method, this discretisation is caused by the choice of subset, step and strain window. By using an adaptive mesh, locations where the displacement is rather heterogeneous are automatically refined by an algorithm similar to FEA [61]. To our knowledge this is the first development of a fully self-adaptive global image correlation algorithm. The new method uses principles like p-adaptive mesh, error estimation and hierarchical shape functions [3]. The use of these principles leads to a very important advantage: extra degrees of freedom can be introduced gradually if the mesh is unable to describe the imposed displacement. This increase of freedom is done automatically, triggered by an error estimator, so the data becomes less user dependent.

This paper is outlined as follows. In section 3.3, the main principles of the local and global method are presented. Section 3.4 describes the new method based on the global approach and in section 3.5 a comparison between local, global and our proposed algorithm is performed. Finally, in section 3.7, the local and the adaptive global algorithm are used to correlate a standard tensile test.

3.3 Digital Image Correlation

Omitted to avoid redundancy, see Chapter 2.

3.4 p-DIC

3.4.1 General description

In the derivation of the global approach, the following description for the displacement was used:

$$\mathbf{d} = \sum_{i,a} \Phi_i \delta_{ia} \mathbf{e}_a \tag{3.1}$$

where Φ_i denote the shape functions of the used basis [3]. Such a basis is usually expressed in local coordinates to obtain a more general and generic description. An element described in these local coordinates is a square element where local coordinates [ξ, η] are within the range of [-1 .. 1] (so-called master-element, see Fig 3.1).

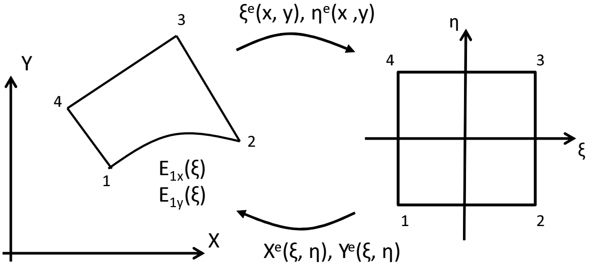

Figure 3.1: Mapping coordinates from global to local coordinate system.

The transformation of the local coordinates $\xi = [\xi, \eta]^T$ into the global coordinate $\mathbf{x} = [x, y]^T$ can be calculated using mapping functions X^e and Y^e :

$$\mathbf{x} = [x, y]^T = [X^e(\xi, \eta), Y^e(\xi, \eta)]^T \tag{3.2}$$

When a p-adaptive mesh (where elements can transform to higher orders) is used, elements are usually larger than the ones used in h-refinement. Using these larger elements makes the traditional linear mapping not accurate enough and more precise mapping is necessary. Therefore, in contrast to previous global algorithms, not only the four corner nodes of the element are used for the mapping, but extra functions are blended with the linear functions to obtain a more precise mapping [62]. These functions, denoted by E_j, describe the shape of edge j and are defined as parametric functions $E_j = [E_{jx}(\chi), E_{jy}(\chi)]^T$, where

χ is the local coordinate. The linear node functions $N_i(\xi,\eta)$ can be defined as:

$$N_i(\eta,\xi) = \frac{1}{4}(1+\xi_i\xi)(1+\eta_i\eta) \tag{3.3}$$

where (ξ_i,η_i) denotes the local coordinates of the i^{th} node. Using E_j and $N_i(\xi,\eta)$, the mapping functions are defined as:

$$\begin{aligned} X^e(\xi,\eta) = \frac{1}{2}(1-\eta)E_{1x}(\xi) + \frac{1}{2}(1+\xi)E_{2x}(\eta) \\ + \frac{1}{2}(1+\eta)E_{3x}(\xi) + \frac{1}{2}(1-\xi)E_{4x}(\eta) \\ - \sum_{i=1}^{4} N_i(\xi,\eta)x_i \end{aligned} \tag{3.4}$$

$$\begin{aligned} Y^e(\xi,\eta) = \frac{1}{2}(1-\eta)E_{1y}(\xi) + \frac{1}{2}(1+\xi)E_{2y}(\eta) \\ + \frac{1}{2}(1+\eta)E_{3y}(\xi) + \frac{1}{2}(1-\xi)E_{4y}(\eta) \\ - \sum_{i=1}^{4} N_i(\xi,\eta)y_i \end{aligned} \tag{3.5}$$

where x_i and y_i denote the global coordinate of node i. It is important to notice that no iso-parametric description, where shape and mapping functions are the same, is used but that shape and mapping functions are independent of each other. The choice of shape functions (defining the displacement) is critical as they must be capable of coping with the updating procedure of an adaptive finite element mesh. The shape functions used are hierarchical functions, the same functions as used in p-adaptive finite elements. More specific, the shape functions used are based on Legendre polynomials and are shown in Appendix A.

The most important property of these hierarchical bases is that, in contrast to the shape functions used in traditional FEA, higher order shape functions will not influence the shape functions of lower orders. This property of independent hierarchical shape functions lead to the interesting characteristic that refining an element, introducing higher orders, does not influence the already calculated parameters for [K] and [F]. This property is illustrated in Section 3.4.3.
As mentioned above the shape functions are expressed in local coordinates. It

is generally believed that the reversed mapping functions can not be explicitly determined [63]. Therefore the hierarchical shape functions Φ_i cannot be found in the global [x, y] system analytically and thus the coefficients from equation 2.11 can not be calculated directly. Consequently a transformation of the element equations from [x, y] to [ξ, η] is necessary. The element matrices become:

$$\begin{aligned}[K_{iajb}]^e = \iint \Phi_i(\xi,\,\eta)\,\nabla_a f(\mathbf{x}(\xi,\,\eta))\,\Phi_j(\xi,\,\eta)& \\ \nabla_b f(\mathbf{x}(\xi,\,\eta))\,\det([\mathrm{J}])\,\mathrm{d}\xi\;\mathrm{d}\eta&\end{aligned} \tag{3.6}$$

$$\begin{aligned}[F_{jb}]^e = \iint (g(\mathbf{x}(\xi,\,\eta) + d') - f(\mathbf{x}(\xi,\,\eta)))& \\ \Phi_j(\xi,\,\eta)\,\nabla_b f(\mathrm{x}(\xi,\,\eta))\,\det([\mathrm{J}])\,\mathrm{d}\xi\;\mathrm{d}\eta&\end{aligned} \tag{3.7}$$

Where J is the Jacobian of the system, and ξ, $\eta \in$ [-1 .. 1]. Note that $a, b \in \{x, y\}$, and thus still remains in global coordinates.

By transforming the coefficients from a global to a local framework, the element equations are built with local (equals transformed global) shape functions.

$$\Phi_i^l = \Phi_i^g[X^l(\xi,\eta), Y^l(\xi,\eta)] \tag{3.8}$$

where X^l and Y^l are the mapping functions in element l and Φ_i^l and Φ_i^g are the local and global shape functions. This is based on having the global description for the shape function. In practice, shape functions are given in the local system following the principle shown in Appendix A. In the algorithm the same scheme of assigning shape functions is used. Downside is that choosing local functions instead of transformed global functions obstructs the assembly process of the system equations. This obstruction is explained in following reasoning. When a certain object, node or edge, belongs to more than one element (e.g. common edge between two elements) it has as much local shape functions as it has connected elements. The use of transformed global shape functions as local functions insures that all local functions for the same object transform back to the same global shape function, which is necessary for the assembling process.

$$\begin{aligned}\Phi_i^1[\xi^1(x,y), \eta^1(x,y)] &= \Phi_i^2[\xi^2(x,y), \eta^2(x,y)] \\ &= \Phi_i^g[x,y]\end{aligned} \tag{3.9}$$

where

$$\Phi_i^1 = \Phi_i^g[X^1(\xi,\eta), Y^1(\xi,\eta)] \; \mathit{and} \; \Phi_i^2 = \Phi_i^g[X^2(\xi,\eta), Y^2(\xi,\eta)] \tag{3.10}$$

Assuming that ξ^1, η^1, X^1, Y^1 and ξ^2, η^2, X^2, Y^2 are the mapping functions of respectively common element 1 and 2 and Φ_i^g is the global shape function. In words, we can describe the condition as: "The equations can be assembled to the system equations if each object copes with the fact that all local shape functions have the same transformed global shape function". When locally assigned shape functions are used, this condition is not always met. The problem is illustrated in Fig. 3.2 for a 3^{th} order edge. The figure clearly indicates that both local functions do not describe the same global function, resulting in inverted parameters for the local element functions. Here δ_1 will denote a positive horizontal displacement, as δ_2 denotes a negative displacement. On the edge, the shape functions become (see Appendix A):

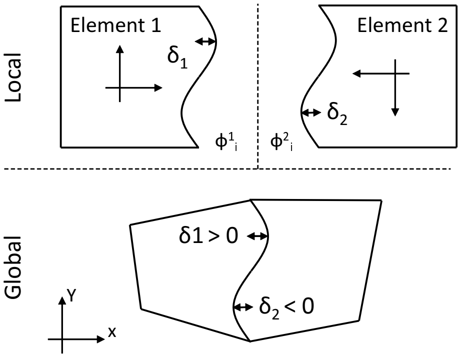

Figure 3.2: Visualisation of obstruction in assembly process by the use of locally assigned shape functions.

$$\Phi_i^1 = 2\eta^1((\eta^1)^2 - 1) \tag{3.11}$$

$$\Phi_i^2 = 2\eta^2((\eta^2)^2 - 1) \tag{3.12}$$

The displacement field is then:

$$u = \delta^1 2\eta^1((\eta^1)^2 - 1) = \delta^2 2\eta^2((\eta^2)^2 - 1) \tag{3.13}$$

and because $\eta^1 = -\eta^2$ (seen in geometry), previous equation yields:

$$\delta^1 = -\delta^2 \tag{3.14}$$

Here, the condition for system assembly is not met, whereas δ^1 is inverse of δ^2 and thus both functions describe inverse displacement fields. To satisfy the condition, an inversion of one of the element shape functions has to be done. Instead of inverting the shape function directly, a transformation on the final element equations is performed. For the calculation of the element equations the original, local shape functions are used and when the system is assembled, the element matrices get transformed so the assembly becomes possible. This transformation is done by a general procedure based on the so-called 'direction' of the edges as it can be shown that the problem only arises on shape functions of edges with an odd polynomial order and specific direction.

3.4.2 Strain calculation

As the displacement field is analytical, strains can be derived directly from the displacements. The Green-Lagrange strain tensor is defined as:

$$E = \frac{1}{2}(F^T F - I) = \frac{1}{2}(G + G^T) + \frac{1}{2}G^T G \tag{3.15}$$

where

$$G = \begin{bmatrix} \frac{\delta d_x}{\delta x} & \frac{\delta d_x}{\delta y} \\ \frac{\delta d_y}{\delta x} & \frac{\delta d_y}{\delta y} \end{bmatrix} \tag{3.16}$$

Because the displacement field is described in local coordinates, derivatives in matrix G can be calculated using:

$$\begin{Bmatrix} \frac{\delta}{\delta x} \\ \frac{\delta}{\delta y} \end{Bmatrix} = [J]^{-1} \begin{Bmatrix} \frac{\delta}{\delta \eta} \\ \frac{\delta}{\delta \xi} \end{Bmatrix} \tag{3.17}$$

where

$$J = \begin{bmatrix} \frac{\delta x}{\delta \eta} & \frac{\delta y}{\delta \eta} \\ \frac{\delta x}{\delta \xi} & \frac{\delta y}{\delta \xi} \end{bmatrix} \tag{3.18}$$

It is important to stress the fact that no smoothing is used to calculate the strains, and accordingly no degradation of spatial resolution in strain is introduced! This is in clear contrast with local DIC methodologies that often use local polynomial smoothing approaches. Previous work indicated that in the subset-based approach nor the derivatives obtained from the Levenberg Marquardt nor the direct derivation from the shape functions can be used to obtain displacement derivatives [30].

3.4.3 Adaptivity

Convergence of the mesh is a key in a good FEA. The same is valid for the global DIC measurement. The displacement and strain field determined by the global (also local) method is the best fit of the mesh, with the allowed degrees of freedom, on the real displacement field. The best fit does not insure that the mesh has enough freedom to sufficiently represent the real deformation field. Correlating a high heterogeneous displacement field with a relative coarse lower order mesh needs refinement to yield an acceptable solution [3]. Refining the mesh, in this context, means adding extra DOF to specific edges/faces, so that the mesh is more suitable for representing the actual field. This way of refinement is called p-refinement. In the hierarchical scheme, three basic degrees of freedom can be added (see Appendix A and Fig. 3.3):

- **Nodal or vertex modes**: are the standard DOF for an iso-parametric four-noded quadrilateral element. The first order element will only contain these DOF.
- **Edge or side modes**: are DOF for each edge separately. All edges in an element can contain different DOF.
- **Element or internal modes**: are extra DOF for one specific element. It only works within an element and does not influence the edges or nodes.

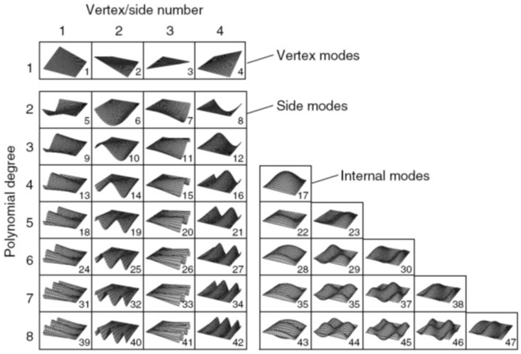

Figure 3.3: Visualisation of Legendre shape functions.[2]

The procedure to refine an element is then straightforward, referring to Fig. 3.3. Each row represents a specific element order. An element from that order contains all the functions in that row and the ones above. To perform refinement, the element enters the next row meaning adding the functions in this new row. Refining from one till three thus means only adding edge modes. Refining to four and higher means adding edge and element modes. This way of updating is possible due to the special nature of hierarchical functions. Higher order functions do not replace lower orders, but are superimposed on to them. This principle of refining is illustrated for a 1D case, thus for one edge in one direction, in Fig. 3.4.

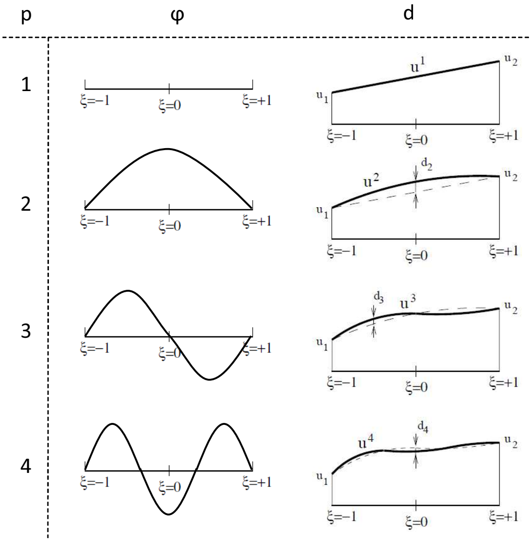

Figure 3.4: 1D representation of the principle of hierarchical shape functions.

By adding extra shape functions, higher order elements receive more DOF. The relationship between order and number of DOF n is as follows;

$$n(p) = \begin{cases} n = 8 \cdot p & \text{if p} < 4 \\ n = p^2 + 3 \cdot p + 6 & \text{if p} \geq 4 \end{cases}$$

The alternative is h-refinement where the elements do not get extra DOF, but the mesh is refined with smaller elements. This refinement is not used for several reasons. First, the elements need a certain size to correlate. Second, the mesh should be regenerated and matrices K should be recalculated. Finally, as it is implemented in other global procedures, refinement is based on user experience. These disadvantages are not present for p-refinement as shown in the previous paragraph.

It is important to note that in our proposed method no uniform updating is done. And thus not simply fixed higher order elements are used. Only the regions where the elements are not able to describe the real displacement, and thus where the *error* is high, will be refined. The refinement (adding orders) is established as follows. The element to be refined contains n DOF, resulting in displacement field $\mathbf{d}$.

$$\mathbf{d} = \sum_{n,a} \Phi_n \, \delta_n \, \mathbf{e}_a \tag{3.19}$$

with

$$[K^n][\delta^n] = [F^n] \tag{3.20}$$

as element equations. When refining the element to $\mathbf{d}'$ by adding m DOF (e.g. updating from p=3 to p=4 then m=5) the displacement field, with $n' = n + m$ DOF, becomes:

$$\mathbf{d}' = \sum_{n',a} \Phi_{n'} \, \delta_{n'} \, \mathbf{e}_a \tag{3.21}$$

Because the shape functions are independent, one obtains

$$\mathbf{d}' = \sum_{n,a} \Phi_n \, \delta_n \, \mathbf{e}_a + \sum_{m,a} \Phi_m \, \delta_m \, \mathbf{e}_a \tag{3.22}$$

Using the equation above in combination with equation 2.8, it can easily be shown that:

$$[K^{n'}][\delta^{n'}] = [F^{n'}] \tag{3.23}$$

where

$$[K^{n'}] = \begin{bmatrix} K^n & K^{nm} \\ K^{nm} & K^m \end{bmatrix} \text{ and } [F^{n'}] = \begin{bmatrix} F^n \\ F^m \end{bmatrix} \tag{3.24}$$

The independence of calculated coefficients is straightforward as the matrix K^n regarding the original element is simply reused in the matrix $K^{n'}$ representing the refined element. This makes refining the element in the global method more efficient. Each time an element is refined with extra DOF, only the coefficients connected to the newly added freedoms are calculated. The remaining coefficients can be copied.

3.4.4 Error estimation

In adaptive finite element analysis, error estimation is a widely discussed topic [60][61]. A lot of research has been done, and multiple approaches are developed. It is now the goal to transfer these estimators to the global method for DIC. In general, two main areas exist in error estimation: a-priori and a-posteriori estimators. In this proposal only a-posteriori error estimation is used [64], because no a-priori information about the experiment is known. Further, no mechanical preknowledge is introduced.

Basically, a-posteriori estimators exist in two groups. Namely recovery or residual based estimators. Recovery based error estimation was proposed by Zienkiewicz et al. [65][66]. The principle is to extract/recover a 'more accurate solution' based on the current solution. The most popular example is the ZZ-estimator [65], where the recovered solution is found by using so-called 'super converged points'. These methods are sometimes called Single Pass Algorithms (SPA) as only one refinement pass is used. After the first calculation, the error is determined using a super convergent solution. Based on this error, the order needed for each element is determined. The calculation is performed again with the updated mesh, resulting in the final results. An other approach is using multiple passes (MPA), where after each calculation an error estimation is done and the mesh is refined [67]. In MPA residual based errors, pioneered by Babuska, can be used where the error is determined by calculating the residual of the finite element solution in each local space. The error estimator implemented is an MPA, as after each correlation run the error will be checked and if necessary elements raised in order. The (local) error in measurand u is defined as:

$$e = u - \hat{u}, \tag{3.25}$$

where e is the local error, u is the exact solution and $\hat{u}$ is the correlated, discretised solution. Measurand u can be displacement, strain or any other quantity of interest. From this local (point wise) error an element error can be determined. In FEA the norm used to describe the element error is the energy norm

$$||e|| = \sqrt{\int_\Omega e^T Le \cdot d\Omega} \tag{3.26}$$

With L the self-adjoined operator. By the lack of material parameters not the energy norm but RMS norm is used. This is valid as scalar norms are similar to the energy norm [3].

$$||e|| = \sqrt{\frac{\int_\Omega e^T e d\Omega}{\int_\Omega d\Omega}} \tag{3.27}$$

If this element error is used as an absolute error, the element should be updated if:

$$||e|| > ||\bar{e}|| \tag{3.28}$$

with $||\bar{e}||$ the permissible RMS error. Another approach is evaluating the element by relative error. Then indicator η is introduced:

$$\eta = \frac{||e||}{||\hat{u}||} \tag{3.29}$$

where

$$||\hat{u}|| = \sqrt{\frac{\int_\Omega \hat{u}^T \hat{u} d\Omega}{\int_\Omega d\Omega}} \tag{3.30}$$

Leading to the updating condition:

$$\eta > \bar{\eta} \tag{3.31}$$

In this way, if the element error is known, elements to be refined are identified. In the following, calculation of the local error is presented. Starting from the definition of error:

$$e = u - \hat{u} \tag{3.32}$$

Based on Zienkiewicz' work [66] the error is approximated by the use of a higher order. Here the higher order solution, one order higher than the current order p, is an approximation for the the exact solution:

$$e \cong \hat{u}^{p+1} - \hat{u}^{p} \tag{3.33}$$

The approximation is valid if it is assumed that the error goes down if the order goes up. Since calculating a higher order solution makes our current (lower order) solution useless, the previous solution is preferred instead of the next:

$$e < e' = \hat{u}^{p} - \hat{u}^{p-1} \tag{3.34}$$

Using this approximation, the error will always be overestimated, which is acceptable as it will yield a more accurate result. This principle, proposed by Zienkiewicz, is common as estimator in p-FE code [68]. To make the estimator independent of the history of the correlation, the error e' can be approximated as [61]:

$$e' \cong \sum_{h} \Phi_h \, \delta_h \tag{3.35}$$

with h denoting the highest orders of the element. Referring to the displacement function (Eq. 3.1) based on shape functions (Fig. 3.3), the h denotes the functions in the last row as seen in Fig. 3.5. If h is defined, e' (Eq. 3.35) can be calculated resulting in element error $\|e\|$ (Eq. 3.27).

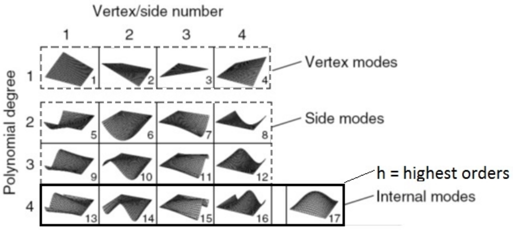

Figure 3.5: Indication of shape functions h used for error estimation.

$$\|e\| = \sqrt{\frac{\int_{\Omega} e'^{T} e' d\Omega}{\int_{\Omega} d\Omega}} \tag{3.36}$$

and if

$$\|e\| > \|\bar{e}\| \tag{3.37}$$

then the element is updated. Note that the same reasoning is used for the relative error η. Because only parameters from the current solution are used, the calculation of the error is very efficient. This estimator can be classified as a MPA method, as at each stage the local error is estimated.

3.4.5 Flowchart p-DIC

To summarise all stated before, a simple flowchart of our new proposed method is shown in Fig. 3.6.

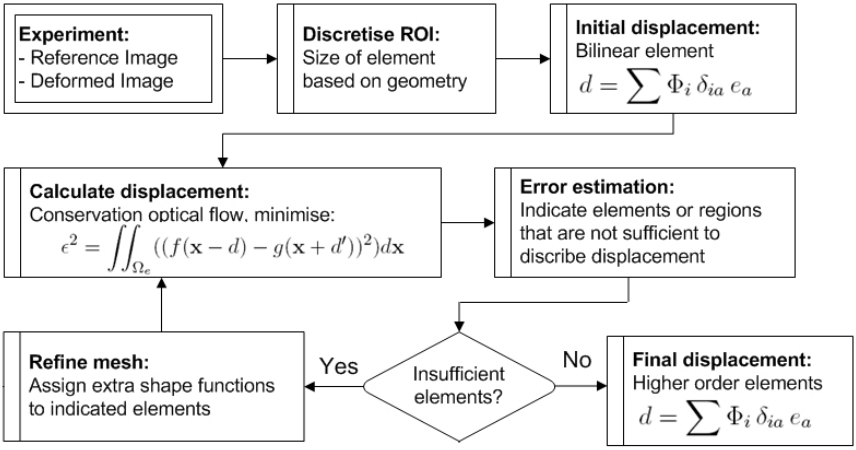

Figure 3.6: Flowchart of the proposed p-DIC method.

3.5 Performance

In previous sections the mathematical framework for the new algorithm was presented. The present section aims at a validation of the proposed algorithm, using measurements and spatial resolution. By way of comparison, the following definitions are firstly presented [69]

- **Measurand**: Object of measurement. Quantity of interest and submitted to the measurement process. In the present application mostly displacement or strain.

- **Resolution**: change in quantity being measured that causes a change in the corresponding indication greater than one standard deviation of the measurement noise. Resolution is comparable to precision.
- **Spatial resolution**: A measure indicating the distance between two independent data points. Spatial resolution is comparable to the detail of the method.

An in-depth comparison of different subset-based platforms has been performed by Bornet et al. [70]. Bornet et al. used sinusoidal deformation fields to assess the metrological performances of image correlation algorithms. Series of sinusoidal deformed images where generated with various frequencies and amplitudes. Results showed that general trends are strongly correlated with the underlying algorithms. A similar approach is used in this comparison, but extensions are done to be applicable for both the local and global method. Comparable images and representations are used. The resolutions and the spatial resolution are plotted in one graph, as the combination of these two quantities indicate the performance of the methods. As can be predicted, both values are inversely related. Achieving a lower spatial resolution leads to an increase of the measurand resolution. For comparison, the platform "MatchID 2D" is used [9]. In the p-DIC method the same libraries for interpolation and mathematical operations are used, leading to a more profound comparison. The influence of filters, interpolation and matrix calculation are ruled out in this way.

3.5.1 Methodology

Parameters

To perform an assessment of DIC, series of synthetic images are used. As reference image, an image of a real speckle pattern (Fig. 3.7) is used. The dimensions of the images are 1200 by 250 $pixels^2$.

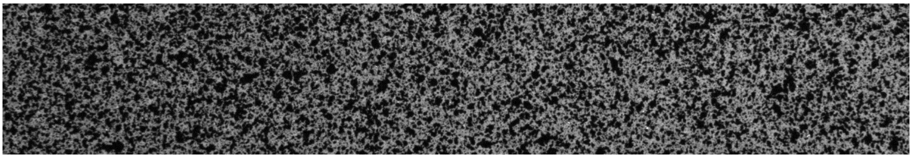

Figure 3.7: Speckle pattern used for validation 1200x250p^2.

As deformed images, numerically deformed images are used. These images are generated by altering the gray level distribution $f(\mathbf{x})$, representing the reference image. If the displacement field is defined by $\Phi_D(\mathbf{x})$, the deformed gray level distribution $g(\mathbf{x})$ is found by following relation:

$$g(\mathbf{x} + \Phi_D(\mathbf{x})) = f(\mathbf{x}) \tag{3.38}$$

The generation of the deformed images is done by using the finite element simulation of the experiment intended to be numerically reproduced [30]. The element size of that mesh is taken small enough to minimise the error. By imposing a known deformation field, the error of the correlation can be assessed in different ways. First a local error is defined.

$$\Delta u(x, y) = u_{imposed}(x, y) - \hat{u}(x, y) \tag{3.39}$$

with $(x, y) \in ROI$. Globally, the root mean square error is defined by

$$RMS_g = \sqrt{\frac{1}{n} \sum_{x,y} \left[\Delta u(x, y)\right]^2} \tag{3.40}$$

The standard distribution and arithmetic mean are defined as:

$$\sigma_g = \sqrt{\frac{n \sum_{x,y} \left[\Delta u(x, y)\right]^2 - \left[\sum_{x,y} \Delta u(x, y)\right]^2}{n(n-1)}} \tag{3.41}$$

$$\overline{\Delta u}_g = \frac{\sum_{x,y} \left[\Delta u(x, y)\right]}{n} \tag{3.42}$$

Finally, some directional parameters are introduced. Directional is defined as using only data in the specified direction. The y-directional standard distribution and arithmetic mean are:

$$\sigma_y(x) = \sqrt{\frac{n \sum_{y} \left[\Delta u(x, y)\right]^2 - \left[\sum_{y} \Delta u(x, y)\right]^2}{n(n-1)}} \tag{3.43}$$

$$\overline{\Delta u}_y(x) = \frac{\sum_{y} \left[\Delta u(x, y)\right]}{n} \tag{3.44}$$

The x-directional parameters are analogously defined.

Measurand resolution

The resolution is determined by using a so-called self-correlation test. Such a test implies the correlation between two images where no deformation is performed. Due to noise and other influences, a deformation field between both images is measured. For that reason the images used are the original pattern (Fig. 3.7) and the same image with an added (numerical) Gaussian noise with a standard deviation of 1%, generally obtained for standard 8-bit cameras. The measurand resolution is defined as the global standard deviation σ_g of the biased measurand field [71].

Measurand spatial resolution

Traditionally, the spatial resolution is defined as the distance between two independent data points [71, 72]. For the local method, the closest distance between two independent data points is the subset size itself. In this case, two neighbouring subsets separated with the subset size from each other will use different pixels and thus remain completely independent. If subsets are closer to each other, they naturally overlap and use common pixels. As such they lose their independence and thus in the subset method the spatial resolution is generally accepted as the subset size. Although this is often confused, the step size only indicates the density in data points. This traditional definition is not applicable to global DIC as the area needed to correlate a data point is not clearly defined. Bornet et al. [70] assessed the metrological performances of different local image correlation algorithms using the sinusoidal deformation fields. As they assess different errors, no clear definition is provided for the spatial resolution. For that reason an alternative indication is used based on the fundamental work of Bornet et al. The spatial resolution will be evaluated as the lowest period (i.e. highest frequency) of a sinusoidal deformation that the method is able to reproduce before losing a certain percentage of amplitude. In this way, a “poor” resolution is a high value and an optimum value is a low one, similar as for the resolution. Thus as deformed image a unidirectional in-plane sinusoidal deformation field is introduced to the original speckle pattern. For displacements this equals to:

$$\Phi_D(\mathbf{x}) = \begin{cases} d_x = a \cdot sin(\frac{2 \cdot \pi}{P} \cdot x) \\ d_y = 0 \end{cases}$$

where a is the amplitude and P the constant period. From this unidirectional in-plane sinusoidal deformation field, a 1D-displacement function R can be extracted using the directional average discussed before.

$$R(x) = \overline{u}_y(x) = \frac{\sum_y [u(x,y)]}{n} \tag{3.45}$$

The function R represents the average sine function the methods (local or global) are capable of reproducing. From the function R the absolute peaks are extracted, denoted as matrix [A], as they represent the reconstructed amplitude. From these peaks average and deviation can be calculated.

$$\sigma_a = \sqrt{\frac{n\sum_p [A]_p{}^2 - [\sum_p [A]_p]^2}{n(n-1)}} \tag{3.46}$$

$$\mu_a = \frac{\sum_p [A]_p}{n} \tag{3.47}$$

The principle is shown in Fig. 3.8. The loss of amplitude is then defined as:

$$\Delta A = \frac{|a - \mu_a| + 3 \cdot \sigma_a}{a} \cdot 100 \tag{3.48}$$

By the use of $3 \cdot \sigma_a$ a certainty of 99.8% on amplitude determination is obtained. As we defined the spatial resolution as the lowest period the method is able to reproduce with an amplitude loss of α, one has

$$Resolution = P \longleftrightarrow \Delta A = \alpha \tag{3.49}$$

where α is the percentage of allowed amplitude loss, which will be the criterion for the spatial resolution determination.

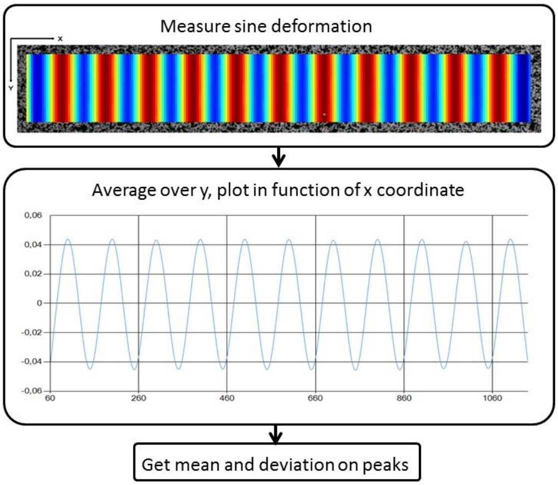

Figure 3.8: Procedure for determining spatial resolution.

By applying this procedure for different frequencies, methods and settings, the loss of amplitude is known as a function of frequency for each setting and method. The graphs resulting from this method are similar as in Fig. 3.9.

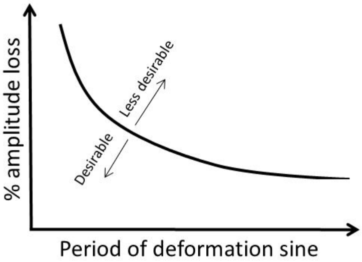

Figure 3.9: Relation amplitude loss vs period of deformation.

In this way the spatial resolution is mathematically determined using only the final deformation field, making it possible to determine the spatial resolution regardless of the method chosen. For this comparison, the error estimation and adaptive meshing are deactivated. This ensures that all settings are maintained to produce a graph similar as in Fig 3.9. If these features were used, the algorithm would update the mesh (higher order) and no loss in amplitude can be measured.

3.5.2 Displacements resolution and spatial resolution

In the following, the resolution and spatial resolution of the displacement is determined for the subset method, the Q8-DIC and p-DIC algorithm. The reference image is the original speckle pattern, the deformed images are the original pattern with an imposed Gaussian noise and unidirectional sinusoidal displacement field. For the resolution a Gaussian noise with a distribution of 1% (2 gray values) is imposed. The in-plane unidirectional sinusoidal displacement field for the spatial resolution has the characteristics shown in Table 3.1.

Parameter	Value
a	5 pixels
P	$50 \xrightarrow{25} 200$

Table 3.1: Deformation parameters for the validation of displacements spatial resolution.

MatchID is used to represent the subset-based approach. The algorithms receive settings shown in Table 3.2.

	Subset method	p-DIC	Q8-DIC
Criterion	NSSD	NSSD	NSSD
Element size (pxl)	$21 \xrightarrow{10} 61$	100 x 100	$200 \rightarrow 20$
Element order	Quad	$4 \xrightarrow{1} 9$	2

Table 3.2: Summarised correlation parameters used in the validation.

The resolution is clearly defined as the standard deviation of the measured artificial displacement field (see section 3.5.1) while measuring the image with noise. The spatial resolution is defined in section 3.5.1. For each combination of method and setting (defined in Table 3.1) the period for a loss of amplitude ranging from 1 to 5 % can be determined and coupled with the displacement resolution for that set-up. The resulting graphs are shown in figures 3.10 ($\alpha = 5\%$) and 3.11 ($\alpha = 1\%$).

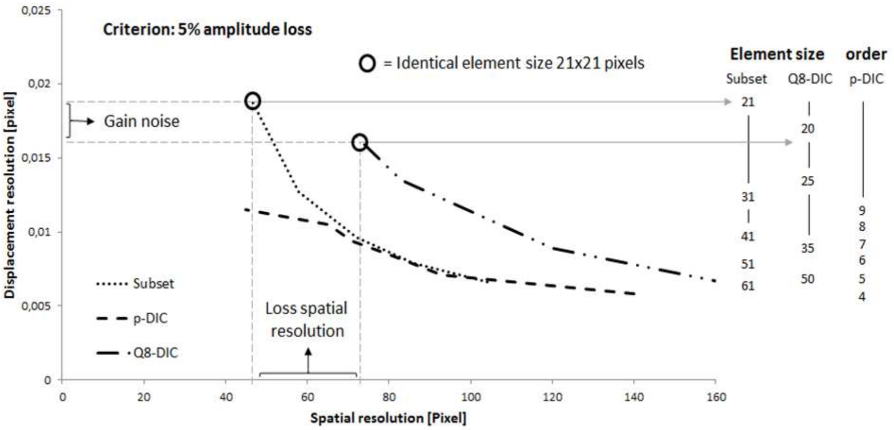

Figure 3.10: Displacement vs spatial resolution for p-DIC, subset method and Q8-DIC. For the local (Q8-DIC) methodology, a decrease in subset dimensions (element size) is adopted horizontally from right to left. The introduced p-DIC, on the other hand, increases the element order from right to left. Spatial resolution criterion $\alpha = 5\%$

Figures 3.10 and 3.11 confirm some intuitive expectations. First of all, the spatial resolution decreases (more heterogeneous deformation) if smaller subsets or higher order elements are taken. Related to the gain in spatial resolution, an increase in resolution is observed. The increase is explained by the rising influence of noise in smaller or higher order elements. Previous research [22] proved that a global approach is less influenced by noise for the same

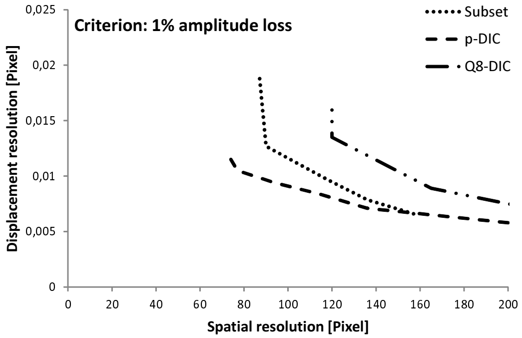

Figure 3.11: Displacement vs spatial resolution for p-DIC, subset method and Q8-DIC. For the local (Q8-DIC) methodology, a decrease in subset dimensions (element size) is adopted horizontally from right to left. The introduced p-DIC, on the other hand, increases the element order from right to left. Spatial resolution criterion $\alpha = 1\%$

element/subset size. However, this investigation did not take spatial resolution into account. Here it is shown that for the same spatial resolution, the Q8-DIC method has a higher displacement resolution than the subset method (different element/subset size). For the p-DIC approach however, at the same spatial resolution, no loss or even a gain in displacement resolution is obtained. Using larger elements with higher orders in the global method keeps the influence of noise low but also lowers the spatial resolution, as more complex deformations can be represented. The graphs also indicate that lowering the criterion α, increases the difference between the subset and p-DIC method. At 1% the difference is larger than at 5%. In general it can be concluded that for low heterogeneous applications (high spatial resolution - right side of Fig. 3.10 and 3.11) the subset, Q8-DIC and p-DIC are competitive. All have similar displacement resolutions for the same spatial resolution. For higher heterogeneous applications (low spatial resolution - left side of Fig. 3.10 and 3.11), the p-DIC has less displacement resolution than the local and the local method less than the Q8-DIC method. For example: at a spatial resolution of 50 and criterion of 5%, the subset method has a resolution of 0.0165, while the p-DIC has a resolution of 0.011. Influence of the amount of the noise has been investigated, concluding that noise shifts both Fig. 3.10 and 3.11 equally up as illustrated in Fig. 3.12. Here the noise level is doubled (form 1% to 2%). The general conclusion is still valid with higher noise values. The data discussed, clearly indicate that for high accurate (low α) low spatial resolutions (low P) the p-DIC method is more favourable than the subset or Q8-DIC method.

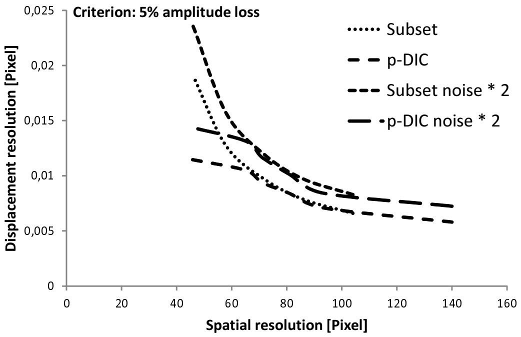

Figure 3.12: Influence of noise on displacement vs spatial resolution for p-DIC and subset method. Spatial resolution criterion $\alpha = 5$

3.5.3 Strain resolution and spatial resolution

The same procedures are followed for the strain resolution and the spatial resolution. The only difference is that not a sinusoidal displacement field but strain field is imposed and that only the subset and p-DIC method are investigated. The in-plane unidirectional sinusoidal strain field for the spatial resolution has the characteristics shown in Table 3.3. For the resolution, again a Gaussian noise with distribution of 1% (2 gray values) is imposed.

Parameter	Value
a	0.05
P	$40 \xrightarrow{20} 200$

Table 3.3: Deformation parameters for the validation of strains spatial resolution.

The configurations for the algorithms are given in Table 3.4.

	Subset method	p-DIC
Criterion	NSSD	NSSD
Element size (pxl)	$21 \xrightarrow{41} 61$	100 x 100
Element order	Quad	$4 \xrightarrow{1} 9$
Step (pxl)	2	pixel
Strain window size	$11 \xrightarrow{10} 51$	n/a
Strain order	Q8	n/a

Table 3.4: Summarised correlation parameters used in the validation.

The resolution is still clearly defined as the standard deviation of the measured artificial strain field (see section 3.5.1). The spatial resolution is defined in section 3.5.1. For each combination of method and setting (defined in Table 3.4) the period for a loss in amplitude ranging from 5 to 15 % can be determined and coupled with the strain resolution for that set-up. The resulting graphs are shown in Fig. 3.13 and 3.14.

The representation of the data will be the same as the plot used for the displacement. Here criteria 5% and 15% are used. Note that the graphs for subsets between 21 and 61 lie between both lines and are left out for obtaining clear graphs.

The data clearly indicate that again lowering the criterion for amplitude loss (determining the accuracy) increases the difference between the methods. The local method was not able to reproduce the strain fields with an accuracy of 5%. Increasing this criterion made comparison possible showing that local and global become competitive. It is also noted that again the strain resolution is lower for the same spatial resolution, with increasing difference if the α is lowered. The same conclusion can be drawn as seen in the displacement resolutions, saying that for high accurate (low α) low spatial resolutions (low P) the p-DIC method clearly outperforms the local method.

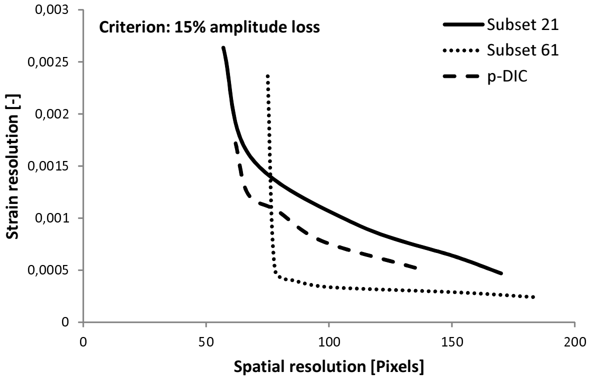

Figure 3.13: Strain vs. spatial resolution for p-DIC and subset method. Spatial resolution criterion criterion 15%

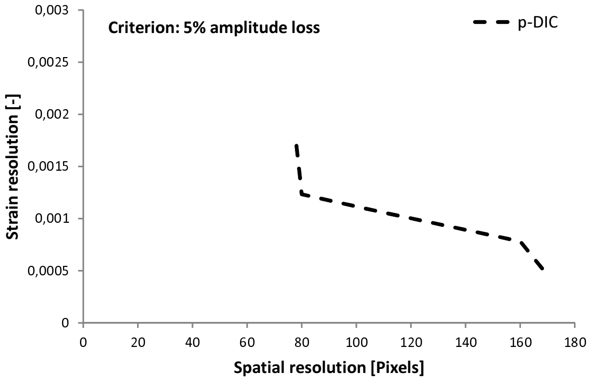

Figure 3.14: Strain vs. spatial resolution for p-DIC and subset method. Spatial resolution criterion criterion 5%

3.6 Full automatic correlation

The p-DIC method, presented in section 3.4, is developed for measuring strains with minimal user dependency in applications producing a high gradient strain field. The validation of the p-DIC method is performed in section 3.5, showing that the p-DIC method is appropriate to be used in these low spatial resolution applications. To minimise user dependency on the results, an error estimator was introduced to adapt the mesh where necessary. Remind that the validation is performed without the error estimator to not alter the spatial resolution of the method. In this section the estimator is activated to prove the concept of the estimator.

The aim is to point out the independence of results obtained by p-DIC. The most important task of the estimator is to identify regions where the mesh is insufficient. Insufficient in this context means needing higher orders to describe the real displacement and thus needing a lower spatial resolution. To test this performance, again a unidirectional sinusoidal numerically deformed image is used. In contrast with previous methodology, a variation in spatial resolution is imposed.

$$\Phi_D(\mathbf{x}) = \begin{cases} d_x = a \cdot sin[\frac{2\cdot\pi}{P_0} \cdot x + (\frac{2\cdot\pi}{P_1} - \frac{2\cdot\pi}{P_0}) \cdot \frac{x^2}{2L}] \\ d_y = 0 \end{cases}$$

Where P_0 is the begin period, P_1 the end period and L the length of the image. In this case $P_0 = 160$ pixels, $P_1 = 70$ pixels and $L = 1200$ pixels. The resulting field is shown in Fig 3.15.

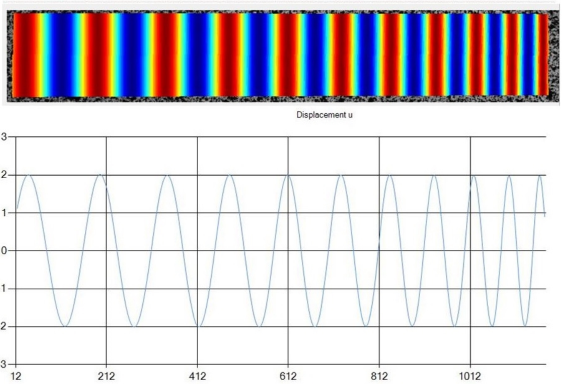

Figure 3.15: Imposed unidirectional sinusoidal displacement field with varying frequency.

With this variation in spatial resolution, a similar variation should be found in the order distribution of the elements. Choosing larger or smaller elements will lead to respectively higher or lower orders. The input for the p-DIC algorithm is shown in Table 3.5.

Parameter	Value
Interpolation	Bicubic
Correlation	NSSD
p-refinement	enabled
Uniform updating	4^{th} order
$\|e\|$	0.05

Table 3.5: Correlation parameters for p-DIC.

These settings have the following proceeding. First, the mesh is uniformly updated until 4^{th} order to prevent severe underestimation of the real displacement. Once the mesh reaches 4^{th} order, the estimator is responsible for updating the mesh. If the element error indicator $\|e\|$ (Eq. 3.36) is larger then $5 \cdot 10^{-2}$ pixels, that element is refined. Running p-DIC with this settings and using element sizes ranging from 50 x 50 to 150 x 150 (= user dependent input), the algorithm yields order distributions as shown in Fig. 3.16.

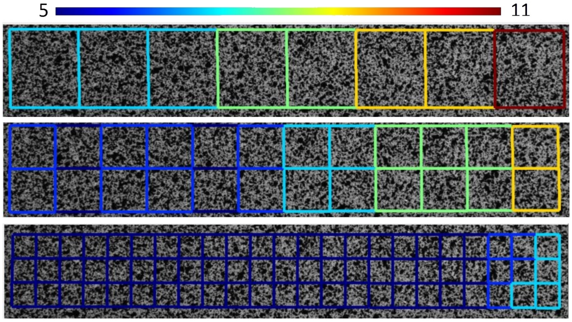

Figure 3.16: Distribution of element orders for the correlation of a displacement field with varying needed spatial resolution for elements ranging from 50x50 to 150x150 pixels.

Based on the indicator (Eq. 3.36), the error plot for element size 100 (middle mesh in Fig. 3.16) is shown in Fig. 3.17. The x-axis represents the refinement loop. The y-axis represents the error indicator value. As seen in the settings, uniform updating is done for four loops, after that the adaptive procedure takes over. Each line on the graph represents an element's indicator in all the loops. The converging behaviour is clearly seen and in loop 9 all elements are converged.

Size	Accuracy	Resolution	Spatial resolution
50 x 50	1.88%	0.72%	1.22%
100 x 100	1.85%	0.50%	1.15%
150 x 150	2.25%	0.37%	2.00%

Table 3.6: Accuracy, resolution and spatial resolution for p-DIC using different element sizes.

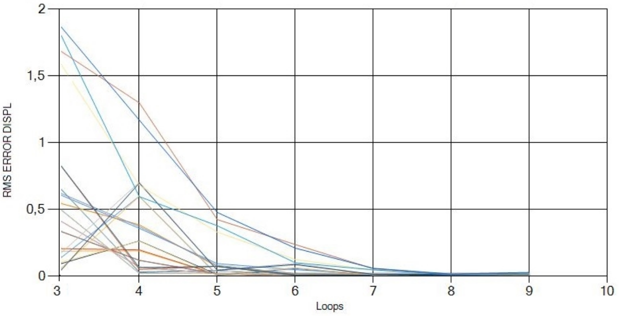

Figure 3.17: Trend error estimation value for correlation with element size 100 x 100.

The convergence graphs for the other mesh sizes are similar. The convergence and order distribution proves that the estimator is able to refine the mesh properly, as needed by spatial resolution. The left side of Fig. 3.16, where the deformation is less heterogeneous, have lower orders than the right side. Also, the large elements are higher order then the small elements. This experiment shows that the measurement is now less dependent on user input. The algorithm will automatically converge to the proper order to represent the real displacement field, and thus having a user independent spatial resolution. This in contrast to the subset method where the spatial resolution is linked to the subset size, chosen by the user. No feedback is given on loss of spatial resolution, in contrast to the p-DIC. In Table 3.6 errors of the correlation for the three mesh sizes are presented. The accuracy is RMS_g (Eq. 3.40) based on the known theoretical imposed displacement field. The resolution is the standard deviation of the measured displacement field obtained by correlating a noised reference image (see section 3.5.1). The spatial resolution is the percentage of amplitude loss in the reconstruction of a sinusoidal displacement field (see setion 3.5.1).

The results, shown in Table 3.6, indicate a clear conclusion. Starting with a bigger mesh influences the spatial resolution slightly. The spatial resolution only rises 0.78% for an element area increase of 900%. The estimator will update the mesh till convergence, and thus till the mesh is able to reproduce the real displacement. The resolution slightly increases when smaller elements are taken. As the accuracy is a combination of resolution and spatial resolution the same conclusion holds.

Using the p-DIC method, one thus chooses the biggest mesh possible. If the correlation does not converge, a smaller mesh should be chosen. If the method converges, one is sure that regardless of the mesh chosen the spatial resolution is low enough if the setting for the estimator is appropriate. By using the biggest mesh that has convergence, one obtains a solution with sufficient spatial resolution and the lowest resolution.

3.7 Application to a tensile test

For a more realistic situation, a tensile test is numerically simulated. Noise is introduced to be as realistic as possible. A perforated aluminium specimen is used, producing a heterogeneous strain field. Extensive research has been done by Wang et al. [34] for selecting correct correlation parameters for the subset method. It is stated that the choice of parameters is critical for reaching the optimum between noise reduction and spatial resolution. For the experiment the same artificial images as in [34] are used, so the same optimum parameters can be selected for the subset method. The used images are shown in the Fig. 3.18 where the left image represents the reference image and the right the deformed image.

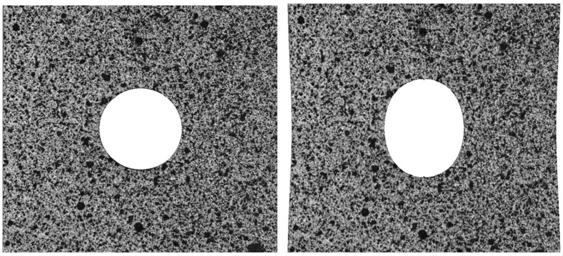

Figure 3.18: Numerically simulated tensile test with imposed noise. On the left the reference image, on the right the deformed image.

As stated by Wang et al. this experiment has an optimum subset size of 25 with affine shape function (based on speckle pattern, noise, strain state, criterion

Criterion	NSSD	-
Interpolation	Bicubic	-
Shape function	Automatic update	-
Min order	4	-
Element size (pxl)	100 x 100	$pixel^2$
$\|\|e\|\|$	0.025	$pixel$

Table 3.7: Correlation parameters p-DIC.

...). The strain window should be bilinear with size 9. For p-DIC, the settings shown in Table 3.7 are used.

Notice that the choice of element size is not critical. Uniform updating is performed until 4th order and the estimator will refine the mesh automatically. Thereby, data is less user dependent, as each correlation starts with the same settings (error estimator) and adapts itself during the correlation. Also, both methods use the same interpolation library to make the comparison more profound. As the images are numerically deformed, the theoretical displacement and strain field is known. Based on these fields, the distribution of the errors are shown in Fig. 3.19 till Fig. 3.22. The error is defined as the difference between imposed an measured deformation.

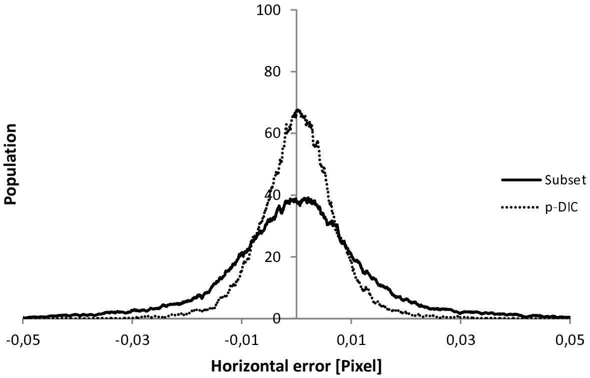

Figure 3.19: Distribution absolute error horizontal displacement for tensile test on holed specimen using subset and p-DIC.

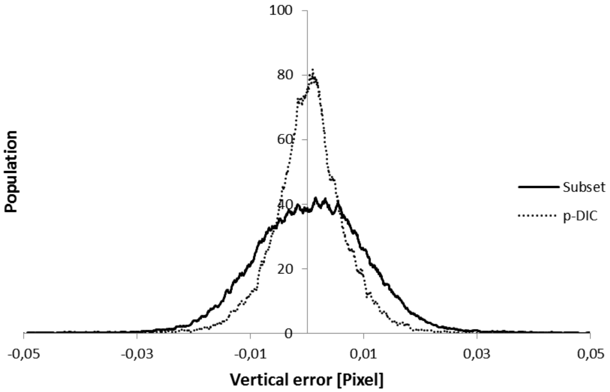

Figure 3.20: Distribution of error in vertical displacement for tensile test on holed specimen using subset and p-DIC.

The first conclusion to be drawn from Fig. 3.19 and 3.20 is that the distribution of the error in p-DIC displacements has less variance than the ones from the subset method, although for this method the optimal settings where used. Remark that these optimal settings for the subset method can only be found by the knowledge of the "true" deformation. Development of an experimental simulator is on its way so that different settings can be checked, yielding the optimal correlation parameters [73]. Currently obtaining these parameters is not possible yet and the settings have to be estimated by user experience. Even if the simulator was used, again user dependent input will be needed in the simulator (model, noise, material, ...) whereas the p-DIC refines only based on the experimental data without any model or pre-knowledge.

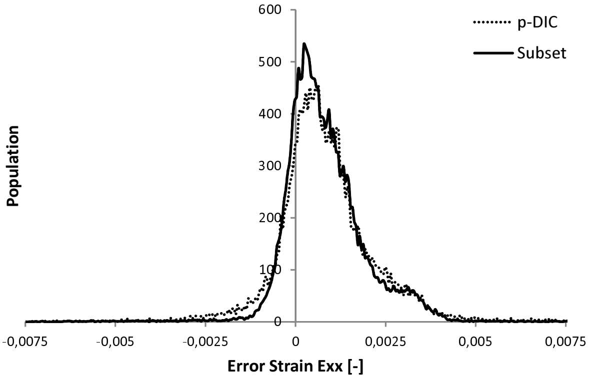

Figure 3.21: Distribution of error in strain Exx for tensile test on holed specimen using subset and p-DIC.

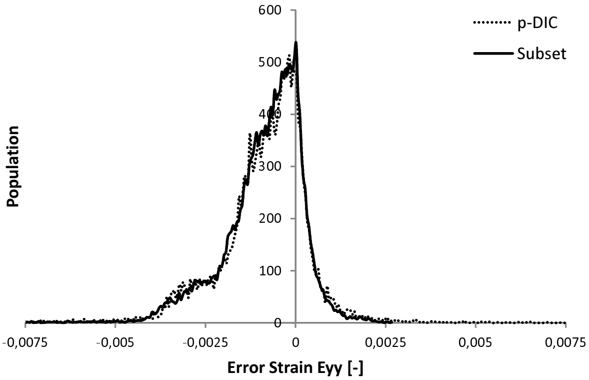

Figure 3.22: Distribution of error in strain Eyy for tensile test on holed specimen using subset and p-DIC.

Secondly, Fig. 3.21 and 3.22 show that the use of a strain window greatly improves the accuracy despite the noisy measurement. The results (variance) for displacement field are better (smaller) for the p-DIC method than the subset method. More accuracy is obtained in the strain field by smoothing the displacement field until calculated strains are acceptable. The accuracy is here obtained by applying the correct filter, dependent on the used step and strain window, and is thus very user dependent. This effect of change in data is shown in the Fig. 3.23.

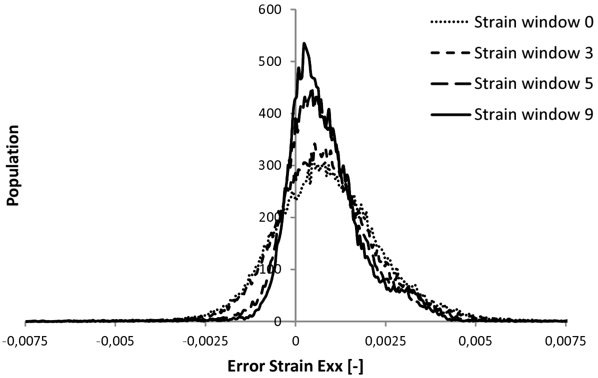

Figure 3.23: Distribution of error in Exx using various strain window sizes for tensile test on holed specimen.

The graph clearly shows the change in error, if the strain window is changed. Increasing the window reduces the noise effect, reducing the variance. Remark that if even larger strain windows were used, the error distribution starts widening again due to the lack of spatial resolution. For this reason, increasing the size of the window is limited by the spatial resolution, which is not known in a normal test. There thus exists a window of acceptable values which is not known, making it cumbersome to find these acceptable settings. Because the p-DIC obtains the derivatives directly, without any smoothing, this problem does not occur.

To prove the statements made earlier the same graph is produced for the p-DIC where the mesh ranges from 75 x 75 to 200 x 200 pixels resulting in Fig. 3.24 representing the change in error in function of the mesh choice. Other settings like $||e||$ and uniform updating order are not altered.

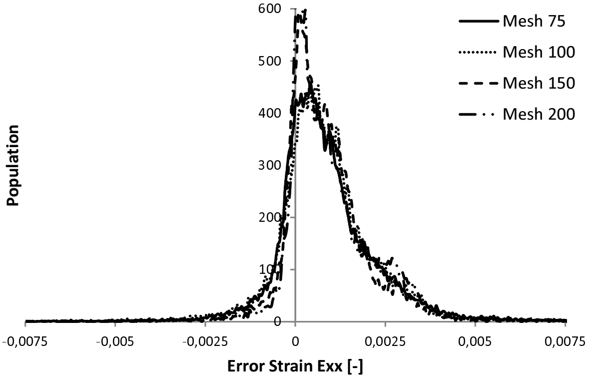

Figure 3.24: Distribution of error in Exx with various element sizes for tensile test on holed specimen.

The graph confirms the conclusions made earlier: the p-DIC method is less dependent of user's input than the subset method. There is a small change in the error distribution for an extreme range of elements (area increment of 700%). The smallest and biggest elements are shown in Fig. 3.25. Although the use of small elements (size 75) is less favourable (see section 3.6), the method still yields acceptable results comparable to the optimal subset size. As stated before, larger elements are more favourable for the p-DIC method, as noise has less influence and thus large elements have to be used. Once the elements are large and convergence is reached, the difference between element sizes is minimal (size 125 x 125 till 200 x 200). The size is limited by the geometry of ROI or the lack of convergence indicated by the estimator. Still keep in mind that although for the p-DIC methods the least favourable settings where used, similar results are obtained as by the subset method (see Fig. 3.21 and 3.22).

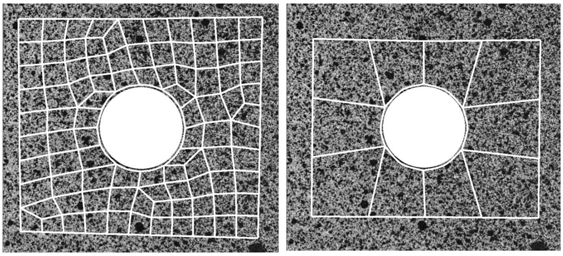

Figure 3.25: Left: Mesh size 75 x 75. Right: Mesh size 200 x 200 pixels.

3.8 Conclusion

In this paper a new global DIC algorithm has been presented. The algorithm adopts features from the concept of adaptive FEA. The region of interest is described by an adaptive element mesh. A p-refinement scheme is implemented so that the elements in the mesh are capable of rising in degrees of freedom when the error estimators indicate them to do so. Using measurand resolution and spatial resolution, a validation of the traditional local and newly presented p-DIC is performed. Results from the validation indicate that the p-DIC method has a lower measurand resolution for the same spatial resolution compared to the local method. Also from the strain validation it can be concluded that for the accurate measurement of low spatial strain fields the p-DIC method is more favourable than the local method. Besides the advantage in performance at optimal settings, an other major advantage is that the method becomes less user dependent by using the self-adapting mesh. The spatial resolution is, in comparison to the local method, not limited by initial user settings. Future work is mainly aimed on the further development of the error estimators as they are key in the p-DIC procedure.

Chapter 4

Convergence in Global DIC

Chapter 3 presented a framework for an adaptive DIC method. This chapter will introduce how this adaptive method is made self-adaptive. Principles from the adaptive FEA are briefly explained and transferred to the DIC method. The robustness of the self-adapting algorithm is validated in both numerical as practical experiments.

Wittevrongel L., Debruyne D., Lomov S.V. and Lava P. Implementation of Convergence in Adaptive Global Digital Image Correlation. *Experimental Mechanics, submitted.*
Some parts of the original publication are left out to avoid redundancy.

4.1 Abstract

In global digital image correlation (DIC) a finite element mesh is used to describe the deformation of the region of interest (ROI). However, the identification of an optimal mesh is a difficult problem and is often obtained by using "mechanical" pre-knowledge of the solution. In Finite Element Analysis (FEA) an optimal mesh can be found without any pre-knowledge of the solution by using mesh adaptivity, where an initial (non optimal) mesh is refined until the optimal solution is obtained. Refinement of the mesh can be based on error and/or convergence estimators. In the present article the convergence procedure is transferred to a recently published global DIC method. In the used global DIC method elements can receive higher order shape functions, also known as

p-elements. Using the aforementioned algorithm, also called p-DIC, refinement to a non-uniform higher order mesh is possible. Using the non-uniform mesh, an optimal mesh can be obtained for each section of the ROI. The presented study shows that, analogous to adaptive FEA, a convergence scheme can be used to automatically control the mesh refinement in a global DIC approach. The convergence boundary, in percentage, is a more intuitive boundary than the absolute error boundary used in the original p-DIC approach. The procedure is validated using numerical examples and the robustness to experimental variables is investigated. Finally, the complete procedure is tested against a wide range of practical examples.

4.2 Introduction

Full field measurements are used in experimental mechanics to make the connection between simulations and experiments. The measured deformation field can be used for several purposes such as model validation or material identification [74]. One of the most popular techniques to measure this full field deformation field is Digital Image Correlation. DIC has a traditional subset-based (local) approach where each pixel is tracked between the reference and deformed images using the pixel itself and its neighbouring pixels [1]. One problem related to the local approach is the selection of the optimal subset size. It should be large enough to contain sufficient features while - at the same time - small enough to represent the underlying deformation [30]. In the literature, quite some research has focussed on the optimal subset size, proposing a particular subset size for a certain speckle pattern [32][33]. Due to the difficulty in selecting an appropriate subset size, results can considerably depend on this user setting which is not desirable in experimental measurements. One possible solution is to use so-called adaptive subsets [75], a principle widely used in stereo matching of multiple cameras. In most implementations, the so-called multiple window approach is used [76][77][78][79]. Here, for each pixel a collection of different subsets is matched and the one with the best correlation coefficient (e.g. Sum of Squared Differences) is retained. More than varying the subset size, also shape functions can be altered in the collection of subsets [18]. In such an adaptive scheme, a correlation is performed for both linear and quadratic subsets. In the final results, the displacement of the subset resulting in the best correlation coefficient is used for the considered pixel. These adaptive principles reduce the influence of the initial subset, but do not overcome another main disadvantage of the subset approach. As each pixel is retrieved individually, the measured points remain independent resulting in a non-continuous displacement field. An alternative method, namely "global approach", is available in DIC where a complete element mesh is tracked on the images. By using a finite element mesh, this method insures C^0-continuity, resulting in less noise influence. The problem of the ideal element size however, remains cumbersome. Any finite element mesh generates discretisation errors [60]. In global DIC, the same discretisation occurs and a best fit of the current mesh and its degrees of freedom (DOF) is made on the actual displacement field [70]. The use of a mesh containing not enough DOF results in a smoothed best fit displacement field. In this way, a suitable mesh is an absolute requisite in global DIC. Most global procedures make use of a fixed order mesh [22], resulting in the fact that refinement of the mesh can only be achieved by reducing the element size, also called h-refinement. Recently, a new approach has been introduced, containing adaptive hierarchical higher order elements [80]. The latter is capable of coping with a non-uniform higher order mesh, where the element order is not limited. In this way, refinement can be done by increasing the element order instead of reducing the element size. From here on this method will be called p-DIC. The refinement is based on adapting all the elements having an error larger than a certain threshold. The value of this threshold however is absolute and rather difficult to determine as it can be different for different correlations.

The purpose of this article is to introduce a procedure for driving the automatic procedure within the p-DIC method. The procedure will be, similar to the FEA, based on convergence of the elements/mesh [3]. The refinement procedure automatically adapts the mesh, initially determined by the user, to eventually obtain a converged mesh for representing the real deformation field occurring in the experiment. By using convergence, the user input is instead of an absolute error threshold, a more intuitive convergence boundary, classically known from FEA.

The article is organised as follows. In section 4.3, the p-DIC algorithm is briefly repeated and the refinement procedure is explained. The principle and implementation of the convergence procedure are given in section 4.4. Section 4.4 also provides an illustrative example as proof of concept. In section 4.5 a study is performed on the robustness of the procedure. Finally, in section 4.6, numerical and real experiments are performed to test the new refinement procedure within the global DIC approach.

4.3 Adaptive global digital image correlation

Omitted to avoid redundancy, see Chapter 3.

4.4 Convergence into p-DIC

The main problem of the current refinement procedure implemented in the p-DIC method, is the determination of the boundary value $\|\bar{e}\|$. This is an absolute value, having no physical meaning and thus hard to determine. To make the procedure more intuitive and even more user independent, a relative error bound should be introduced instead of the used absolute error bound. In this way, in analogy to FEA, a solution with 5% (or more) accuracy can be requested. In this section, a convergence procedure is introduced to the p-DIC method in order to obtain the relative error indication and thus make the refinement procedure even more autonomous.

4.4.1 Convergence procedure

In FEA, refinement of the mesh is often driven by convergence of the element energy [81]. The refinement procedure of the finite element mesh (introducing extra DOF) continues until the element energy for all the elements is converged. As stated before, the introduction of extra DOF will be done by increasing the element order (p-refinement).

To obtain an appropriate mesh in the p-DIC method, a similar approach is followed. The convergence procedure is based on the convergence of element strain energy. Since in p-DIC no material parameters are known, the exact strain energy (Eq. 4.1) cannot be calculated.

$$E^e_{Exact} = \iint_{\Omega_e} \varepsilon^T D \varepsilon \, d\Omega \tag{4.1}$$

It is well-known that for elastic material behaviour the energy norm and L2 norm are equivalent and thus have the same convergence properties [3]. Consequently, not the real energy (Eq 4.1) but an $L_2 - norm$ will be used to find convergence in global DIC.

An element keeps being refined until its norm of strains converges. For the mesh, refinement continues until all elements are converged. When some elements do not converge in the strain norm, for example when a certain maximum order is achieved, the correlation can be restarted using the displacement field in the convergence procedure. The previous is proposed because in a finite element mesh the displacements have a convergence rate of $O(h^{p+1})$ while the m^{th} derivative of displacement has a convergence rate of $O(h^{p+1-m})$, where h denotes the element size and p the polynomial order. Consequently, the rate of convergence in displacement ($m = 0$) is one order higher than the rate of convergence in strain ($m = 1$) [81]. When the elements do not converge in the displacement norm, the final option is to use global norms. Here, a global strain or displacement norm over the entire ROI is used to control the mesh refinement. It should be noted that when using the global norms, all the elements have the same global convergence curve, and thus the algorithm will only perform uniform refinement. A global convergence procedure improves stability, but has less performance as the elements are not optimised individually. The hierarchy in convergence norms is given in Table 4.1.

	Norm	**Type**	**Energy area**	**Refinement**
1	$E_\varepsilon^e = \iint_{\Omega_e} \varepsilon^T \varepsilon \, d\Omega$	Local	Element	Element by element
2	$E_\varepsilon^e = \iint_{\Omega_e} u^T u \, d\Omega$	Local	Element	Element by element
3	$E_\varepsilon^e = \iint_{ROI} \varepsilon^T \varepsilon \, d\Omega$	Global	ROI	Uniform
4	$E_\varepsilon^e = \iint_{ROI} u^T u \, d\Omega$	Global	ROI	Uniform

Table 4.1: Hierarchy in convergence norms used in the convergence procedure.

Based on the convergence of the norms presented in Table 4.1, an automatic refinement procedure can be implemented. The use of a convergence procedure for each element e separately, results in a non-uniform mesh where all the elements have the most beneficial polynomial order without any pre-knowledge of the experiment's mechanical behaviour.

4.4.2 Algorithm

The implementation of convergence procedures into the global DIC procedure is illustrated in the flowchart, shown in Fig 4.1.

If the standard convergence procedure is adopted, the choice of element size is the only user dependent input in the algorithm. As the mesh is automatically refined, based on the convergence of element L_2-norms, the element size will have minor effect on the final results. The use of convergence instead of the previously implemented error estimators has the major advantage that no absolute error bound has to be defined, but a more intuitive convergence boundary (similar as in adaptive FEA) is used to obtain a suitable mesh.

4.4.3 Practical Approach

A correlation will always follow the same scheme:

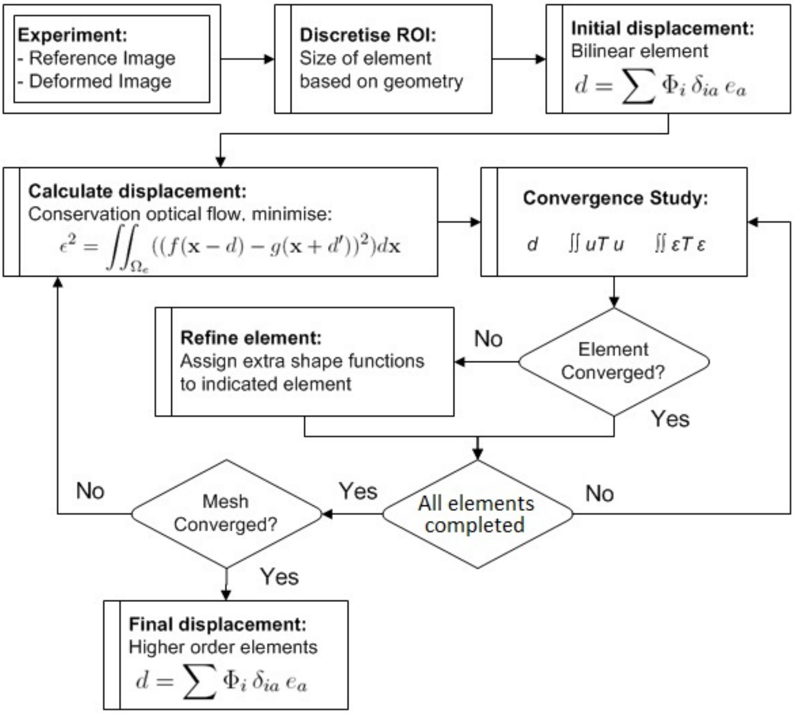

Figure 4.1: Flowchart of convergence into p-DIC.

- **Select a mesh size:** The user draws the ROI and selects an element size. In practice, the user should use an element size that generates a mesh which is able to reproduce the specimen geometry. In this way, complex geometries should be represented by smaller elements than simple geometries.
- **Select convergence criteria:** In normal situations the convergence criterion is set-up by default at 5% convergence in the strains L2-norm, a boundary commonly used in the adaptive FEA. The mesh is refined until convergence in the strain norm for each element is achieved. More experienced users can modify the convergence procedure and convergence criteria to boost the performance of the updating procedure. The improvement of the procedure can be based on the returned convergence curves and error graphs of the standard correlation.

In most of the cases the strain energy will converge. However, if for some elements the criteria did not converge, it can be checked whether the elements are critical for the user. If not, the results can be accepted although some elements in the mesh are not converged. If the elements are critical for the user, the convergence boundary can be increased or decreased in order to find convergence in those elements. If increasing the boundary does not resolve into a converged mesh, the convergence norm can be adapted following the scheme given in Table 4.1.

4.4.4 Refinement illustration: example

The principle of convergence in global DIC is illustrated in a numerical test. The performed test lacks experimental meaning, but illustrates the performance of the refinement procedure in the global DIC approach. A sinusoidal displacement field with rising frequency is imposed on a reference image. The change in frequency ensures a change in spatial resolution and thus a mesh refinement can be expected. The deformation field is defined as:

$$\Phi_D(\mathbf{x}) = \begin{cases} d_x = a \cdot sin[\frac{2\cdot\pi}{P_0} \cdot x + (\frac{2\cdot\pi}{P_1} - \frac{2\cdot\pi}{P_0}) \cdot \frac{x^2}{2L}] \\ d_y = 0 \end{cases}$$

Where P_0 is the starting period, P_1 the end period and L the length of the image. In this case $P_0 = 160$ pixels, $P_1 = 70$ pixels and $L = 1200$ pixels. The gray level distribution for the deformed image $g(\mathbf{x})$, is found by using the gray level distribution of the reference image $f(\mathbf{x})$, shown in Fig 4.2, and the following relationship:

$$g(\mathbf{x} + \Phi_D(\mathbf{x})) = f(\mathbf{x}) \tag{4.2}$$

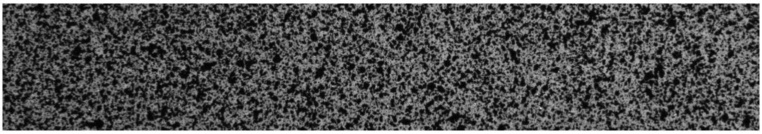

Figure 4.2: Reference image used to impose a sinusoidal deformation field.

To resemble the user input, different mesh sizes are used to correlate the numerical images. A wide range in element sizes is taken to cover all (reasonable) user settings. The mesh sizes used are: 50 x 50 pixels, 75 x 75 pixels, 100 x 100 pixels, 125 x 125 pixels and 150 x 150 pixels. The meshes are shown in

Criterion	NSSD
Interpolation	Bicubic
Shape function	Automatic update
Min order	4
Convergence procedure	$E_{\varepsilon}^{e} = \iint_{\Omega_e} \varepsilon^T \varepsilon \, d\Omega$
Convergence criterion	5%

Table 4.2: Standard correlation parameters for the p-DIC approach.

Appendix C. The correlation settings are independent of mesh size and are summarised in Table 4.2.

In these settings, the minimum and maximum order are important; however not influencing the final results. The minimum order insures that the initial mesh is uniformly refined to a fourth order mesh. The minimum order is needed to improve the robustness of the refinement procedure and to avoid severe underestimation of the displacement field. It provides a lower bound that does not interfere with final results.

The reference image (Fig. 4.2) is correlated with the numerical deformed image, results in a measured deformation field for each mesh defined before (50/75/100/125/150). The refinement procedure refines each mesh until all elements are converged. As a result, all elements are able to describe the deformation field correctly. In Fig. 4.3 the distribution of element polynomial order is given as a function of the x-coordinate. The element order is only a function of the x-coordinate because in the y direction no deformation is introduced and thus the order of elements along the y direction remains constant.

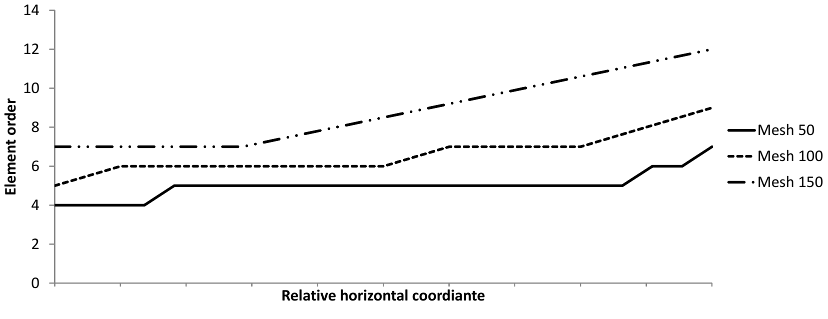

Figure 4.3: Trend of element orders in function of horizontal coordinate in the illustration example for mesh sizes 50, 100 and 150.

Fig. 4.3 confirms the user's instinct. Going from $x = 0$ to $x = 1200$ the rising frequency invokes higher element orders. For all the element sizes this rising trend is noticed. Further it is confirmed that using larger elements result in higher orders, as they need more degrees of freedom (DOF) to describe the same deformation field. The convergence curves for element size 100 x 100 pixels are shown in Fig. 4.4.

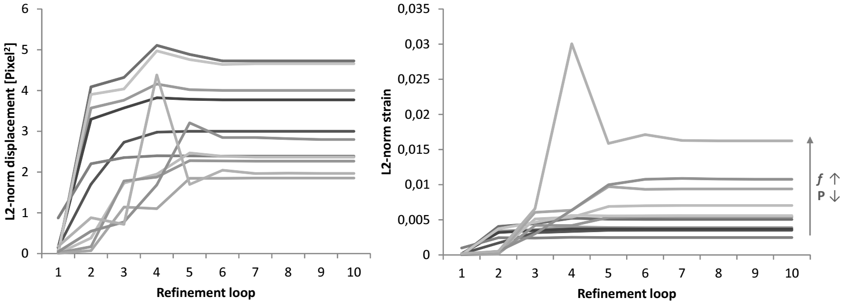

Figure 4.4: Convergence curves for all 11 elements of 100 x 100 mesh. Left represents L2-norm in displacement, right L2-norm in strain.

Fig. 4.4 allows for some interesting conclusions. Indeed the element displacement and strain norms converge when the element is refined. The L2-norm in strain, shown in Fig. 4.4 on the right, indicates that some elements converge faster than others. When element curves are linked to the mesh geometry and deformation (see Fig 4.5), it is seen that the elements that converge fast are located on the left of the image where the deformation is less complex and where, consequently, the orders are expected to be lower.

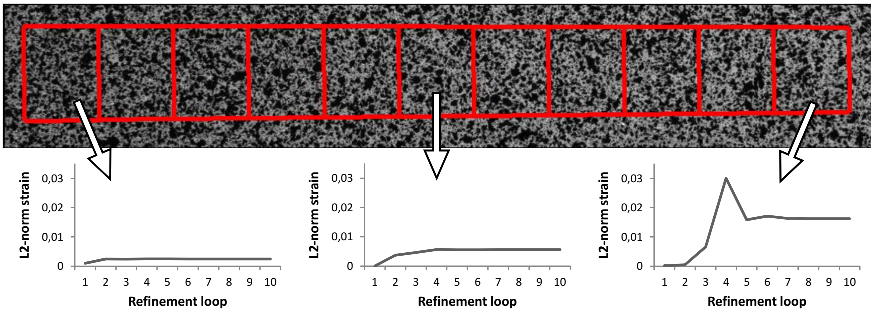

Figure 4.5: Strain convergence curves for 3 elements (left, middle and right) of the 100 x 100 mesh with there location in the finite element mesh.

The results from all meshes can be compared to the known imposed displacement field to obtain the local error. The average and standard deviation of the error in horizontal displacement are shown in Table 4.3.

	μ	σ
50	< 0.001	0.0113
75	< 0.001	0.0121
100	< 0.001	0.0172
125	< 0.001	0.0123
150	< 0.001	0.0147

Table 4.3: Mean and deviation of horizontal displacement error in the illustration example for element sizes varying from 50 to 150 pixels.

Table 4.3 clearly indicates the minimisation of user independence of the final results. An element area increase of 900% results in almost no change in distribution of the error. It should be remarked that only the horizontal displacement is discussed as this is the primary direction.

In the remainder of the present paper, when presenting correlation results, no comparison to the "correct" solution or to other methods such as the local subset method will be performed. In previous work a complete comparison between the "correct" value, the subset method and the p-DIC method has been done [80]. To recapitulate, it was shown that for homogeneous applications the performance in terms of spatial and displacement resolution the p-DIC and local subset method were competitive. For heterogeneous applications though, the p-DIC method has a considerably large gain in displacement resolution for the same spatial resolution. Furthermore, it is illustrated that the results obtained by the p-DIC method are considerably less user dependent. For the local method it is widely known that the initial correlation parameters, such as subset size and strain window, influence the results heavily [30].

4.5 Performance of the procedure

The concept of using a convergence procedure for driving the refinement procedure has been demonstrated in Section 4.4. In the following, the robustness of the refinement procedure against experimental conditions is checked. The parameters taken into account are noise, light conditions, correlation criterion and camera rotations. After numerically imposing these experimental influences onto the deformed images, it can be checked whether the procedure was able to reconstruct the reference order distribution obtained in Fig 4.3. The same order distribution is found when the final mesh contains as many DOF as in the reference case. The number of DOF N for a certain mesh can be found using Eq. 4.3.

$$N = 2n_n + \sum_{e=1}^{n_e} 2(p_e - 1) + \sum_{f=1}^{n_f} \sum_{i=5}^{p_f} i - 4 \tag{4.3}$$

Here n_n, n_e and n_f represent the number of nodes, edges and faces in the mesh. p_e and p_f define the polynomial order of the indicated edge or face. In this validation the mesh with element size 100x100 pixels is used. The order distribution indicated in Fig 4.3 contains $N = 634$ DOF.

4.5.1 Noise and Light conditions

To check the performance of the refinement procedure against noise, Gaussian distributed noise with a deviation ranging from 0 to 10 gray levels is imposed onto the image. The DOF of the final mesh, equivalent to the reconstructed order distribution, remained at 634 DOF. The reconstructed order matched the reference order where no noise was present.

Secondly, the effect of light changes are checked by imposing a brightness change, ranging from 0 to 40 gray levels, onto the deformed image. Again, the DOF of the final mesh obtained in different light conditions was 634. This indicates that noise and light conditions, within reasonable limits, do not influence the procedure's performance and that the same optimal mesh is achieved. As third influence, the correlation criterion was varied between SSD and NSSD. Once again, it became clear that changing the criterion to SSD does not influence the order distribution.

To conclude, it can be stated that the refinement procedure is capable of handling all kinds of experimental changes in the images. Hence, the refinement procedure is not tempted to follow noise or is not influenced by light conditions and correlation criterion. The final order distribution is only dependent on the underlying deformation. Remark that this does not mean that the correlation itself is not influenced by these parameters. The quality of the measurement will decrease, i.e. σ will increase. Only the refinement procedure is not influenced and is still able to indicate the correct element orders.

4.5.2 Camera rotations

The performance of the convergence procedure in a 2D setup is shown above. As a last step in the validation stage, the method's potential for a 3D DIC set-up is investigated. The most important step in 3D DIC is the cross correlation between cameras, as they provide the stereo view. To check whether this correlation method is able to achieve the cross correlation, a circular specimen is captured with two cameras. The position of the cameras is varied to obtain multiple stereo set-ups. The experimental set-up shown in Fig 4.6. To obtain a change in the pan angle, angles θ_0 and θ_1 can be adjusted. To obtain a twist angle, angles γ_0 and γ_1 can be adjusted.

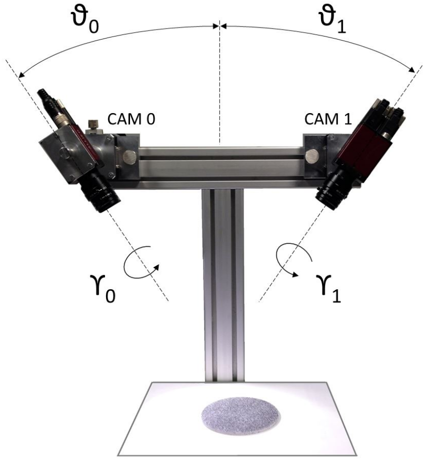

Figure 4.6: Experimental setup for performing cross correlations with p-DIC.

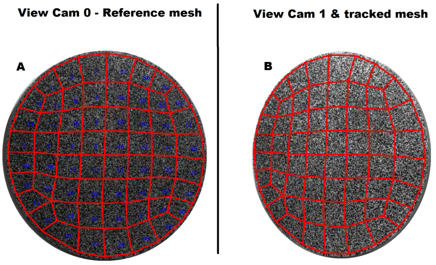

Figure 4.7: Illustration of the tracked mesh in the cross correlation for $\theta_0 = \theta_1 = 30°$.

Angles θ_0 and θ_1 range both from 0° to 30°. Using the standard correlation settings, shown in Table 4.2, p-DIC was able to perform the cross correlations for all set-ups. For illustrating the results, the tracked mesh in the most outer situation is presented in Fig 4.7.

A second possible rotation is around the camera axis. Now, $\theta_0 = \theta_1 = 0°$ but γ_1 is varied from 0° to 60°. The image obtained from camera 0 is used as reference image, images obtained by rotating camera 1 are used as deformed images. The tracked meshes at different rotation angles are illustrated in Fig 4.8.

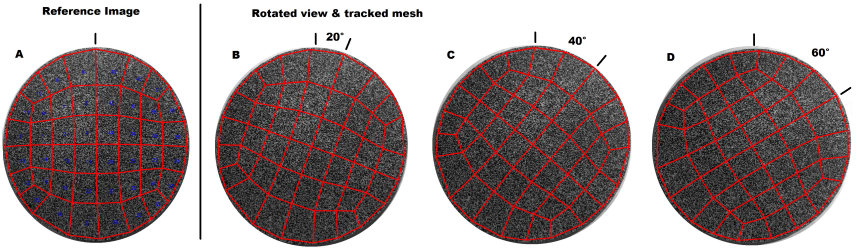

Figure 4.8: Illustration of the tracked mesh in the cross correlation for $\theta_0 = \theta_1 = \gamma_0 = 0°$ and γ_1 ranging from 20° to 60°.

It is seen that the p-DIC method using the convergence procedure is able to correlate a wide range of dual camera set-ups. Both pan as twist angle (θ and γ) were varied from 0° to 60°. The camera rotations were treated as a standard correlation and thus automatic mesh refinement was allowed. In each set-up, a uniform 4^{th} order mesh was obtained due to the standard settings (Table 4.2), where the mesh is bounded to minimum 4^{th} order elements. In each set-up, no further refinement was performed by the procedure as a cross correlation is a second order displacement field. Results also indicate that the allowed twist angle can be substantially larger than for the subset method. In the local approach, decorrelation occurs at approximately 20° [1] while the p-DIC method was able to cross correlate until 60°.

4.6 Applications

In the previous sections it became clear that convergence procedures can be used to independently determine the element order distribution for a certain mesh used in a global digital image correlation algorithm. Again, it should be stressed that it is shown that the final results are in a large extent mesh or deformation independent and does not use any pre-knowledge. Also it was shown that the procedure is able to cope with varying experimental situations. To finalise the validation of the automatic refinement procedure, several experiments are conducted. For each test, results from the correlations are compared to a FE simulation. As boundary conditions, the displacement of the edges of the specimen are applied. The material parameters are determined using standard tensile tests in the rolling-, transverse-, and 45 degree direction. As plastic behaviour, a swift hardening law is used and anisotropy is implemented using Hill 48 yield criterion. The identified parameters are shown in Table 4.4.

Young's Modulus	150 MPa
Yield stress	163 MPa
k	508
ϵ_0	0.009
n	0.25
Hill F	0.45
Hill G	0.30
Hill H	0.70
Hill N	2.13

Table 4.4: Identified material properties.

It should be noted that the simulations are not used to do a quantitative evaluation of the results. The purpose is to see whether the deformation field is qualitatively good represented by the refined mesh.

First, a numerical experiment is conducted to check the feasibility of automated refinement on heterogeneous strain states. In the next step, real experimental images will be used to validate the refinement procedure.

4.6.1 Application 1: Numerical tensile test

Numerical images are created, representing a perforated specimen loaded under a tensile load. The ROI is discretised into a first order 150 x 150 pixels element mesh. The standard settings for the p-DIC algorithm are adopted and can be found in Table 4.2. Summarised, a local 5% strain convergence is requested.

Figure 4.9 indicates the order distribution and error indication for the numerical experiments. Elements located at the heterogeneous deformations received, as can be expected, higher order shape functions. Furthermore it is seen that elements at strain concentrations contain a higher error indication. Figure 4.10 shows that the rather large mesh is refined properly and represents the imposed deformations well. It is noted that this is the same experiment as used in the validation of the error estimation approach. The mesh obtained using standard convergence is the same as the one obtained using an error boundary of 0.02 pixels.

Because the automated refinement performed well in a numerical case, three real experiments are conducted to check the refinement procedure.

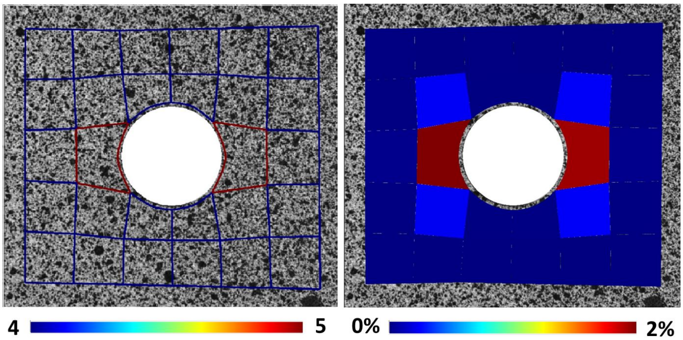

Figure 4.9: Convergence results application 1: a holed specimen loaded under a tensile load (numerical experiment). Left: Element order, right: element error.

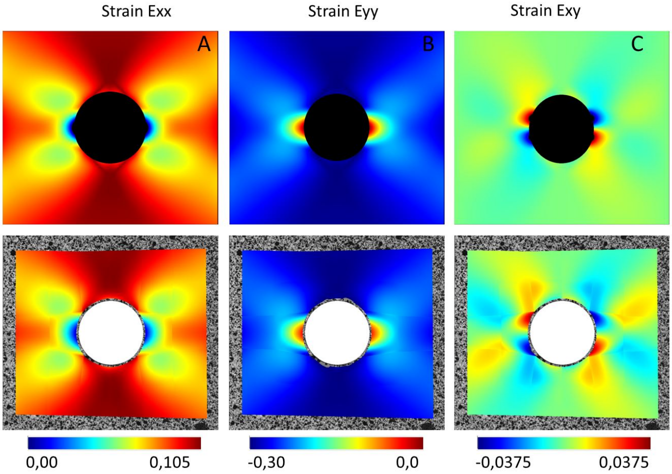

Figure 4.10: Imposed (top) and measured results (bottom) for application 1: a holed specimen loaded under a vertical tensile load (numerical experiment).

4.6.2 Application 2: Tensile test

The same test as the numerical case is done experimentally. A 50 mm wide specimen is perforated in the center with a 15mm hole. The specimen is loaded with a tensile load in the horizontal direction. A totally different mesh size is used, originally a 100x100 pixel first order mesh, to show the independence of the results towards the element size. As stated in section 4.4, an experienced user can modify the criterion to improve performance. The convergence curves indicated that convergence below 5% was possible. Therefore, the local strain criterion was further lowered to 2.5%.

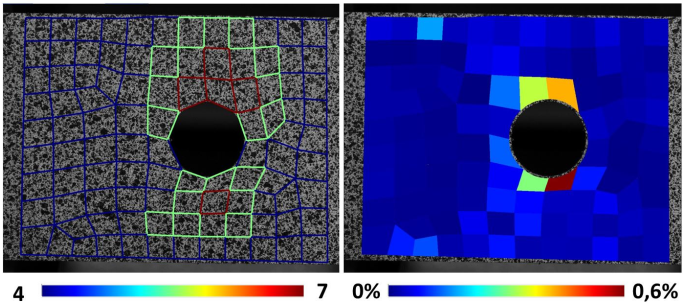

Figure 4.11: Convergence results application 2: a holed specimen loaded under a horizontal tensile load. Left: Element order, right: element error.

The results from the experimental tensile test confirm the results obtained in the numerical case. Again the elements are refined properly, as the measured field matches with the simulated deformation field (Fig. 4.11 and 4.12). The error indication again indicates the elements at the strain heterogeneities.

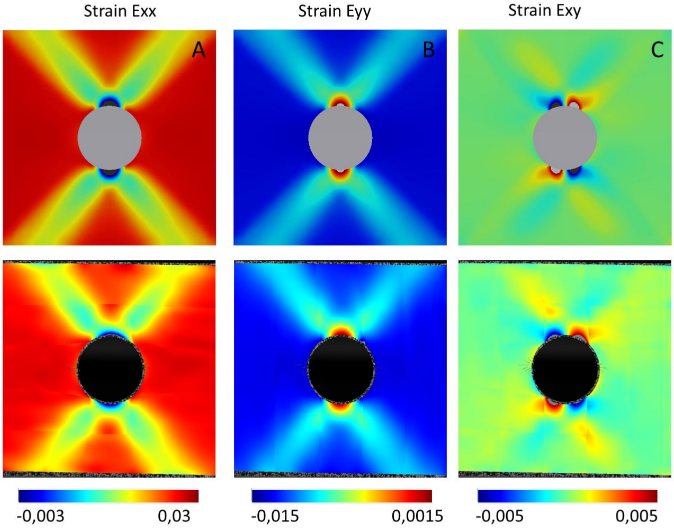

Figure 4.12: Simulation (top) and measured results (bottom) for application 2: a holed specimen loaded under a horizontal tensile load.

4.6.3 Application 3: Shear test

Third, a shear test is conducted to investigate the performance of the procedure against high and concentrated strain peaks (strains above 15%). The experiment is conducted on a specimen developed for generating high shear strains. For the element size, a mesh decently fitting the specimen geometry is chosen. Due to the very concentrated strains, no convergence for the local strain energy was found. As increasing the convergence boundary did not resolve in a converged mesh, following Table 4.1, only local displacement convergence is requested.

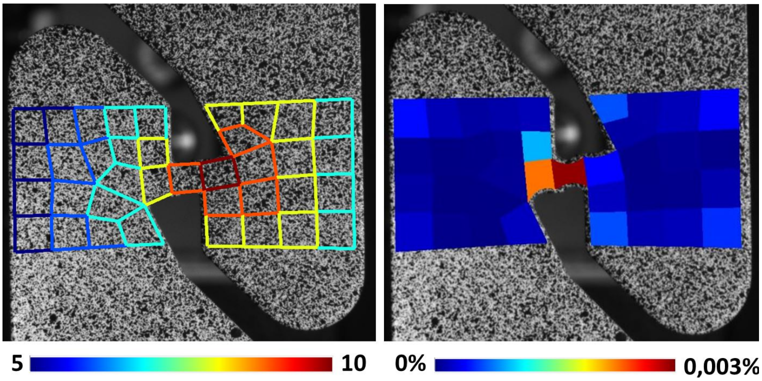

Figure 4.13: Convergence results application 3: vertical shear test. Left: Element order, right: element error.

Figure 4.13 again indicates the order distribution for the shear test. The elements representing the strain concentration received higher order shape functions. Consistent to the previous tests, elements representing strain concentrations indicate a higher error indication. It is noted that the error indication is not directly related to the element order, but is based on the error estimation of the original p-DIC method. For example, the element in the center of the mesh (located at the strain concentration) did not receive the highest order. In the error indication though, it received the highest error indication which can be expected due to the high strain concentration. When, using Fig. 4.14, the results are compared to the simulation, again a similar deformation field is obtained.

4.6.4 Application 4: Disc in compression

Finally, an aluminium disc specimen (radius 40mm, thickness 6mm) is loaded with a compressive force of 9000N. In a compressed disc, strains stay well below

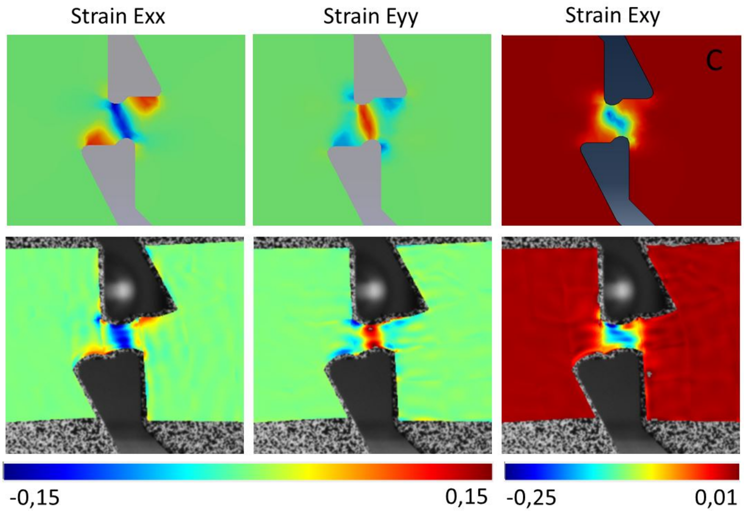

Figure 4.14: Simulation (top) and measured results (bottom) for application 3: vertical shear test.

1%, and thus taking previous tests in account a wide range of experimental situations is covered. Due to the very small strains, no convergence for the local strain energy was achieved. Following Table 4.1, only local displacement convergence is applied. Again, a first order mesh was introduced as initial mesh. The results obtained in this test (Fig. 4.15 and 4.16) confirm the conclusions made in the previous experiments.

4.7 Conclusion

The finite element mesh used in global DIC is crucial to obtain acceptable results. As the optimal mesh is mostly based on pre-knowledge of the expected results, correlation results become very user dependent. To prevent the difficulty just presented, a self adaptive global approach was developed. The proposed method used an absolute error boundary for controlling the refinement procedure. As this absolute value is difficult to obtain, a major improvement to the refinement procedure is presented. The principle of convergence in "strain energy" is introduced in the global DIC approach. The concept of using convergence in displacement and strain norms, originating from the adaptive finite element analysis, is implemented and validated using a global DIC algorithm capable of coping with a non uniform higher order mesh. Hereby, an automatic adaptive

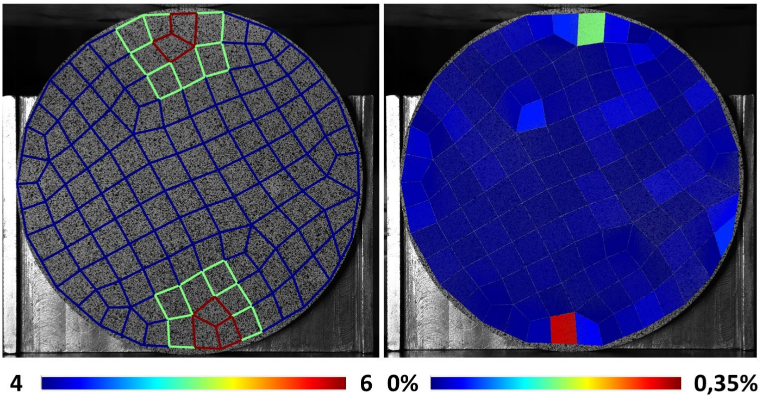

Figure 4.15: Convergence results application 4: Disc in compression. Left: Element order, right: element error.

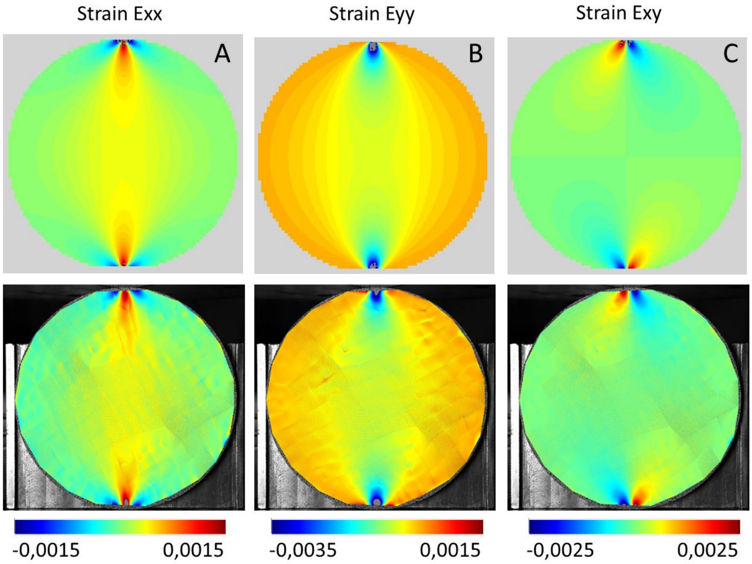

Figure 4.16: Simulation (top) and measured results (bottom) for application 4: Disc in compression.

global DIC procedure is achieved where, in contrast the the original absolute error bound, a more intuitive relative error is supplied to the adaptive algorithm. The proposed concept has proven to be valid on an illustrating example introducing different spatial resolutions as a function of the x-coordinate. The automatic, convergence driven global DIC algorithm was capable of determining appropriate element orders without any pre-knowledge of the deformation field. Furthermore, it has been shown that even the element size does not influence the final results, but only influences the polynomial order of the elements. As second part in the validation, the robustness to experimental influences is investigated. The validation showed that the refinement procedure is able to cope with varying noise and light conditions as well as with different correlation criteria. After the validation, three specifically chosen experiments are performed. First of all, a standard tensile test on a perforated specimen is performed. Here plastic strains occur, indicating that the method can work beyond elastic cases. Secondly, a shear test is performed to achieve very concentrated strain peaks embedded in a homogeneous deformation. Finally, and in contrast to previous specimens, a disc in compression is used to obtain very small strains. The applications also implied the different steps a user can undertake in the correlation. Ranging from accepting the correlation, to reducing the convergence boundary to even discard criteria to boost the algorithm. It is stressed that altering the convergence criteria is only boosting the refinement procedure and is not necessary for a standard correlation. Further the original error estimator provides an error indicator to assess the quality of refinement.

Chapter 5

Strain Continuity

Chapter 3 indicated that using a global description, introducing C^0-continuity, improves the methods performance. Therefore, in this chapter, it is investigated whether introducing C^1-continuity can further improve the methods performance. Chapter 5 firstly introduces a novel C^1-continuous algorithm and then compares it towards current C^{-1}- and C^0-continuous methods.

Wittevrongel L., Lava P., Lomov S.V. and Debruyne D. C^n continuity in Digital Image Correlation: Implementation and validation of C^{-1}, C^0 and C^1 algorithms. *Strain,*Published online DOI: 10.1111/str.12146, 2015
Some parts of the original publication are left out to avoid redundancy.

5.1 Abstract

In digital image correlation, a global approach is more and more used aside from the traditional subset method. The biggest advantages of the global approach are the continuity of the displacement field and the clear link to finite element analysis. In this paper the traditional subset method is compared to several implementations of the global method, to investigate the importance of continuity in DIC. As first the most known Q4-DIC is implemented, where linear elements describe the deformation. The second implementation is the so called p-DIC where the element mesh used in the correlation can be updated to higher order elements to describe more complex deformations. The third implementation is a newly proposed C^1 continuous global algorithm. This

algorithm is similar to the other global approaches, but uses a triangular finite element mesh where the triangular elements within the mesh have a generic p^{th} order description. Accordingly, elements can vary both in size as well as element order to describe more complex deformations while preserving C^1-continuity. The four implementations are made in the same platform, leading to a more robust comparison. In the comparison, both numerical as experimental tests are conducted and the relation between resolution and spatial resolution is investigated for all approaches. It is concluded that continuity itself does not have a major influence on the performance of the methods. The choice of algorithm will be based on the desired specifications of the measurement.

5.2 Introduction

Digital Image Correlation (DIC), is a technique used to measure surface deformation by tracking image features. As the complete surface is measured, this method is referred to as a full field measurement method. The full field deformation has many applications in experimental mechanics. The full field deformation can be used to validate finite element simulations or to characterise materials [74]. Some well known approaches for characterising materials using DIC are VFM [56] and FEMU [55]. To obtain the deformation field, two main approaches for DIC are currently available, namely local and global DIC. Local DIC, also known as subset DIC, is based on tracking each pixel and its local neighbourhood from the reference image to the deformed image [1]. An alternative approach is global DIC where all the pixels are connected to each other and tracked simultaneously from reference image to the deformed image. Originally, the global approach uses a mesh with a fixed element type and is introduced by Besnard et al. using Q4 elements [22]. More recently, an adaptive approach has been developed [80]. In this approach the elements can change in polynomial order during the correlation in view of their underlying deformation field. Using this adaptivity, elements can automatically adapt to represent more complex deformations. Although this increases computation time, previous work indicated that this adaptive global DIC approach, p-DIC, is an alternative method for quantifying high strain gradients at low strain levels where the trade-off between spatial resolution and noise floor reduction becomes more crucial. By using the Q4 or p-elements in a global DIC description C^0-continuity is introduced, resulting in a smooth displacement field. In the global approach the strains can, in contrast to the local method, be calculated directly from the displacement field, without the need of polynomial smoothing. In this way, with the proposed elements, strains are continuous within elements but non-continuous across element boundaries [60]. For the local method the displacement field is non continuous and thus a local polynomial smoothing approach is used to obtain the strains [19][18]. In most applications a continuous deformation field is predicted, and thus traditionally results are evaluated by the "smoothness" of both displacement and strain results. In this way, intuitively a C^1-continuous displacement field can be considered as a nice improvement to DIC implementations. Several C^1-continuous global DIC algorithms were presented in the past. Cheng et al. [21], used B-Spline functions to obtain displacement fields with continuous derivatives. More recently, Langeroc et al. [27] used iso-parametric elements with 24 degrees of freedom (DOF) to ensure a continuous deformation field. Further, global DIC approaches that use global continuous functions, such as global polynomials, making them $C^{infinite}$-continuous are also developed [82]. In this article however, the focus is on FE-based global DIC approaches. In this way, all methods proposed will use the exact same mathematics and minimisation routines, except for the shape functions. In this way, the actual influence of different elements can be profoundly investigated. Further, by using only FE based DIC algorithms, the proposed methods are very easy to implement as they are very similar to the widely known FE-DIC approach. Therefore, as third implementation, a novel adaptable higher order C^1-continuous FE-based global DIC approach is used as third implementation of the global approach. The choice for a higher order approach is made because previous work [80] showed that a p-refinement scheme, where elements receive higher orders, can be a valuable upgrade to the FE-DIC approach. In this way, in contrast to most methods, both h- and p-refinement are usable. H-refinement means that the element size is reduced to describe more complex deformation fields. The reduction of element size however, is not always beneficial to DIC as the amount of information (speckles) reduces leading to poor or even loss of measurements [1].

In this article, the aim is to investigate the influence of continuity by using various implementations of DIC. First of all the traditional (local) subset method is used. Next, several implementations of the FE based global method are used. These algorithms are Q4-DIC, p-DIC and the newly proposed C^1 algorithm. The algorithms are assessed using both numerical as experimental tests and by using the displacement, strain and spatial resolution. The outline of the article is as follows. Section 5.3 presents a short view on the traditional local DIC method. In section 5.4 the widely known Q4-DIC is explained, while section 5.5 introduces the self adaptive hierarchical global approach. In section 5.6, the continuous global approach is presented and section 5.8 includes the validation of the approaches.

5.3 Subset method: C^{-1} DIC Algorithm

Omitted, See Section 2.1.1

5.4 Q4-DIC: C^0-Q4 DIC Algorithm

Omitted, See Section 2.1.2

5.5 p-DIC: C^0-p DIC Algorithm

Omitted, See Section 3.4

5.6 C^1 DIC Algorithm

For the most used shape functions in global DIC, a C^0 continuous displacement field is obtained. Within these elements the strains are continuous, but across element boundaries this continuity is lost. The final global implementation used in this work, will be an approach containing a continuous deformation field. To implement the C^1-continuity, again the same mathematical framework as in section 5.5 is used but an alternative set of shape functions Φ_i are implemented. In this section, such a set of functions is introduced. More than introducing a fixed set of C^1-continuous functions, a set of generic p^{th} order functions is introduced. A p^{th} order set is developed since it was illustrated in [80] that the use of larger higher order elements in a global DIC approach has a positive influence on the correlation procedure.

5.6.1 Element geometry

As a starting base, Argyris elements are used to obtain C^1-continuous shape functions [83]. The Argyris element, shown in Fig. 5.1, contains 21 DOF representing a 5^{th} order element. The starting order is 5, since no C^1 functions exist for $p < 5$ [84].

It has so-called "Argyris DOF" $(1-3)$ at the vertices and "Hermite DOF" $(4-6)$ at the center of the edges. The Argyris point uses d, $\frac{\delta d}{\delta x}$, $\frac{\delta d}{\delta y}$, $\frac{\delta^2 d}{\delta^2 x}$, $\frac{\delta^2 d}{\delta^2 y}$ and $\frac{\delta^2 d}{\delta x \delta y}$ as degrees of freedom. The Hermite point only uses $\frac{\delta d}{\delta n}$ as degree of freedom,

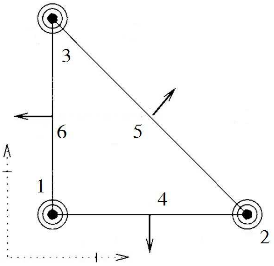

Figure 5.1: The Argyris element, containing 21 DOF.

where n is the normal direction on the considered edge. It is shown that using the standard DOF (Fig. 5.1) the solution is both unisolvent and containing continuous differentiation across boundaries. To obtain higher order elements, more DOF have to be introduced to the element in order to represent a higher polynomial order. It is shown that in the general case one needs $p-5$ Lagrange DOF (only using d as DOF) and $p-4$ Hermite DOF per edge in order to remain unisolvent and continuous [83]. The amount of Lagrange, Hermite and Argyris points are indicated by N_L, N_H and N_A.

- Lagrange points $N_L = 3*(p-5)$, containing 1 DOF.
- Hermite points $N_H = 3*(p-4)$, containing 1 DOF.
- Argyris points $N_A = 3$, containing 6 DOF.

In total, $6p-9$ DOF are present in a p^{th} order element. As stated by Zienckiwicz [3], the number of degrees of freedom needed to describe a p^{th} order polynomial, referring to Fig. 5.2, writes:

$$N_p = \frac{(p+1)(p+2)}{2} \tag{5.1}$$

As $N_p \geq 6p-9$, the element is completed with internal Lagrange points to describe a full p^{th} order polynomial so that $N_p = N_L + N_H + N_A + N_{L_{internal}}$.

$$N_{L_{internal}} = \frac{(p+1)(p+2)}{2} - 6p + 9 = \frac{p^2 - 9p + 20}{2} \tag{5.2}$$

Using the above, the sixth and seventh order elements are shown in Fig 5.3.

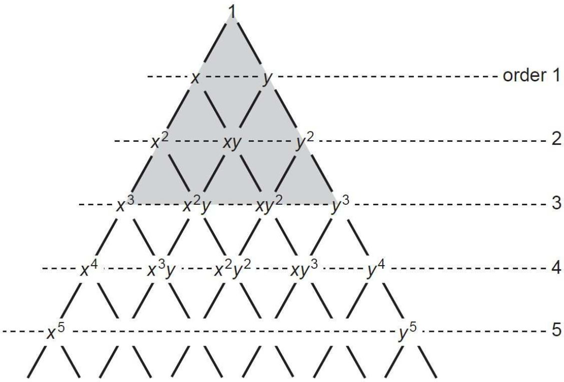

Figure 5.2: Pascals Triangle. Cubic expansion indicated in gray. [3]

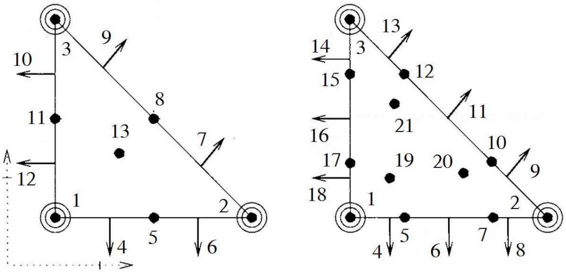

Figure 5.3: The sixth and seventh order elements used in the C^1 approach.

5.6.2 Shape functions

The value ψ (representing horizontal or vertical displacement), defined by a p^{th} order description, can be written as:

$$\begin{aligned} \psi(x,y) &= \textstyle\sum_{n=1}^{N_p} a_n x^{k_n} y^{l_n} \\ &= \textstyle\sum_{n=1}^{N_p} a_n g_n \end{aligned} \tag{5.3}$$

where k_n and l_n represent the powers for x and y based on Pascals Triangle shown in Fig 5.2 and a_n represents the sought polynomial coefficients. Function g_n is part of the basis $\beta = \{g_1, g_2, g_3, \cdots, g_{N_p}\}$, defined by the polynomial order p of the element. Matrix $[\psi]$ is defined as the matrix containing the degrees of freedom for all nodes. The degrees of freedom for each node are dependent on its type:

- Lagrange functions: $\psi(x_\eta, y_\eta)$
- Hermite functions: $\psi_n(x_\eta, y_\eta)$
- Argyris functions: $\psi(x_\eta, y_\eta)$, $\psi_x(x_\eta, y_\eta)$, $\psi_y(x_\eta, y_\eta)$, $\psi_{xx}(x_\eta, y_\eta)$, $\psi_{yy}(x_\eta, y_\eta)$ and $\psi_{xy}(x_\eta, y_\eta)$

where (x_η, y_η) is the coordinate of the considered node. Using matrix $[\psi]$, the following relationship can be established:

$$[\psi] = [L][a] \tag{5.4}$$

where matrix $[a]$ represents the polynomial coefficients from Eq. 5.3 and $[L]$ represents the generalised Vandermonde matrix $L = \{L_i(g_j)\}_{i,j=1}^{N_p}$ using the basis β. In matrix L L_i depends on DOF number i, where $i \in \{1 \cdots N_p\}$, linked to the type of each node. E.g. for the sixth order element shown in Fig. 5.3 $i = 1$, refers to the first DOF of Argyris point $\eta = 1$. $i = 7$ refers to the DOF of Hermite point $\eta = 4$ and $i = 10$ refers to the first DOF of Argyris point $\eta = 2$. Finally, $i = 28$ refers to the first DOF of the Lagrange point $\eta = 13$. For the different points, L_i writes:

- Argyris:

$$L_a(g) = g(x_\eta, y_\eta) \tag{5.5a}$$

$$L_b(g) = \frac{\delta g}{\delta x}(x_\eta, y_\eta) \tag{5.5b}$$

$$L_c(g) = \frac{\delta g}{\delta y}(x_\eta, y_\eta) \tag{5.5c}$$

$$L_d(g) = \frac{\delta g}{\delta x \delta x}(x_\eta, y_\eta) \tag{5.5d}$$

$$L_e(g) = \frac{\delta g}{\delta y \delta y}(x_\eta, y_\eta) \tag{5.5e}$$

$$L_f(g) = \frac{\delta g}{\delta x \delta y}(x_\eta, y_\eta) \tag{5.5f}$$

- Lagrange:

$$L_a(g) = g(x_\eta, y_\eta) \tag{5.6}$$

- Hermite:

$$L_a(g) = \frac{\delta g}{\delta n}(x_\eta, y_\eta) \tag{5.7}$$

where (x_η, y_η) is the coordinate and the sub-indices a till f represent the local DOF of the considered node η. Using the basic condition of set of shape functions,

$$\phi_i(x_j, y_j) = \begin{cases} 1 & \text{if } j = i \\ 0 & \text{if } j \neq i. \end{cases} \tag{5.8}$$

$[\psi^i]$ can be defined as:

$$[\psi^i] = \begin{cases} [\psi^i]_j = 1 & \text{if } j = i \\ [\psi^i]_j = 0 & \text{if } j \neq i. \end{cases} \tag{5.9}$$

Using Eq. 5.4, we can define:

$$[a^i] = [L]^{-1}[\Psi^i] \tag{5.10}$$

where $[a^i]$ represent the coefficients of the shape function i by using basis $[g]$, obeying Eq. 5.8. The general description for shape function $\phi_i(x, y)$, then becomes

$$\begin{aligned} \phi_i(x, y) &= [a^i][g] \\ &= [L]^{-1}[\psi^i][g] \end{aligned} \tag{5.11}$$

where

$$\begin{aligned} [g] &= [g_1, g_2, \cdots, g_{N_P}] \\ &= [x^{k_0}y^{l_0} \cdots x^{k_i}y^{l_i} \cdots x^{k_{N_P}}y^{l_{N_P}}] \end{aligned} \tag{5.12}$$

As an example, shape functions for an element with order $p = 6$ (Fig. 5.3) are shown in Appendix D. The shape functions derived above can be used in the global DIC scheme presented in Section 5.5. Due to the presence of extra nodes for higher order elements, neighbouring elements need to be of the same polynomial order. Because of this, in contrast to the p-DIC method, only uniform order meshes can be obtained. The order is not limited in degree, but is limited to a uniform order. We do note that, as mentioned in the introduction, different C^1-continuous approaches exist. This new method was introduced to be easily implementable. It uses the exact same mathematics as the Q4-DIC, except for the shape functions. These shape functions can easily be calculated using Eq. 5.11.

5.6.3 Applications

Aside from the smooth strain field obtained for deformation measurements, the C^1-continuous elements also have some applications where the C^0 elements are not sufficient. This is the case for plate bending applications where the conformity requirements obliges inter-element continuity for both the

Method	$\mathbf{C^{-1}}$	$\mathbf{C^0}$-Q4	$\mathbf{C^0}$-p	$\mathbf{C^1}$
Module	MatchID 2D	AdaptID		
Principle	Local	Global		
Element	Square	Lin quad	Curved quad	Triangle
Order	$0 \xrightarrow{1} 2$	1	$1 \xrightarrow{1} p$	$5 \xrightarrow{1} p$
Continuity	N/A	C^0	C^0	C^1
Adaptivity	N/A	Size	Size/order	Size/order

Table 5.1: Overview of the implemented DIC algorithms with varying continuity.

displacement and slope on the boundary of elements [85]. Further, because the second order derivative can easily be obtained, it can also be used in applications where higher order differentials are required such as Magnetohydrodynamics (MHD) applications [86]. The use of second order derivations in local DIC has been discussed in [17].

5.7 Overview

In sections 5.3, 5.4, 5.5 and 5.6 four alternative DIC approaches are presented. These are the traditional subset method, the global Q4-DIC (C^0-Q4), the recent p-DIC (C^0-p) and the newly presented C^1 method. In Table 5.1 the main properties of each method are compared.

All algorithms are implemented in the platform "MatchID" [9]. The local approach is housed in the "MatchID 2D" module while the three global approaches are housed in the "AdaptID" module. By implementing all 4 approaches in the same platform they all use the same libraries for interpolation and mathematical operations, leading to a more profound comparison. The influence of filters, interpolation and matrix calculations are ruled out in this way.

For all methods, strains are calculated exactly the same. A logarithmic Euler Almansi tensor is used, defined as:

$$E = \frac{1}{2}(F^T F - I) \tag{5.13}$$

where the deformation gradient F is calculated analytically from the shape functions used within the subset or elements. Usually, the deformation gradient for the local method is not obtained using direct derivation, but local polynomial smoothing over several measurement points is used for the determination of the deformation field. When smoothing of a non-continuous displacement field is performed, a more accurate deformation field can be obtained. The amount of smoothing however is a cumbersome task, as the increase of the smoothing will decrease the resolution but in the meanwhile increase the spatial resolution. In the first stage, the methods are compared by calculating the deformation gradient without smoothing of the displacement field. In the second stage the relationship between the resolution and spatial resolution is established for all four methods to obtain a more profound comparison. While the strain calculation remains the same for the global methods, the strain calculation for the local method is done by using the classical strain window approach.

5.8 Validation

5.8.1 Numerical and practical experiments

Firstly, two numerical tests will be conducted. The numerical tests are used to validate whether the methods perform as could be expected. First of all, a simple quadratic (horizontal) displacement field is imposed. The quadratic displacement field results in a linear deformation field. Secondly, a tensile test on a perforated specimen is simulated. In a third stage, the simulated tensile test will be performed experimentally. In this way, the same test is used to validate the procedures in both numerical as real circumstances.

Quadratic displacement

The first numerical test is a simulated quadratic displacement field. This field is chosen as it will introduce a linear strain field, which can be easily compared to its theoretical deformation field. The imposed field is described by Eq. 5.14 and can be found in Fig 5.4.

$$\Phi_D(x) = \begin{cases} d_x = 0.01x + 0.0001x^2 \\ d_y = 0 \end{cases} \tag{5.14}$$

Fig 5.5 indicates the deformation field obtained by the four methods, presented on the same color scale.

Fig 5.4 indicates a zoom region. After correlating the numerical images, the results from this region are extracted. The region is defined as a line at y =

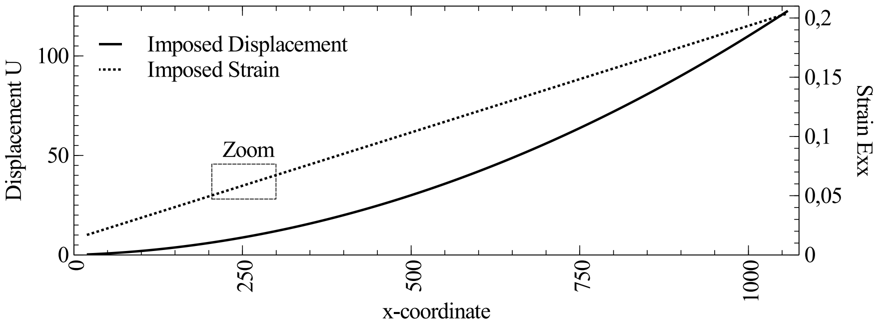

Figure 5.4: Imposed strain and displacement field for the quadratic deformation, line extraction at y = 100 (middle).

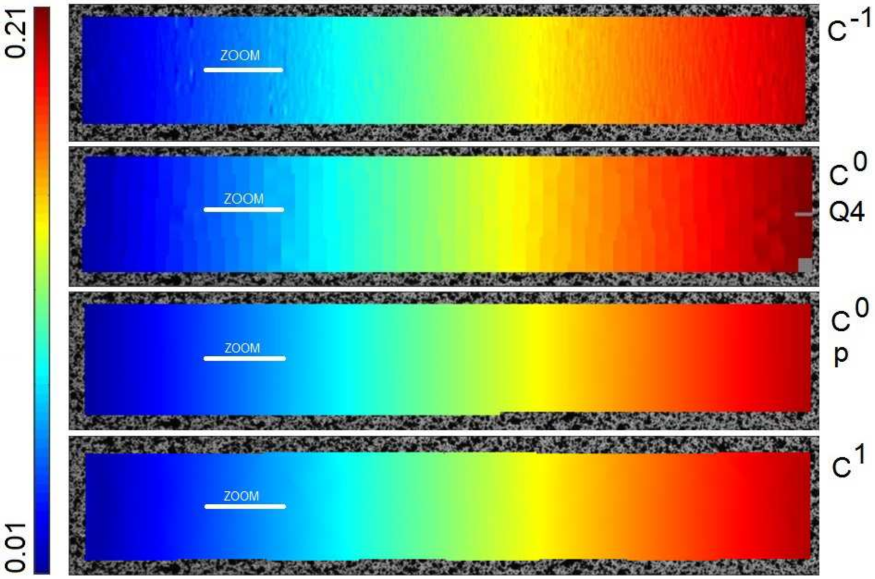

Figure 5.5: Measured Exx strain field for the numerical quadratic displacement, obtained by using the four proposed correlation algorithms.

100 pixels (middle of the image) with x ranging from 200 to 300 pixels. The results for the Subset method, the global C^0 approaches and the C^1 approach are presented in Fig 5.6.

Fig 5.6 clearly indicates the nature of all four algorithms. The subset method

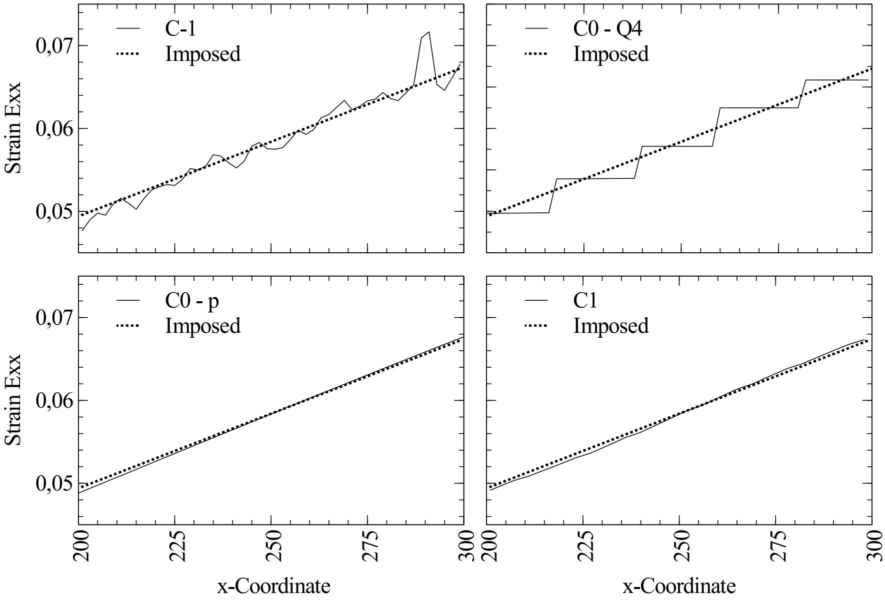

Figure 5.6: Line extract from the measured Exx strain field for the numerical quadratic displacement at position x = 200 .. 300 and y = 100.

has a very noisy strain derivation as it has no continuity whatsoever. Because of this, a random error is observed. The C^0 DIC however, has a more systematic error as displacement continuity was introduced. That strains are continuous within the element and non continuous across element boundaries can be clearly seen in Fig 5.6. In this way one can see the element size of 25 pixels, the same size of the subsets. In the p-DIC algorithm, the mesh was automatically updated to a second order mesh to represent the deformation. Therefore, the strain jumps are barely seen. It was made sure that an element boundary for all methods was included in the middle of the zoom area. In this way, it is seen that jumps are hard to see, although they are still there. This will be more clear in the practical example. The continuity of the C^1 algorithm is obvious. No jumps in the strain field can be observed, showing the continuity of the field.

Perforated tensile specimen

The second numerical benchmark is a tensile test on a perforated specimen. This test will be done experimentally in the next paragraph. The results of this test are shown in the Figures 5.7 until C.1.

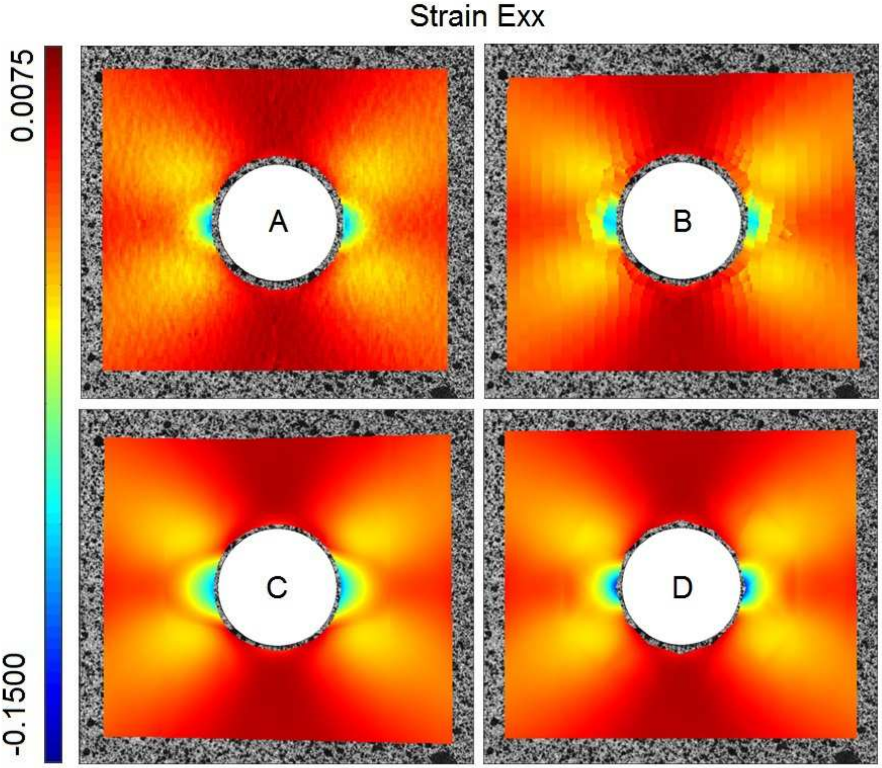

Figure 5.7: Measured Exx strain field for the numerical simulated tensile test on a perforated specimen, obtained by using the four proposed correlation algorithms. A) $C{-}1$, B) $C^0 - Q4$, C) $C^0 - p$ and D) C^1.

The results from this test will be analysed using a horizontal line cut at pixel hight 250 pixels. The deformation field that was imposed at this line cut is shown in Fig 5.8 while the correlated results for this line cut for each method are given in Fig C.1. The total error of each method, compared to the imposed deformation field, is given in Table 5.2.

Again, the differences between the algorithms are clear. The C^1 algorithm is the only one producing a smooth strain field. The C^0-p algorithm is, thanks to the adaptable elements, capable of representing the heterogeneous deformation field. The C^0-Q4 method has again the linear approximation of the deformation within the elements and the subset method again the noisy strain field. We do note that the overall performance of all four methods are competitive, as

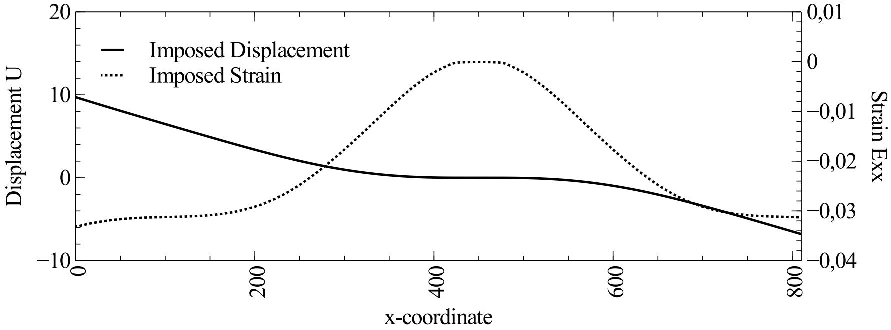

Figure 5.8: Imposed displacement and strain for the numerical simulated tensile test on a perforated specimen at y = 250.

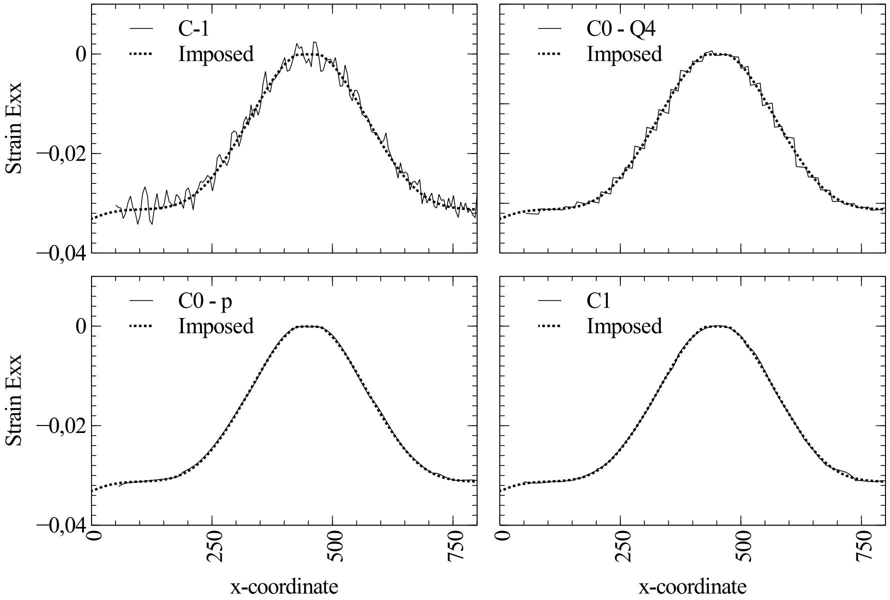

Figure 5.9: Line extract from the measured Exx strain field for the numerical simulated tensile test on a perforated specimen at y = 250.

they all have an average error of $1 \cdot 10^{-4}$ (See Table 5.2). The deviation on the strains however is different due to the natural differences of the algorithms.

	μ	σ	DOF
$\mathbf{C^{-1}}$	$9.5364 \cdot 10^{-5}$	$2.3986 \cdot 10^{-3}$	NA
$\mathbf{C^{0}}$-Q4	$8.4984 \cdot 10^{-5}$	$2.3526 \cdot 10^{-3}$	1682
$\mathbf{C^{0}}$-p	$8.6244 \cdot 10^{-5}$	$1.4661 \cdot 10^{-3}$	584
$\mathbf{C^{1}}$	$9.6164 \cdot 10^{-5}$	$1.4628 \cdot 10^{-3}$	992

Table 5.2: Mean and standard deviation of the error in measured Exx strain field for the numerical simulated tensile test on a perforated specimen together with the used DOF.

Practical Experiment

From the numerical experiments, it has been shown that all four algorithms are capable of accurately representing a deformation field. Both a quadratic displacement field as a heterogeneous deformation field were reconstructed accurately. However, the fundamental difference between the algorithms is presented clearly. The direct derivation of the displacement field obtained by the C^{-1} method, resulted in a noisy strain field. The derivation of the C^0 method, resulted in a continuous strain field inside the elements, but non continuous strains over the element borders. The direct derivation of the C^1 method resulted in a smooth deformation field, with no jumps or discontinuities.

Now, as practical test, a perforated specimen is captured during a tensile loading. This test is similar as the simulated test used above. The images obtained during the test are analysed with all four methods. Again all four results are compared to each other. Do note that now the solution is not known in advance. In this test the results are only compared to each other and not to an analytical solution. The purpose here is to indicate that all methods give approximately the same solution but with different continuities. The used meshes are illustrated in Fig. 5.10

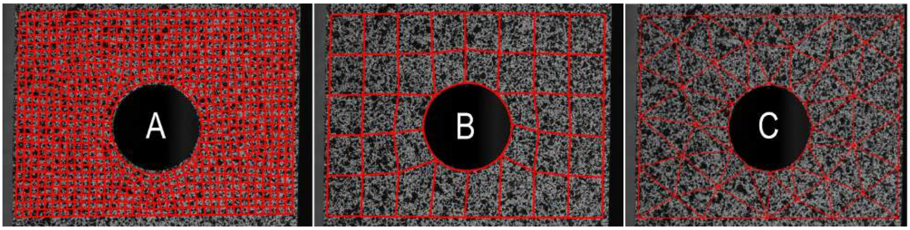

Figure 5.10: FE mesh used in (A) C0-Q4, (B) C0-p and (C) C1.

The obtained deformation fields are shown in Fig. 5.11

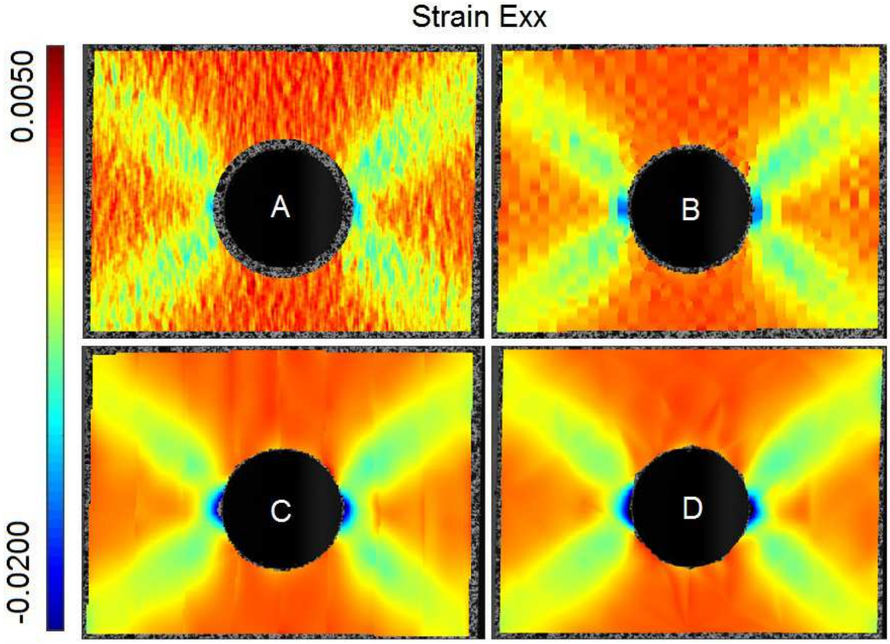

Figure 5.11: Measured Exx strain field for the experimental tensile test on a perforated specimen, obtained by using the four proposed correlation algorithms. A) $C{-}1$, B) $C^0 - Q4$, C) $C^0 - p$ and D) C^1.

Taking a line extract at y = 525, the profiles shown in Fig. 5.12 are obtained.

The experimental test confirms the conclusions made during the numerical validation. All four methods yield approximately the same strain profile but handle the noise differently. The difference is best seen in the continuity of the deformation field. Fig. 5.12 clearly indicates that the C^{-1} method is indeed very noisy but introduces almost no systematic error. For the C^0-Q4 method, the averaged linear strain reduces noise but introduces systematic errors. For the C^0-p method, the higher order strains result in less noise and only minor systematic error. The strain is more smooth for the C^0-p method, but still holds strain jumps on the edges of the elements. For the continuous algorithm no strain jumps can be seen. Big fluctuations are present, but the strain remains continuous. This might be valuable when second order derivatives are needed. Remark that this example was presented to indicate fundamental differences between methods, they cannot be used to select the best method. In order to compare the methods more profoundly, next section introduces the resolutions of the different methods.

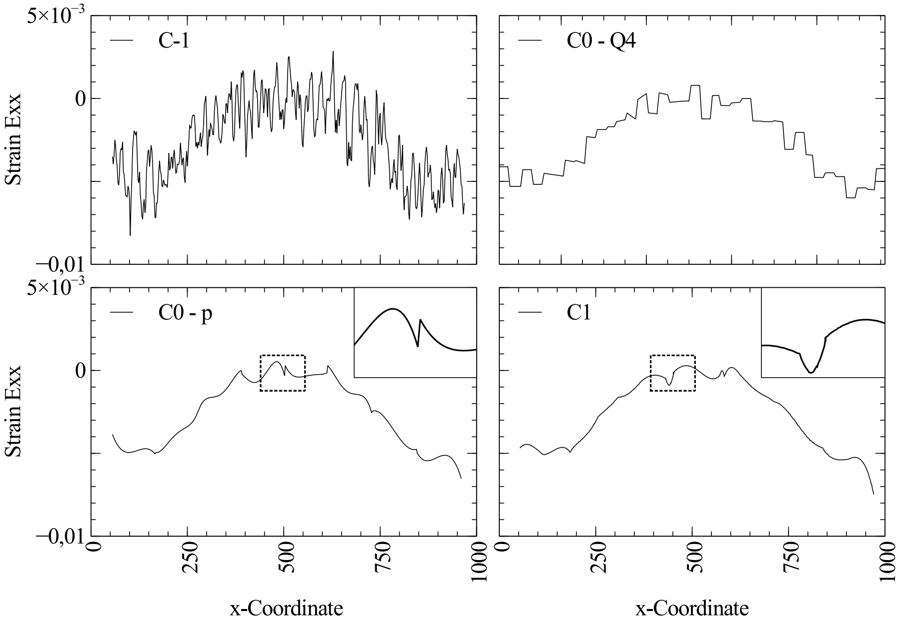

Figure 5.12: Line extract from the measured Exx strain field for the experimental tensile test on a perforated specimen at y = 525.

5.8.2 Resolutions

Previous tests indicated a good performance of all four methods. In the present section a more quantitative comparison of the different implementations is performed. The comparison is done using measurements and spatial resolution. With the introduction of the p-DIC algorithm, an in-depth validation of the local C^{-1} and the C^{0}-p method has been performed. In that validation an objective approach of comparing DIC algorithms has been used. To keep conformity, the same approach is used in this validation. Throughout the comparison, the following definitions are used [80]:

Resolution: The resolution or noise floor, is determined by using a so-called self correlation test. Such a test implies the correlation between two images where no deformation is performed. Due to noise and other influences, a deformation field between both images is measured. For that reason the images used are the original pattern and the same image with an added (numerical) Gaussian noise with a standard deviation of 1%, general obtained for standard 8-bit cameras. The measurand resolution is defined as the global standard deviation σ_g (Eq.

5.15) of the biased measurand field [71].

$$\sigma_g = \sqrt{\frac{n \sum_{x,y} [\Delta u(x,y)]^2 - [\sum_{x,y} \Delta u(x,y)]^2}{n(n-1)}} \tag{5.15}$$

where $\Delta u(x,y)$ represents the biased measurand under investigation.

Spatial resolution: The spatial resolution or detail of the method will be evaluated as the lowest period (i.e. highest frequency) of a sinusoidal deformation that the method is able to reproduce before losing a certain percentage of amplitude. In this way, a 'poor' resolution is a high value and an optimum value is a low one, similar as for the resolution. Thus as deformed image a unidirectional in-plane sinusoidal deformation field is introduced to the original speckle pattern. The generation of the deformed images is done by using the finite element simulation of the experiment intended to be numerically reproduced [30]. The imposed displacement field writes:

$$\Phi_D(\mathbf{x}) = \begin{cases} d_x = a \cdot sin(\frac{2\cdot\pi}{P} \cdot x) \\ d_y = 0 \end{cases} \tag{5.16}$$

where a is the amplitude and P the constant period. As we defined the spatial resolution as the lowest period the method is able to reproduce with a amplitude loss of α, one has

$$Resolution = P \longleftrightarrow \Delta A = \alpha \tag{5.17}$$

where α is the percentage of allowed amplitude loss, which will be the criterion for the spatial resolution determination. Here the loss of amplitude is then defined as:

$$\Delta A = \frac{|a - \mu_a| + 3 \cdot \sigma_a}{a} \cdot 100 \tag{5.18}$$

with

$$\sigma_a = \sqrt{\frac{n_p \sum_{p=0}^{n_p} [A]_p^2 - [\sum_{p=0}^{n_p} [A]_p]^2}{n_p(n_p-1)}} \tag{5.19}$$

$$\mu_a = \frac{\sum_{p=0}^{n_p} [A]_p}{n_p} \tag{5.20}$$

where matrix [A] represents the amplitudes extracted from the reconstructed sine wave R and n_p the count of peaks. The reconstructed sine wave $R(x)$ can be represented as a 1D function, defined as:

$$R(x) = \overline{u}_y(x) = \frac{\sum_y [u(x,y)]}{n_y} \tag{5.21}$$

In this work a fixed amplitude of 5 pixels and a cut off of 5% is used.

To compare the different implementations, the resolutions and corresponding spatial resolutions are plotted in one graph, as the combination of these two quantities indicate the performance of the methods. As can be predicted, both values are inversely related. Achieving a better spatial resolution leads to a degradation of the resolution. By determining the resolution and spatial resolution for different methods and settings, a clear view on the performance of the method can be given. For example, varying the subset size for the local method will alter both the displacement resolution and the spatial resolution. Increasing the subset size will lead to an increase in spatial resolution, but will also lead to a decrease of resolution. In this way, a complete graph of the resolution in function of the spatial resolution can be constructed for each method.

The procedure presented above is applied on all the presented methods. First as measurand the displacement is used. A sinusoidal displacement field is imposed onto the image. The imposed sinusoidal wave has an amplitude $a = 5$ pixels and a period $P = 50 \xrightarrow{25} 200$. Where $A \xrightarrow{\Delta} B$ represents "ranging from A to B in steps of Δ". The cut off is fixed at 5% amplitude loss. The parameters used in the different DIC approaches are shown in Table 5.3.

	C^{-1}	C^0-Q4
Criterion	NSSD	NSSD
Element size (pxl)	$21 \xrightarrow{10} 61$	$100 \xrightarrow{20} 20$
Element order	Quad	linear
	C^0-p	C^1
Criterion	NSSD	NSSD
Element size (pxl)	100 x 100	$200 \xrightarrow{50} 50$
Element order	$4 \xrightarrow{1} 9$	$5 \xrightarrow{1} 8$

Table 5.3: Summarised correlation parameters for all four algorithms, used in the validation of displacement resolutions.

Retrieving the displacement and spatial resolution from the different correlations with varying displacement fields, approaches and settings results in the graph shown in Fig 5.13. The results obtained will be discussed together with the results of the strain validation. The strain resolutions are determined in a similar way.

The algorithmic parameters for the strain validation are given in Table 5.4. The imposed sinusoidal wave has an amplitude $a = 0.05\frac{P}{2\pi}$ pixels and a period

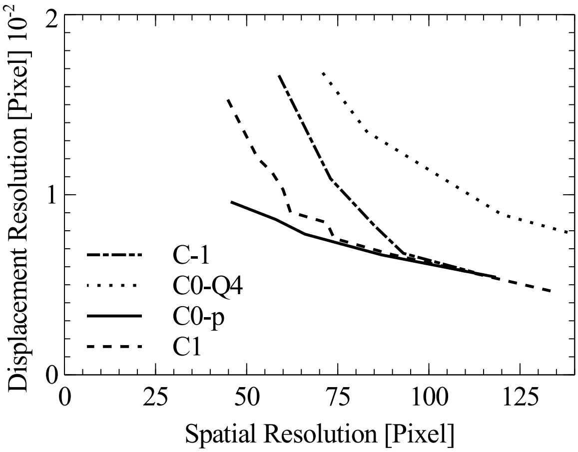

Figure 5.13: Displacement resolution vs spatial resolution for the C^{-1}, C^0-Q4, C^0-p and C^1 obtained by using varying sinusoidal deformation fields.

$P = 40 \xrightarrow{25} 200$. An amplitude $a = 0.05\frac{P}{2\pi}$ results in a strain amplitude of 5%. All the results are given in Fig 5.14.

	C^{-1}	C^0-Q4
Criterion	NSSD	NSSD
Element size (pxl)	$40 \rightarrow 20$	21
Element order	Quad	Linear
Strain window	$11 \xrightarrow{10} 51$	n/a

	C^0-p	C^1
Criterion	NSSD	NSSD
Element size (pxl)	100 x 100	$200 \rightarrow 50$
Element order	$4 \xrightarrow{1} 11$	$5 \xrightarrow{1} 7$
Strain window	n/a	n/a

Table 5.4: Summarised correlation parameters for all four algorithms, used in the validation of strain resolutions.

The results for the validation of displacement and strain resolution versus spatial resolution are presented in Fig 5.13 and 5.14. The data indicates that the C^0-Q4 has the least performance than the others, when the link between noise robustness and spatial resolution is taken into account. It has been shown

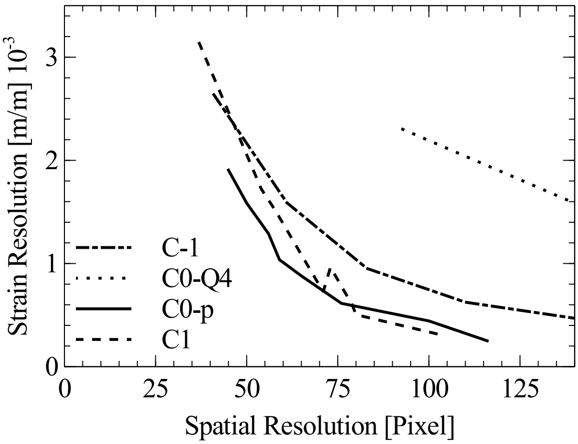

Figure 5.14: Strain resolution vs spatial resolution for the C^{-1}, C^0-Q4, C^0-p and C^1 obtained by using varying sinusoidal deformation fields..

that, when the element size is equal to the subset size, the global method is more robust to noise. This is still valid, but here it is shown that the gain in noise robustness is traded for a significant loss in spatial resolution. The loss is even more clear in the deformation field as only homogeneous (1st order) strain can be represented by linear elements. It is noted that during the applications this difference was not noticed as all applications had a rather large spatial resolution. The spatial resolution for normal applications easily exceeds 300 pixels as no large strain gradients occur. The global approaches C^0-p and C^1 are more robust to noise than the local subset method or the C^0-Q4 method. It is clearly seen that using the higher order elements preserves the gain in noise robustness but has less loss of spatial resolution. This is one of the reasons why C^0-p is applicable for measuring strain gradients at low strain levels. Between C^0-p and C^1 however, the differences are small.

The difference in noise robustness of the methods can be explained by the difference in needed DOF to represent a certain spatial resolution. In Fig 5.15 the DOF of the mesh are given in function of the represented spatial resolution. It is seen that the DOF follow the same trend as the displacement resolution, which is expected as the noise influence should be proportional to the amount of DOF. For the subset method, no global DOF could be given, as the DOF are defined locally. The difference in needed DOF between the $C^0 - Q4$ method and the other global approaches can be explained using [3]. Here it was already shown that a p-refinement scheme in FEA converges faster than h-refinement when the same amount of DOF are used. It was shown that describing a

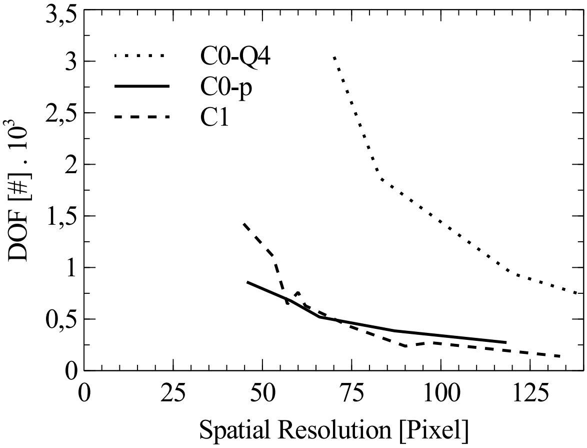

Figure 5.15: Degrees Of Freedom in function of the spatial resolution for the C^{-1}, C^0-Q4, C^0-p and C^1 method.

deformation field using a higher order mesh uses less DOF than when using a first order reduced element size mesh. The same effect is seen when the DOF are checked for the examples given before. Table 5.5 indicates the DOF for each method for each conducted experiment.

	C^0-Q4	C^0-p	C^1
Quadratic deformation	860	410	555
Numerical Deformation	1682	584	992
Experiment	5676	924	1784

Table 5.5: DOF present in the meshes used for the global approaches.

We can observe that the C^0-p method needs the least DOF to represent the data, resulting in the most noise robustness. Second comes the C^1 method. The C^0-Q4 method needs the most DOF, resulting in the least robustness to noise for a certain spatial resolution.

The choice for an algorithm to be used in a certain application will be mostly based on the properties of the measurement. A complex measurement with many discontinuities is best performed using the local method. Is the deformation field unknown, one rather chooses C^0-p as here automatic non uniform refinement is possible and thus both homogeneous and heterogeneous deformation zones will be adapted most efficiently. On the other hand, when explicitly a C^1-continuous field is requested e.g. with beam kinematics [25], the C^1 approach is a valuable alternative towards the other methods.

5.9 Conclusion

In this article the influence of continuity in DIC is investigated. This is done by using 4 different DIC approaches having totally different characteristics. The first approach is the traditional subset method which has no continuity in the displacement field. The second approach is the widely known Q4-DIC. Here a first order finite element mesh, introducing C^0-continuity is used for tracking the deformation. The third approach is a self adaptive higher order global approach, also containing C^0-continuity. The fourth approach is a special developed p^{th} order global C^1-continuous DIC approach named c-DIC. The newly proposed approach is based on global DIC and uses C^1-continuous elements with a generic p^{th} order description. The generic description allows that elements can vary in both size as order while remaining C^1-continuous. It is concluded that the local method (C^{-1}), the higher order method (C^0-p) and the newly proposed C^1 approach are competitive to each other. The C^0-Q4 method performed less as the linear elements constrain the elements deformation flexibility and thus the spatial resolution. The most applicable algorithm for a certain application will be mostly based on the specific requirements of the measurement. A complex measurement with many discontinuities, is best performed using the local method. Is the deformation field unknown, one rather chooses C^0-p as here automatic non uniform refinement is possible and thus both homogeneous and heterogeneous deformation zones will be adapted most efficiently. On the other hand, when explicitly a C^1-continuous field is requested e.g. with beam kinematics, the C^1 approach is a valuable alternative towards the other methods.

Chapter 6

Out of plane motion

Previous chapters introduced the theoretical framework for both a self-adaptive and a C^1-continuous global DIC algorithm in a 2 dimensional set-up. Here a study to reduce the impact of out of plane motion in a 2D setup is presented. The study is aimed on out of plane motion, as it is one of the major error sources in a 2D setup.

Wittevrongel L., Badaloni M., Balcaen R., Lava P. and Debruyne D. Evaluation of methodologies for compensation of out of plane motions in a 2D Digital image correlation set-up. *Strain,* 51(5): 357-369, 2015
Some parts of the original publication are left out to avoid redundancy.

6.1 Abstract

In 2D digital image correlation out of plane motions are an important experimental factor to consider. Because a 2D setup does not provide any depth information, movements towards the camera (out of plane motions, OPM) are disadvantageous for the surface measurement. The effects of out of plane motions in a 2D DIC setup have been investigated profoundly in previous works. The compensation of these motions however is less investigated. Therefore, this paper will handle on solutions for correcting or minimising out of plane motions on 2D DIC measurements. Three compensation methods are implemented and validated. Firstly, a mechanical camera positioning tool is developed to avoid misalignments of the camera and therefore avoid most of the out of plane

motions. Secondly, the camera is aligned numerically using the camera pinhole model and numerically deforming the images. Finally, a method proposed in literature using a region of compensation is used in this validation. All three methods have shown to be able of minimising out of plane motions. Validated in an experimental setup, a great improvement of the identified Poisson ratio is observed during multiple tensile tests.

6.2 Introduction

Digital image correlation (DIC) is an optical technique allowing full field deformation measurements on a specimens surface [1]. Because of its easy set-up and wide range of usability, DIC has become more and more used as a valuable alternative to the grid method, speckle laser, moire and other optical methods [87]. Thanks to the fundamental research performed towards the algorithmic accuracy of DIC, it is becoming more and more accepted as a metrological tool [70]. The acceptance of DIC as a metrological tool, resulted in the use of DIC in material identification procedures such as the virtual fields method or a finite element model updating scheme [74]. The research involving error estimation in DIC made it possible to provide some kind of confidence margins on the performance of DIC [30][18][34]. These studies included the influence of interpolators [29][21], smoothing [19], matching algorithms [14] and others. Although the algorithmic errors are well known and provide an estimate of the error bounds, the influence of experimental parameters on final results is not negligible [73]. The most known experimental influences could be (not limited) light conditions, camera noise, temperature deviations, lens distortions, speckle pattern quality [20][43], ... For 2D and 3D DIC setups the same experimental influences are present. For 2D DIC however, out of plane motions (OPM) are an extra source of uncertainty [4]. Because a 2D setup does not provide any depth information, movements towards the camera (out of plane motions) are disadvantageous for the surface measurement. As a recent study showed, when the DIC measurement is used for material identification using VFM [56], the out of plane motion has a major influence on the final quality of the identification [88]. Because of the importance of out of plane motions in a 2D DIC setup, this paper will handle on solutions for correcting or minimising out of plane motions in 2D DIC measurements. In this work three methods are presented and validated. Two methods for minimising the occurrence of out of plane motions were in house developed. These are methods for aligning the camera to the loading direction of the test and so avoiding out of plane motions due to non perpendicular elongation of the specimen. The third method, a variation on a method initially introduced by Pan [42], does not minimise the effect of out of plane motions but actually corrects them. It uses a second region of interest (ROI) that is assumed to not deform but follows the specimens movements. This extra region will be further denoted as Region of Compensation (ROC). It should be noted that out of plane movements do not only occur due to relative movement of camera and specimen. It has been shown that camera heating results in movement of the camera sensor relative to the camera lens and can also be denoted as out of plane motion [89]. Although camera heating can be denoted as out of plane motions, it will not be considered in this work. Because the effect of camera heating can not be neglected, the cameras were activated before the actual test, to ensure a stabilised camera temperature of 20 degrees Celsius. When the camera obtained a stable temperature, no extra relative motion of the sensor towards the lens occurs.

In this work, the effect of out of plane motions will be validated using the artificial strains produced by the out of plane motion. The quality of the correction method can then be evaluated as the amount of artificial strain remaining in the measurement. In a second stage the correction methods will be used in the identification procedure VFM to assess their performance towards material identification. The paper will be organised as follows. In section 6.3, the effect of out of plane motions on DIC measurements is explained. Section 6.4 introduces the different compensation methods that will be used in this work. In section 6.6, the methods are validated using a rigid body motion test and two tensile tests on two different specimens.

6.3 Influence of OPM

As mentioned in the introduction, deformation measurements of a 2D DIC set up is heavily influenced by out of plane motions. This is straight forward as the one camera used in the set up can not provide any in-depth information, and thus the complete test should remain in plane. Out of plane motions can be introduced by two main factors. The first factor, indicated in Fig 6.1, is pure out of plane motion of the specimen. Here a perpendicular movement of the specimen along the cameras optical axis occurs.

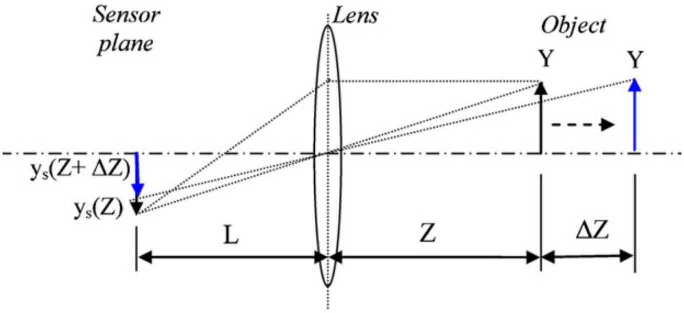

Figure 6.1: Pure out of plane motion. [4]

Because of the movement the specimen will be scaled, resulting in artificial deformations. The artificial deformation can be quantified as [4]:

$$U(\Delta Z) \approx x_s \left(-\frac{\Delta Z}{Z}\right) \tag{6.1a}$$

$$V(\Delta Z) \approx y_s \left(-\frac{\Delta Z}{Z}\right) \tag{6.1b}$$

$$\epsilon_{xx} = \frac{\delta U(\Delta Z)}{\delta x_s} \approx -\frac{\Delta Z}{Z} \tag{6.1c}$$

$$\epsilon_{yy} = \frac{\delta V(\Delta Z)}{\delta y_s} \approx -\frac{\Delta Z}{Z} \tag{6.1d}$$

Where U, V, ϵ_{xx} and ϵ_{yy} are the artificial deformations introduced by the out of plane motion ΔZ, when Z is the distance of the lens to the specimen. (x_s, y_s) represent the sensor positions. The second factor is the rotation of the specimen relative to the sensor plane. The rotation of the specimen will skew the image, resulting in a gradient in the strain field [4].

$$U(\theta) \approx x_s \left(- \frac{y_s sin\theta}{Z} \right) \tag{6.2a}$$

$$V(\theta) \approx y_s \left(cos\theta - 1 - \frac{y_s sin\theta cos\theta}{Z} \right) \tag{6.2b}$$

$$\epsilon_{xx} = \frac{\delta U(\theta)}{\delta x_s} \approx - \frac{y_s sin\theta}{Z} \tag{6.2c}$$

$$\epsilon_{yy} = \frac{\delta V(\theta)}{\delta y_s} \approx cos\theta - 1 - \frac{y_s sin2\theta}{Z} \tag{6.2d}$$

A principle view can be found in Fig 6.2.

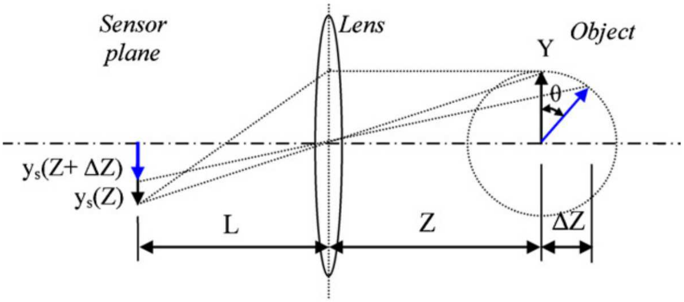

Figure 6.2: Out of plane motion due to rotation.

Where θ is the angle the angle around the x-axis. For the angle γ, the angle around the y-axis, a similar relationship can be obtained. It should be noted that pure out of plane motions result in a constant artificial strain, while for the rotations a strain gradient is observed. The equations above also indicate an inverse relation between the artificial strains and the camera distance Z. In this way a large camera distance will reduce the effect of out of plane motion. Do note that, when the same lens is used, increasing the camera distance will also result in a loss of spatial resolution as the $\frac{mm}{pixel}$ reduces. A fair trade off should be found.

6.4 Compensation OPM

Out of plane motion can be compensated by using different approaches. First of all a bilateral telecentric lens could be used [5]. A bilateral telecentric lens is insensitive to small changes within its telecentric depth in both the object distance and image distance. Second, lens distortion of a well-designed high-quality bilateral telecentric lens is small enough to be neglected. Due to these reasons, it is validated by Pan et al. that a 2D-DIC system using a bilateral telecentric lens can be considered as a 'near perfect and very stable' imaging system. The principle of telecentric lenses is shown in Fig 6.3.

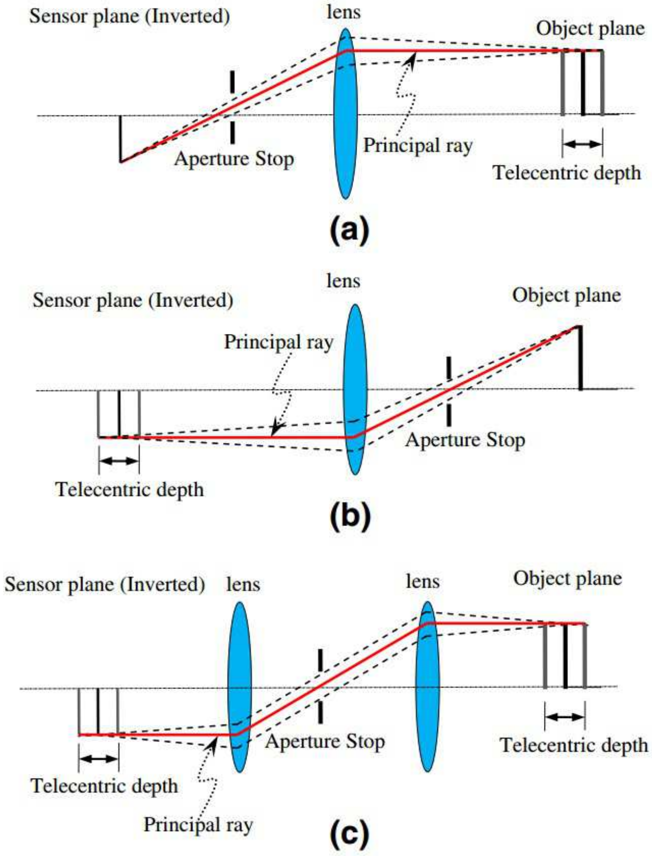

Figure 6.3: Schematic diagram of (a) object-side telecentric lens, (b) imageside telecentric lens, and (c) bilateral telecentric lens [5].

Although the telecentric lens compensates out of plane motions, it has some specific drawbacks:

- A telecentric lens is more expensive than a traditional lens.
- The field of view for a telecentric lens is fixed, in this way each test or specimen requires a specific telecentric lens.

Therefore, it can be an expensive setup when no lens with the required field of view is available. Because we focus on flexible compensation methods, this has not been included in this work. The performance of telecentric lenses has been investigated in [5]. Next, if the assumption is made that no extra out of plane motion occurs during loading, all out of plane motions could be compensated by positioning the camera perpendicular to the specimen. We do note that this is not perfectly met in real experiments and thus not all OPM will be compensated (see Results). The camera alignment can be done physically or numerically by rectifying the image using the camera parameters. Another approach is leaving the camera non-perpendicular but introducing some extra post processing to "rectify" the data. All methods have their specific advantages. The first clear advantage is for the mechanical alignment, as it does not involve any pre or post processing of the data. The camera is positioned physically and not altered during the test so that the specimen or the data (images) obtained for the DIC analysis is not altered. The downside however is that no out of plane motions may occur during the test. The numerical rectification suffers from the same assumption of the mechanical alignment, but has the advantage that it does not require any additional hardware or adjustments to the set up. The downside however is that the initial data is altered prior to the DIC measurements and that the method's performance will be dependent on the calibration quality. Moreover, the change in data will introduce extra errors (e.g. interpolation). Finally, the third compensation method is discussed. Despite the post-processing nature of the compensation, the ROC has its specific advantage. By correcting the measurement data using an undeformed region in the images allows corrections of the out of plane motions occurring during the test. In this way, it can resolve out of plane motions not invoked by non-perpendicularity of the camera. Even more, no pre-knowledge is needed to correct the images. As a downside, it uses the assumption that the ROC does not deform and that it will not influence the behaviour of the specimen itself. The assumption of not influencing the specimen limits the applicability as for example with foils or rubbers an attached ROC will influence the stiffness of the material. Further, it also limits the field of view as the ROC has to be in view the complete test. In this way, very large motions can not be measured as they will be blocked by the ROC. When comparing the rectifying tools to the compensation method, the rectifying tools have the advantage that the influence of perpendicularity is clearly described in the literature and tested numerously. The ROC method however, uses a bicubic fit rather than analytical formulas obtained by physics. In this sense it is a more better fit solution.

In what follows, all three methods are introduced.

6.4.1 Camera Alignment

Although the out of plane motion mostly occurs during a tensile test, it is often invoked by a misalignment of the camera towards the tested specimen. Due to the technological progress it is reasonable to assume an aligned tensile direction. More difficult is the perpendicular positioning of the camera towards the specimen. The position of the camera (see Fig 6.4) can be found by using a single camera calibration procedure. To summarise, following steps are made for determining the camera procedure:

1. 100 calibration images are taken using a standard calibration plate.
2. For the last image, hold the calibration plate against the specimen. In this way the calibration plate will be parallel to the specimen.

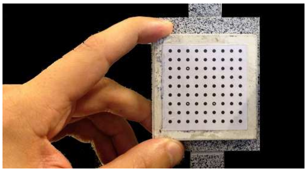

Figure 6.4: The calibration plate parallel to the specimen

3. Run a calibration procedure using the 101 images.
4. From the last image camera positions T_x, T_y, T_z and camera angles θ, ϕ, Ψ can be retrieved by using the calibration software of the DIC package MatchID [9], which allows the users to determine the position and rotation of the camera with respect to the calibration target.

By retrieving the camera parameters using the last image of the sequence, the relative position of the camera to the specimen can be deducted. To determine the accuracy of manual camera positioning, 10 set-ups are made by hand and validated using a single camera calibration procedure. The angles of the specimen towards the camera after manual positioning of the camera are shown in Fig 6.6. The average and deviation on the angles is given in Table 6.1.

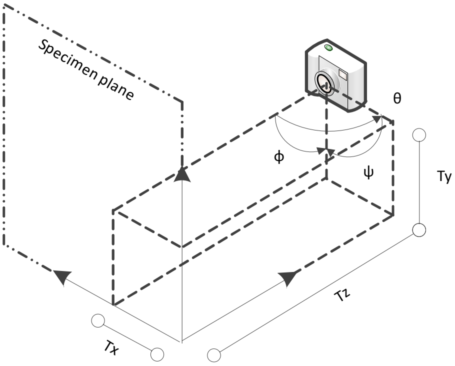

Figure 6.5: Position of the camera relative to the specimens surface.

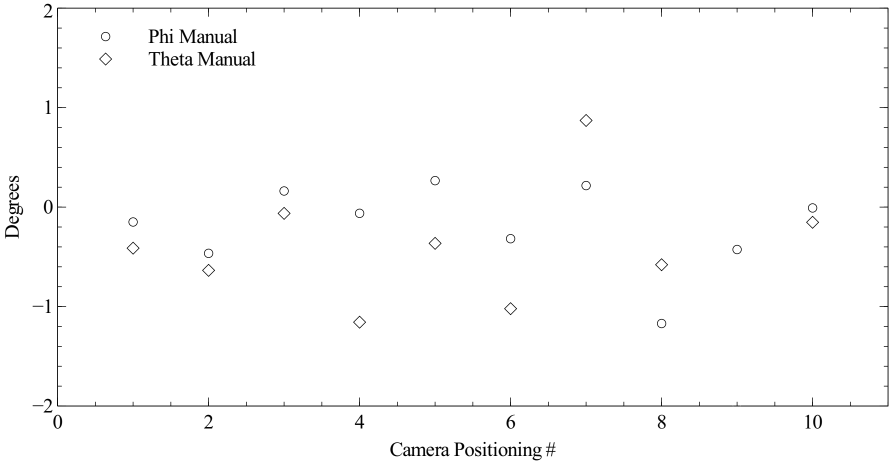

Figure 6.6: Camera positions using manual aligning.

	Average	**Deviation**
θ	1.75	1.23
ϕ	-0.42	2.64

Table 6.1: Camera positions using manual aligning.

Table 6.1 indicates that the manual perpendicular positioning is accurate to ±2 degrees. It is now the purpose to improve this perpendicular alignment using a mechanical tool, capable of rotating the camera perpendicular towards the specimen. As an alternative to the mechanical alignment, also a numerical tool is developed to numerically 'position' the camera perpendicular to the specimen. In a third tool the camera remains misaligned, but the data is post processed using a region called Region Of Compensation.

Physical Alignment.

To achieve a perpendicular camera setup, a high precision rotation stage is designed. Here the camera is mounted onto a platform containing two high precision rotation stages. The assembly can be seen in the Figure 6.7.

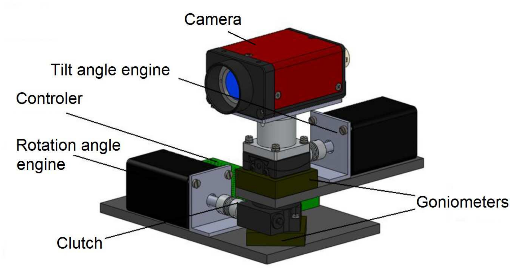

Figure 6.7: Mechanical Camera Positioning Tool.

A first rotation stage ensures the ϕ angle, while the second manipulates the θ angle. The Ψ angle is not included in this platform, as this is in plane rotation, which is accepted by DIC. The rotation stage is controlled by stepper motors, performing 200 steps per revolution. Because of the stepper motors, the rotation angles can be controlled very precisely. The angles needed to rotate the camera are obtained using a standard single camera calibration system. The only extra step in the procedure is the inclusion of one extra picture (see 6.4.1). This picture is taken when the calibration target is held against the clamped specimen. By holding the target against the specimen, they can be assumed to be parallel, and thus, this image can be used to obtain the camera position relative to the specimen. The performance of this rotation stage is presented in Table 6.2.

	Degr/rot	**Motor**	**Degr/step**
θ	8.00	200 steps	0.04
ϕ	2.17	200 steps	0.01

Table 6.2: Goniometer specifications.

To assess the accuracy of the tool, again 10 calibrations are performed to validate the perpendicularity between the camera and the specimen. The obtained positions are shown in Fig 6.8. To make comparison possible, the same scale as for the manual positioning is used.

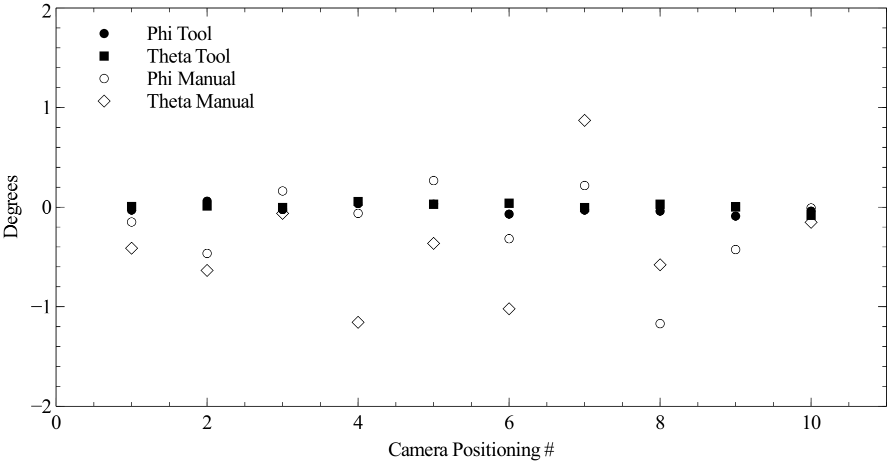

Figure 6.8: Camera positions using mechanical tool alignment.

Results clearly indicate an improvement of the positioning. The data in Table 6.3 indicate that the tool is capable of positioning the camera ±0.15 degree perpendicular.

	Average	**Deviation**
θ	-0.12	0.12
ϕ	-0.02	0.14

Table 6.3: Camera positions using mechanical tool alignment.

Hereby, it is shown that manual camera positioning leads to non-perpendicular alignment of the camera towards the camera. It is also shown that using a mechanical positioning tool, consistent perpendicular camera positioning are obtained. In what follows the camera will be put manually "perpendicular" to the specimen and any remaining misalignments will be compensated numerically.

Numerical Alignment.

The second way to align the camera to the loading direction is to rectify the image numerically, as previously done in [90]. A brief explanation follows. The image rectification procedure numerically transforms the non-perpendicular image to an image as it was taken by a perpendicular set-up.

It is clear that one has to know the camera parameters as they will strongly influence the quality of results. These parameters are determined using the same procedure as discussed above. After the calibration the 6 external parameters (rotations R and translations T of the camera according to the world reference frame) and the 8 internal camera parameters f_x, f_y, f_s (focal lengths), c_x, c_y (image plane center location) and $\kappa_1, \kappa_2, \kappa_3$ (lens distortion coefficients) are determined.

The first step of the rectification process is the removal of the distortion due to the lens; the 3 radial distortion parameters ($\kappa_1, \kappa_2, \kappa_3$) are used to calculate an ideal distortion-free image. It is clear that the quality of the results heavily depend on the results of the calibration. After the removal of the distortions the four corners of the undistorted image are converted from sensor (x_s^u, y_s^u) to world coordinates (X_W, Y_W, Z_W) by using the equations in [1]:

$$\begin{bmatrix} x_s^u \\ y_s^u \end{bmatrix} = \begin{bmatrix} c_x + f_x \frac{R_{11}X_W + R_{12}Y_W + T_x}{R_{31}X_W + R_{32}Y_W + T_z} + f_s \frac{R_{21}X_W + R_{22}Y_W + T_y}{R_{31}X_W + R_{32}Y_W + T_z} \\ c_y + f_y \frac{R_{21}X_W + R_{22}Y_W + T_y}{R_{31}X_W + R_{32}Y_W + T_z} \end{bmatrix} \tag{6.3}$$

Where $Z_W = 0$. The R-factors are the elements of the rotation-matrix when using Euler-angles and θ is the rotation around the x-axis, ϕ is the rotation around the y-axis, ψ is the rotations around the z-axis:

$$[R] = \begin{bmatrix} R_{11} & R_{12} & R_{13} \\ R_{21} & R_{22} & R_{23} \\ R_{31} & R_{32} & R_{33} \end{bmatrix} = \begin{bmatrix} 1 & 0 & 0 \\ 0 & \cos(\theta) & \sin(\theta) \\ 0 & -\sin(\theta) & \cos(\theta) \end{bmatrix} \begin{bmatrix} \cos(\phi) & 0 & -\sin(\phi) \\ 0 & 1 & 0 \\ \sin(\phi) & 0 & \cos(\phi) \end{bmatrix} \begin{bmatrix} \cos(\psi) & \sin(\psi) & 0 \\ -\sin(\psi) & \cos(\psi) & 0 \\ 0 & 0 & 1 \end{bmatrix} \tag{6.4}$$

Finally the image is constructed by calculating the location of each pixel of the rectified image in the old, non-perpendicular, image by applying the inverse transformations. This transformation is done using equation 6.3, but now using matrix R' defining the perpendicular position of the camera. Similar as for the mechanical tool, 10 rectifications are performed to determine the accuracy of the rectification method. After rectification, the calibration images are recalibrated to determine the final angle. The obtained angles are shown in Fig 6.9 and Table 6.4.

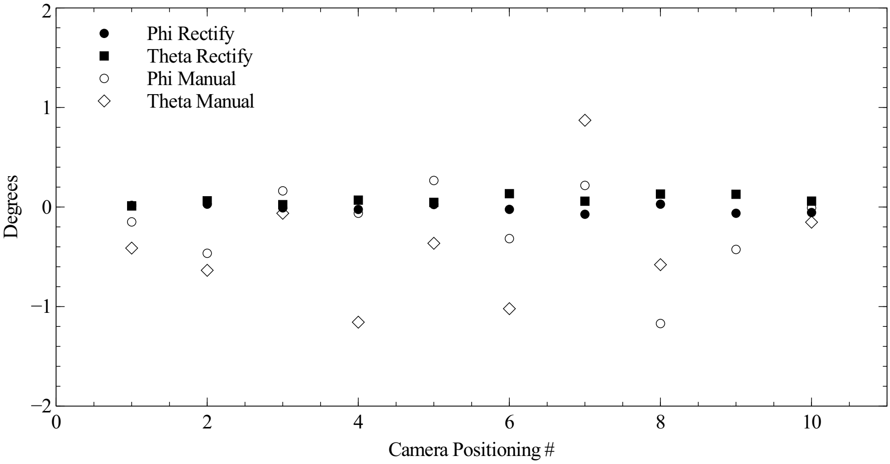

Figure 6.9: Camera positions using numerical alignment.

	Average	**Deviation**
θ	-0.07	0.01
ϕ	-0.05	0.04

Table 6.4: Accuracy numerical rectification.

The effect of this rectification-process is described in [90]; a brief summary follows. As one can presume, the rectified image yields better results than the non-perpendicular image. The errors made in a non-perpendicular set-up rise with a higher degree of non-perpendicularity (in contrast to stereo-DIC where the degree of non-perpendicularity has no influence on the results). Image rectification also yields better results in comparison with stereo-DIC due to the fact that the main error sources in stereo-DIC (there will be no triangulation, cross-camera matching, nor will there be multiple correlation runs) are avoided. However, interpolation errors are introduced as the image is corrected and the results heavily depend on the quality of the calibration; if the parameters are not precise, a good rectification is impossible. Despite the fact that the rectification tool has better results than the stereo and the non-perpendicular set-up, a true perpendicular set-up yields the best results overall.

Finally, in Fig 6.10, the dependency of the accuracy in relation to the starting position is shown. It is clearly seen that the accuracy of the tool is not influenced by the starting position of the camera, the tool always obtains a final angle of 0.1 degree or lower.

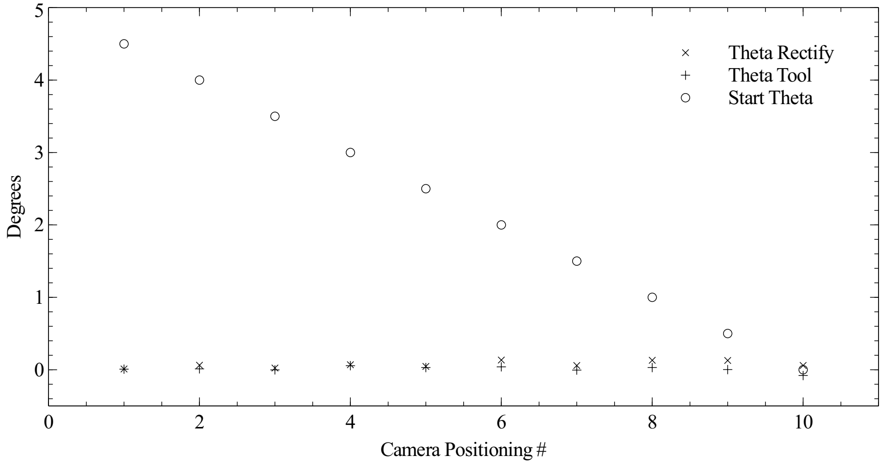

Figure 6.10: Starting positions for aligning the camera with the mechanical and numerical tool

Region of Compensation.

The original concept of the Region of compensation (ROC) is introduced by Pan et al. The basic principle consists of correcting the deformations in the specimen by using a region that does not deform but only follows the specimens body movements. The region used for compensation, denoted as ROC and shown in Fig 6.11, is obtained by attaching a frame on a specimen. The main hypothesis behind this methodology is that the ROC only rigidly moves with the specimen and will not deform under loading of the specimen. A second assumption made is that the ROC will not influence the behaviour of the specimen tested. To correct the measurement in the ROI (Fig 6.12B), a polynomial is fitted into the displacements of the ROC (Fig 6.12A) and subtracted from the original measurements (Fig 6.12C).

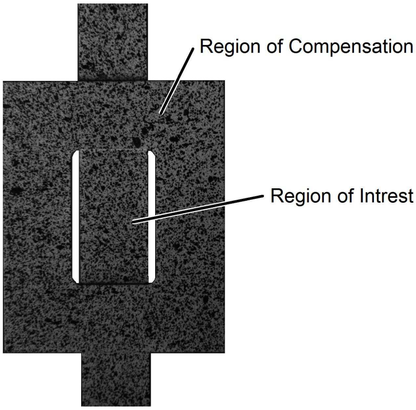

Figure 6.11: Identifying ROI and ROC on the used specimen..

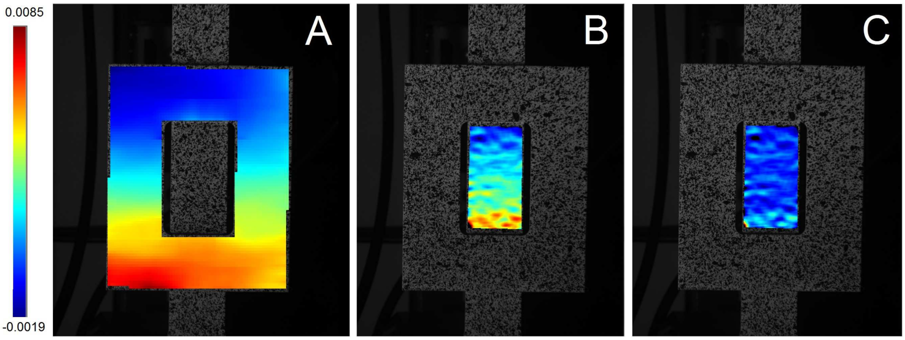

Figure 6.12: A) Region of Compensation B) Region of Interest C) Compensated Field

The displacements of the ROC are modelled as a second order polynomial, as the strain field is expected to be constant or linear (See 6.3).

$$\begin{aligned} u_{ROC} &= a_0 + a_1x + a_2y + a_3xy + a_4x^2 + a_5y^2 \\ &\quad + a_6x^2y + a_7xy^2 + a_8x^2y^2 \\ v_{ROC} &= b_0 + b_1x + b_2y + b_3xy + b_4x^2 + b_5y^2 \\ &\quad + b_6x^2y + b_7xy^2 + b_8x^2y^2 \end{aligned} \tag{6.5}$$

Using this fitted displacement of the ROC, the ROI can be corrected.

$$\begin{aligned} u_c &= u_{ROI} - u_{ROC}(x,y) \\ v_c &= v_{ROI} - v_{ROC}(x,y) \end{aligned} \tag{6.6}$$

These corrected displacement fields can then be used to determine the corrected strain field. Please note that correcting the image will not only remove out of plane movement but will also correct for rigid body motions and lens distortions because all the movement of the ROC is compensated.

The compensation of lens distortions is even more clear when the original compensation surface is used, rather than the second order polynomial used here. The original method used:

$$\begin{aligned}
u_{ROC} &= a_0 + a_1 x_{ci} + a_2 y_{ci} + a_3 x_{ci}^2 + a_4 x_{ci} y_{ci} \\
&\quad -k_1 \left[x'_{ci} \left(x'^2_{ci} + y'^2_{ci} \right) - x_{ci} \left(x_{ci}^2 + y_{ci}^2 \right) \right] \\
v_{ROC} &= b_0 + b_1 x_{ci} + b_2 y_{ci} + b_3 x_{ci} y_{ci} + b_4 y_{ci}^2 \\
&\quad -k_1 \left[y'_{ci} \left(x'^2_{ci} + y'^2_{ci} \right) - y_{ci} \left(x_{ci}^2 + y_{ci}^2 \right) \right]
\end{aligned} \tag{6.7}$$

where a_0 and b_0 refer to the in-plane rigid motions; $a_1, a_2, a_3, b_1, b_2, b_3$ are used to correct the rigid motions such as the in-plane motions and the out-of-plane translations and rotations; k_1 represents the lens distortions. Do note that the current, polynomial approach equally compensates the lens distortions. The only difference is that the distortion parameters are embedded in the polynomial fit and thus cannot be retained from the fitted plane.

6.4.2 Overview

In Fig 6.13, an overview of the discussed compensation methods is given.

In Table 6.5, the advantages and disadvantages of the compensation methods are listed.

	Mechanical	Numerical	Compensation
Type Manipulation	HW	SW	HW + SW
Specimen Manipulation	No (+)	No (+)	Yes (-)
ROI / FOV Limitation	No (+)	No (+)	Yes (-)
Limited by deformation	No (+)	No (+)	Yes (-)
Data Manipulation	No (+)	Yes (-)	Yes (-)
Compensate during test	No (-)	No (-)	Yes (+)

Table 6.5: Advantages and disadvantages of the compensation methods used in this work. HW= Hardware solution, SW=Software solution, +=Advantage, -= Disadvantage. FOV = Field of View.

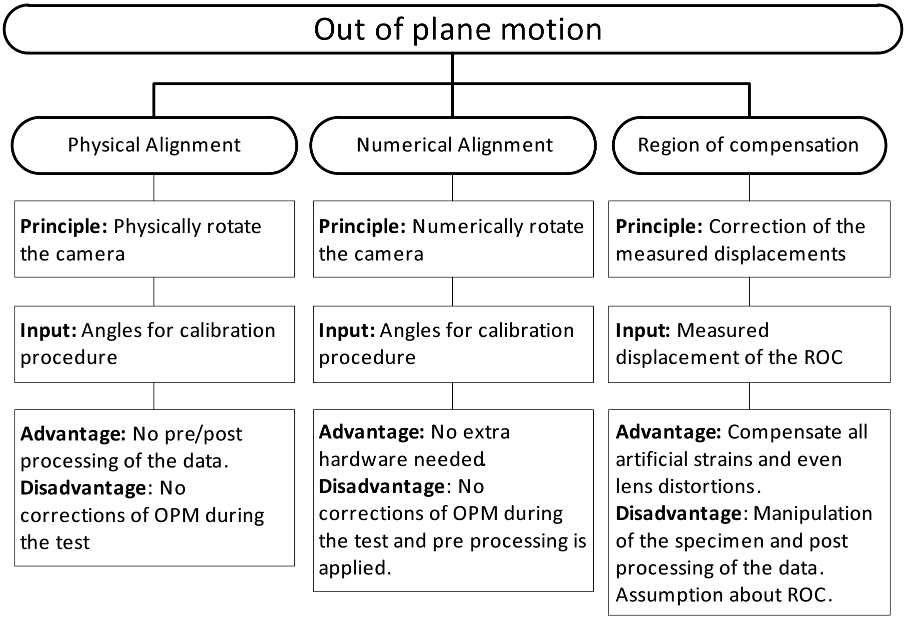

Figure 6.13: Overview OPM compensations.

6.5 Compensation of lens distortions

Although the methods were developed to compensate out of plane motion, some of them are capable of also compensating lens distortions. The effect of lens distortions has been investigated in [36][91], denoting the importance of compensating lens distortions. The first compensation method, physical alignment, is unable of dealing with lens distortions as no pre- or post-processing of the data is performed. The remaining two compensation methods are capable of reducing the measurement error introduced by lens distortions. For the ROC this is embedded in the polynomial fit made on the artificial displacement field. The artificial field will contain both OPM as lens distortions. When the polynomial proposed by Pan et al. is fitted in the displacement field then the lens distortions are represented by k_1. For the numerical method, the effect of lens distortions can also be compensated as the lens distortion coefficients are known from the calibration process. This has been successfully done in [6] and [90]. The difference with the ROC method is that for the numerical rectification OPM and lens distortions are treated separately.

6.6 Experimental setup

The procedures described above are validated in an experimental setup. The validation will be divided into two parts, first only rigid body motions are introduced. Due to out of plane movements, artificial strains are measured. When the compensations for out of plane motions are applied, the artificial strains should resolve. The quantity of artificial strain will be an indication of the performance of the compensation methods. In the second stage, a real tensile test will be performed. In this tensile test the strain field is validated with the knowledge that a more or less homogeneous field is expected. Even further the material parameters can be validated using the different compensation methods.

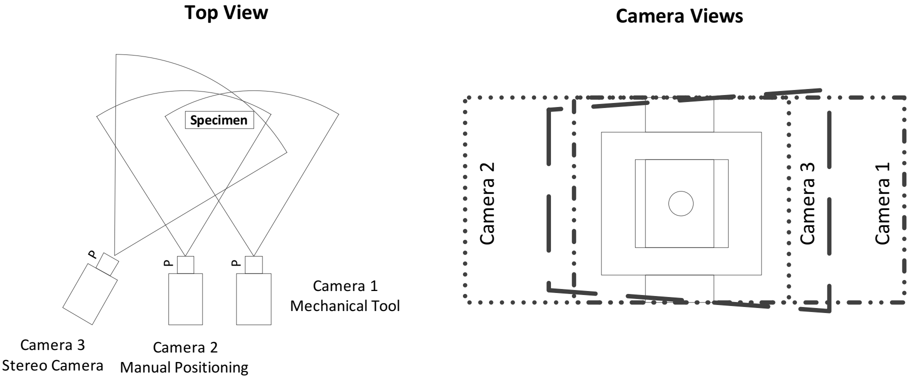

Figure 6.14: Principle of the testing setup with frame 3 the stereo camera, frame 2 the manual positioned camera, and frame 1 the perpendicular camera.

Both stages of the validation will be done on the same setup. In this setup, three cameras are used to measure the same experiment. Two cameras are put perpendicular to the specimen, a third camera is used for obtaining stereo vision. The principle of the setup can be seen in Fig 6.14, the actual setup is seen in Fig 6.15. Camera one will be used for the physical alignment. Camera two is used for the numerical compensation and region of compensation approach. The camera is put perpendicular manually, resulting in a non-alignment of 1 degree equivalent to the accuracy determined in Section 6.4.

For the speckle pattern, to be seen in Fig 6.11, DIC setup/settings shown in Table 6.6 and 6.7 are used.

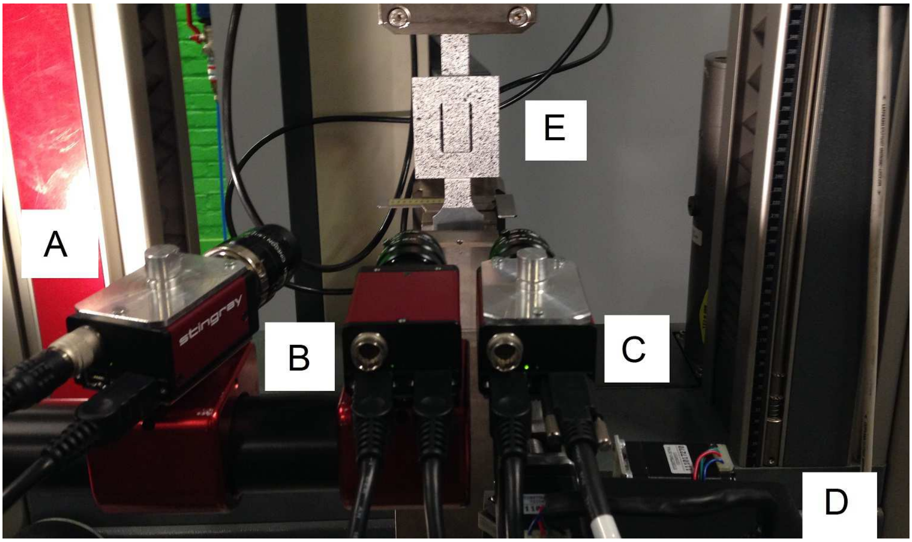

Figure 6.15: Testing setup with A the stereo camera 3, B the manual positioned camera 2, C the perpendicular camera 1 mounted on the mechanical tool D. E is the tested specimen.

Experimental	
Sensor and digitalisation	1624 x 1234; 8 bit
Camera Noise	0.6 %
Lens and imaging distance	12mm F-mount, 0.270m
Imaging speed	2 Hz
Field Of View (needed)	65 x 80 mm

Table 6.6: Experimental setup details.

Correlation	
Subset	31 pixels (Affine)
Step	2
Strain Window	15
Virtual Strain Gauge	29 pixels
Interpolation	Bicubic
Correlation Criteria	NSSD
Displacement Resolution	$9 \cdot 10^{-3}$ pixels
Strain resolution	$3.8 \cdot 10^{-4}$

Table 6.7: Correlation details.

6.6.1 Results

Rigid body motions

In the first stage, the specimen is translated vertically (Fig. 6.16). No deformation will occur as rigid body motion is performed. When the translated images are correlated, an artificial strain field will be measured for each compensation method. As mentioned above, the amount of artificial strain will be an indication of the performance of the compensation method.

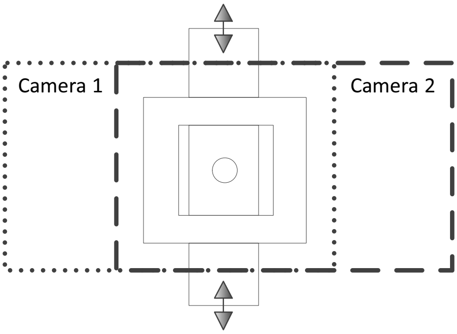

Figure 6.16: Testing principle for rigid body motions.

The results will be presented as "artificial strain", representing the average of the strains ϵ_{xx} and ϵ_{yy}. The average is used in the validation because, as shown above, an out of plane movement will introduce a constant artificial strain field approximated by $\frac{\Delta z}{Z}$. The specimen is moved along the y-axis ranging from 0 to 16mm in steps of 1mm. At each step images are taken and artificial strains analysed.

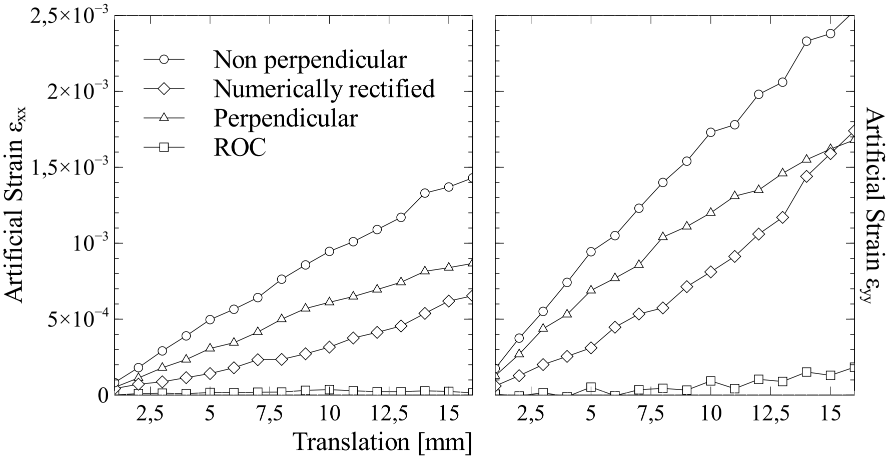

Figure 6.17: Artificial strain for translations.

The results are shown in Fig 6.17 and 6.18. Both graphs clearly indicate that increasing the translation introduces extra out of plane motion, resulting in larger artificial strains. The difference between the aligned camera and the non-aligned camera is also obvious; the strains get reduced with approximately 50%. The strains left in the aligned image, see Fig 6.18, can be assigned to the remaining misalignment or to the extra out of plane movements introduced by the tensile bench.

When the stereo system is used as benchmark, The out of plane movement and rotation of the specimen can be retrieved. For a translation of 16mm it is seen that the specimen has an extra out of plane movement of 0.115mm, and a rotation around the y axis of 0.125 degree. Compensating this known error from the artificial strains, the remaining error for the rectifying methods can be verified.

$$\epsilon_{Artificial_{xx}} = -\frac{\Delta Z}{Z} - \frac{y_s sin\theta}{Z} \tag{6.8a}$$

$$\epsilon_{Artificial_{yy}} = -\frac{\Delta Z}{Z} + cos\theta - 1 - \frac{y_s sin2\theta}{Z} \tag{6.8b}$$

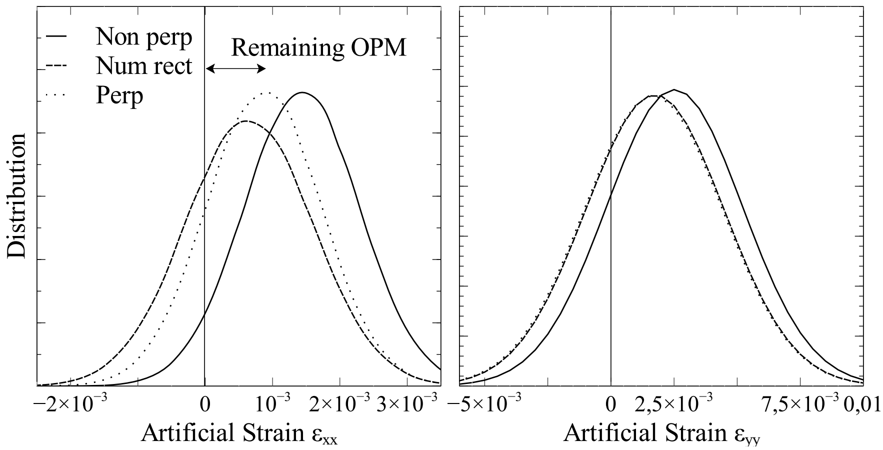

Figure 6.18: Artificial strain distribution at translation 16mm.

With $Z = 270$mm obtained from the calibration and ΔZ and θ obtained from the 3D measurement. When correcting the strains, the remaining error is shown in Fig 6.19.

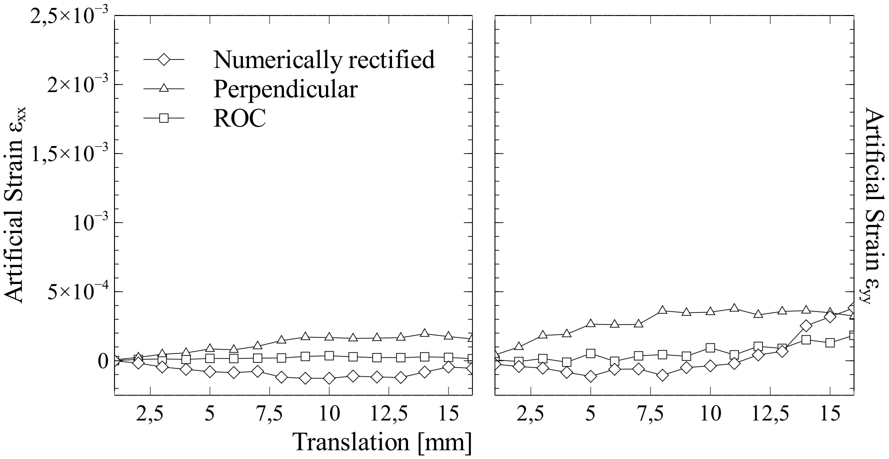

Figure 6.19: Corrected artificial strain during translation using the measured out of plane motions with a stereo setup.

Fig 6.17 and 6.18 shows that the ROC method reduces the artificial strain to almost zero, as it will correct all strains occurring in the specimen. This validation shows that the tool is capable of improving the strains considerably, while the ROC seems to be able to compensate all out of plane motions occurring. We do note that the ROC performs this well because no deformation is introduced and the two assumptions made in the beginning are met perfectly. The ROC does not influence the specimen's behaviour and will follow the exact movement of the specimen. We also see that the rectifying tools do accurately compensate the out of plane motions invoked by a misalignment of the camera. That the ROC is capable of compensating out of plane motions occurring during the test is clearly illustrated here. An experimental validation follows to see the performance of the methods in experimental conditions.

Tensile test

As a final stage, the specimens are loaded in a tensile test. In the tensile test, two different specimens are used. First, a normal dog bone, without perforation used to have a reference of the used material. Second, a perforated dog bone with ROC is used in the tensile test. The location of the specimens is unchanged as shown in Fig 6.20.

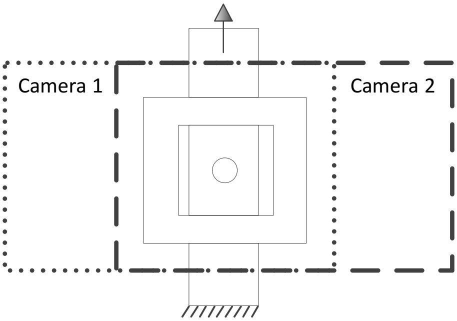

Figure 6.20: Testing principle for the tensile test.

Both specimens are loaded in the elastic regime. During loading, multiple images are taken, and synchronised with the applied force. Using the VFM, material parameters can be obtained for each loading step using the force and the deformation measured with DIC. In this validation, the focus will be on the Poisson ratio, as this material property is heavily influenced by out of plane motions. The material used in the experimental test is Aluminum AL6081T having a Poisson ratio of 0.33.

Because the loading is in the elastic region, the Poisson ratio should remain constant during the loading. For each setup (Perpendicular camera, non perpendicular camera, rectified camera and ROC setup), a box plot with the identified Poisson ratio during the loading could be plotted. The results of the stereo setup will be used as the reference as this setup is not influenced by out of plane motions and thus will yield the best results. The results for the non perforated specimen are shown in Fig 6.21.

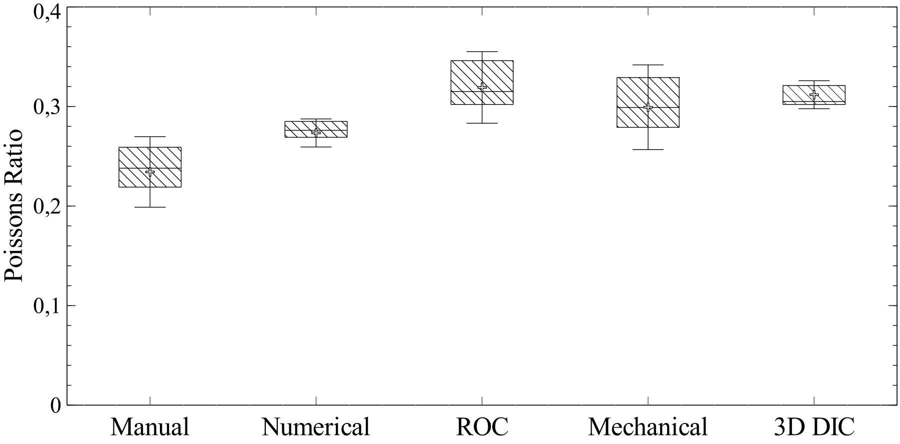

Figure 6.21: Identified Poissons ratio for a standard dogbone specimen under tensile loading for the manual positioned camera, the mechanically rectified setup, the numerical rectified setup and a stereo setup.

Fig 6.21 clearly shows the influence of the compensation methods on the identified Poisson ratio. As the Poisson ratio is dependent on the ratio between ε_{xx} and ε_{yy}, it will be very sensitive to artificial strains. Reducing these artificial strains (See Fig. 6.17) improves the Poisson ratio considerably. Firstly, comparing the physical aligned camera with the non aligned camera reveals the importance of a good experimental setup. It is seen that the ratio from the aligned setup matches the ratio from the 3D setup, while the non perpendicular camera identifies a ratio with an error of 25%. When analysing the method of compensation (ROC), it is seen that it has the same performance of the aligned camera. Finally, the numerical rectifying method was able of reducing the error (to 12%) but could not obtain the same accuracy of the other methods. The remaining error can be from the quality of the camera parameters used for the deformation, or the introduction of interpolation errors from the numerical image generation. We do note that, although the mechanical tool and ROC have the same performance, the mechanical tool is preferred as it does not limit the experimental setup (no extra region needed), the specimen is not altered (no attached ROC) and the DIC data is not manipulated.

To confirm the conclusion made before even in heterogeneous deformations, a second test is performed using a perforated specimen. The exact same setup is used, but the specimen is replaced. The specimen is loaded in the elastic regime while images are taken. From these images, the Poisson ratio is obtained using all three correction methods. The results from this test is shown in Fig 6.22 and indicate the same trends as discussed above.

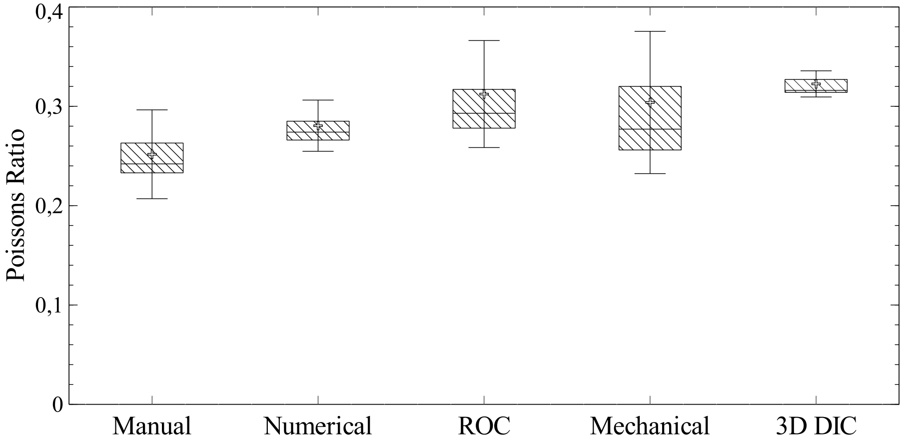

Figure 6.22: Identified Poissons ratio for a perforated dogbone specimen under tensile loading for the manual positioned camera, the mechanically rectified setup, the numerical rectified setup and a stereo setup.

6.7 Conclusion

In this paper, the problem of out of plane motion in a 2D DIC setup is addressed. More specifically, methods to compensate this motion are introduced and compared to a 3D reference setup. Three methods are included in this work. First of all, the camera is aligned perpendicularly to the specimen to avoid out of plane motion due to miss alignment. This alignment is done with a mechanical tool where the camera is mounted on. The camera's perpendicularity is controlled and checked using a single camera calibration system. The second approach is again the camera alignment, but now not the camera but the images are numerically "rectified" using again a single camera calibration system. The last method to compensate is not done before the test, but is post processing of the data. A region, attached to the specimen, is assumed to not deform and will be used to identify the artificial strains. This region is called region of compensation and is used to correct the region of interest. It is noted that it is assumed that the ROC will follow the specimens rigid body motions, will not deform and will not influence the specimens behaviour. The validation has shown that all three methods are capable of compensating out of plane motions. The ROC has proven to be very effective as it will compensate all motions, even the ones occurring due to other sources than camera alignment. The validation on real tensile test resulted in a clear conclusion. The numerical tool has the least performance due to its dependency on camera parameters, interpolations and others. The mechanical tool and ROC performed similarly. Between both, the mechanical tool is more favourable because it does not introduce any data manipulations. Further it does not limit the setup or holds any assumptions compared to the ROC. On the other hand, the ROC is easier to implement as less effort is needed to obtain the setup.

Chapter 7

Conclusions and future works

The main objective of the present dissertation was the development of a self adaptive algorithm for measuring small strains with high strain gradients as this remains cumbersome using the traditional DIC approaches. The main focus has been the development of an adaptive algorithm and the development of a procedure for controlling the refinement of the mesh to reduce the influence of user input, which is the main disadvantage of current implemented methods. The aforementioned topics were presented in two articles, included in the present dissertation as Chapter 3 and Chapter 4. Furthermore, a possible improvement towards continuity has been investigated. To finalise, contributions to improve the experimental setup for 2D DIC have been included, as, for now, the algorithm is only developed in 2D. Both last mentioned topics were also presented in two peer-reviewed papers.

In what follows each chapter is briefly summarised and a conclusion stated.

7.1 Adaptivity in Global DIC

In Chapter 3, the new global DIC algorithm was presented. The algorithm adopts features from the concept of adaptive FEA. The region of interest is described by an adaptive element mesh. A p-refinement scheme is implemented so the elements in the mesh are capable of rising in degrees of freedom when the error estimators indicate them to do so. Using measurand resolution and spatial resolution, a validation of the traditional local and newly presented p-DIC is performed. Results from the validation indicate that the p-DIC method has a lower measurand resolution for the same spatial resolution compared to the local method. Also from the strain validation it can be concluded that for the accurate measurement of low spatial strain fields the p-DIC method is more favourable than the local method. Besides the advantage in performance at optimal settings, another major advantage is less user dependent results of the method by using the self adapting mesh. The spatial resolution is, in comparison to the local method, not limited by initial user settings. The self adaptive mesh is controlled using error estimators and absolute error boundaries. In the following chapter, this procedure was improved.

We do note that this manuscript is a summary of publications. Because there is continuous development in DIC, some of the statements in this chapter must be revised. At the time of publication, the h-refinement scheme was less beneficial in terms of element size and pDIC was the first adaptive algorithm. After publication however, progress was made in global DIC. The h-refinement scheme was greatly improved achieving elements the size of pixels and the concept of automatic refinement was further explored.

7.2 Convergence in Global DIC

The original adaptive approach used an absolute error boundary for controlling the refinement procedure. As this absolute value is difficult to obtain, a major improvement to the refinement procedure was presented. The principle of convergence in "strain energy" was introduced in the global DIC approach. The concept of using convergence in displacement and strain norms, originating from the adaptive finite element analysis, is implemented in the previous mentioned adaptive method. Hereby, a fully automatic adaptive global DIC procedure is achieved where an intuitive relative error is supplied to the adaptive algorithm. The proposed concept has proven to be valid on an illustrating example introducing different spatial resolutions as a function of the x-coordinate. The automatic, convergence driven global DIC algorithm was capable of determining appropriate element orders without any preknowledge of the deformation field. Furthermore, it has been shown that even the element size does not influence the final results, but only influences the polynomial order of the elements. In addition, the robustness to experimental influences is investigated. The validation showed that the refinement procedure is able to cope with varying noise and light conditions as well as with different correlation criteria. After the validation, three specific experiments are chosen and conducted. First, a standard tensile test on a perforated specimen is performed. Here plastic strains occur, indicating that the method can work beyond elastic cases. Second, a shear test is performed to achieve very concentrated strain peaks embedded in a homogeneous deformation. Finally, and in contrast to previous specimens, a disc in compression is used to obtain very small strains. The applications also implied the different steps a user can undertake in the correlation. Ranging from accepting the correlation, to reducing the convergence boundary to even discard criteria to boost the algorithm. It is stressed that altering the convergence criteria is only boosting the refinement procedure and is not necessary for a standard correlation.

7.3 Continuity in Global DIC

The influence of continuity in DIC has been investigated. This was done by using 4 different DIC approaches possessing totally different characteristics. The first approach is the traditional subset method which has no continuity in the displacement field. Secondly, the widely known Q4-DIC is used. Here a first order finite element mesh, introducing C^0-continuity is used for tracking the deformation. As third method, the proposed self adaptive higher order global method, also containing C^0-continuity, is used. As last, a special developed p^{th} order global C^1-continuous DIC algorithm named c-DIC is used. The newly proposed algorithm is based on global DIC and uses C^1-continuous elements with a generic p^{th} order description. The generic description allows that elements can vary in both size as order while remaining C^1-continuous. It is concluded that the local method (C^{-1}), the higher order method (C^0-p) and the newly proposed C^1 approach are competitive to each other. The C^0-Q4 method performed less as the linear elements constrain the element's deformation flexibility and thus the spatial resolution. The algorithm to use in a certain application, will be chosen mostly based on the specific requirements of the measurement. A complex measurement with many discontinuities, is best performed using the local method. Is the deformation field unknown, one rather chooses C^0-p as here automatic non uniform refinement is possible and thus both homogeneous and heterogeneous deformation regions will be adapted most efficiently. On the other hand, when explicitly a C^1-continuous field is requested e.g. with beam kinematics, the C^1 approach is a valuable alternative towards the other methods.

7.4 Out of plane motions

As closure to this thesis, the problem of out of plane motion in a 2D DIC setup was addressed. More specifically, methods to compensate this motion are introduced and compared to a 3D reference setup. Three methods are included in this work. First of all, the camera is aligned perpendicularly to the specimen to avoid out of plane motion due to misalignment. This alignment is done with a mechanical tool where the camera is mounted on. The camera's perpendicularity is controlled and checked using a single camera calibration system. The second approach is again the camera alignment, but now not the camera but the images are numerically "rectified" using again a single camera calibration system. The last compensation method is post processing of the data. A region, attached to the specimen, is assumed to not deform and will be used to identify the artificial strains. This region is called region of compensation and is used to correct the region of interest. It should be noted that the ROC is assumed to follow the specimen's rigid body motions, will have no deformation and will not influence the specimens behaviour. The validation has shown that all three methods are capable of compensating out of plane motions. The ROC has proven to be very effective as it will compensate all motions, even the ones occurring due to other sources than camera alignment. The validation on a real tensile test resulted in a clear conclusion. The numerical tool has the lowest performance due to its dependency on camera parameters, interpolations and others. When comparing the mechanical tool and ROC, both performed similar. Between both, the mechanical tool is more favourable because it does not introduce any data manipulations. Further it does not limit the setup or holds any assumptions compared to the ROC.

7.5 Future works

Correlation procedure

In the present work, the first mathematical framework for a fully automated procedure is presented. Several improvements can be done:

- The development towards error/convergence estimations can be expanded. In the current implementation, when no convergence is found, no solution is obtained. The development of more robust estimators could bring a solution.
- The algorithm can be sped up by a more intelligent refinement procedure. In current implementations element orders are increased when no convergence is reached. Hereby multiple correlation passes are needed. When an indication could be given on what the order should be, as in FEA, a single pass procedure should become possible.

- Refinement is now pure p- refinement. However, a combination of h- and p-refinement would be a great addition to the algorithm. In this way, the results might become completely user independent.
- The extension to a stereo application is still left to be done. The method's capability towards a stereo setup has been validated though. It has been shown that it is capable of cross correlating stereo imaging and thus stereo should be possible.

Applications

- The p-element mesh could be coupled to a p-finite element simulation package. Because the element size is now not a limiting factor in the DIC approach. Exactly the same mesh could be used and thus no mapping between both deformation field and simulated field is needed. This could improve current FEMU approaches.
- The algorithm can be used in several applications where a high spatial deformation field is expected and so, hopefully, prove its usability. Examples of such applications can be composites, bio-materials or any material/application posing difficulties to the local method.

Appendix A

Legendre shape functions

Legendre shape functions are a combination of function $P_p(\chi)$:

$$P_p(\chi) = \frac{1}{(p-2)!2^{p-2}} \frac{d^{p-2}}{d\chi^{p-2}}[(1-\chi^2)^{p-1}] \tag{A.1}$$

The first six functions $P_p(\chi)$ are shown as example:

$$\begin{array}{lcl} P_0(\chi) & = & (1-\chi) * 0.5 \\ P_1(\chi) & = & (1+\chi) * 0.5 \\ P_2(\chi) & = & 1-\chi^2 \\ P_3(\chi) & = & 2\chi^3 - 2 * \chi \\ P_4(\chi) & = & -\frac{15}{4} * \chi^4 + \frac{9}{2} * \chi^2 - \frac{3}{4} \\ P_5(\chi) & = & 7 * \chi^5 - 10 * \chi^3 + 3 * \chi \\ P_6(\chi) & = & -\frac{105}{8} * \chi^6 + \frac{175}{5} * \chi^4 - \frac{75}{8} * \chi^2 + \frac{5}{8} \\ P_n(\chi) & = & \cdots \end{array} \tag{A.2}$$

In a p-element shape functions are assigned to nodes, edges or faces identified in Fig A.1.

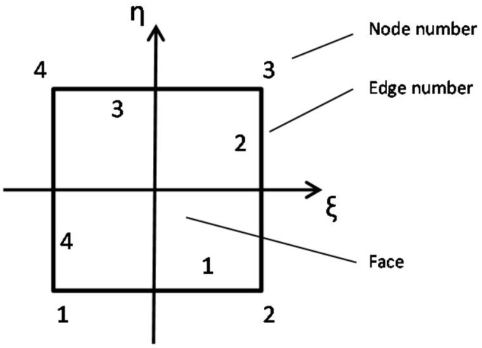

Figure A.1: Element nodes, edges and face.

The shape functions that can be used are shown in Table A.1 with p the polynomial order.

Table A.1: Hierarchical shape functions.

Object	Shape function
Node 1	$P_0(\xi)P_0(\eta)$
Node 2	$P_1(\xi)P_0(\eta)$
Node 3	$P_1(\xi)P_1(\eta)$
Node 4	$P_0(\xi)P_1(\eta)$
Edge 1	$P_p(\xi)P_0(\eta)$
Edge 2	$P_1(\xi)P_p(\eta)$
Edge 3	$P_p(\xi)P_1(\eta)$
Edge 4	$P_0(\xi)P_p(\eta)$
Face	$\sum_{k=1}^{p-3} P_{k+1}(\xi)P_{p-1-k}(\eta)$

Appendix B

Inverse Mapping

Assume mapping functions $X^e(\xi, \eta)$ and $Y^e(\xi, \eta)$ and their derivatives $\frac{\delta X^e(\xi,\eta)}{\delta \xi}$, $\frac{\delta X^e(\xi,\eta)}{\delta \eta}$ $\frac{\delta Y^e(\xi,\eta)}{\delta \xi}$ and $\frac{\delta Y^e(\xi,\eta)}{\delta \eta}$.

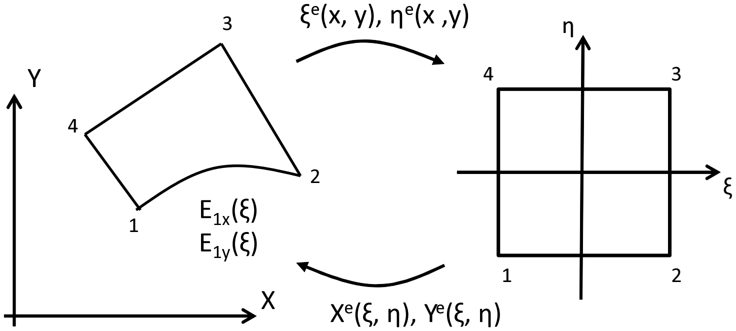

Figure B.1: Mapping functions between local and global systems.

It is generally known that the inverse mapping $\xi^e(x, y)$ and $\eta^e(x, y)$ does not explicitly exist [63]. For that reason an alternative scheme is needed to invoke an inverse mapping. Note that this inverse mapping is not used in the algorithm it self. The inverse mapping is only used in the post processing stage, when data at a specific (x_g, y_g) is requested.

The local coordinate (ξ, η) within an element e for the global coordinate (x_g, y_g) could be described as:

$$(\xi, \eta) = (\xi_0, \eta_0) + (\Delta\xi, \Delta\eta) \tag{B.1}$$

where $(\xi_0, \eta_0) = (0, 0)$ so that:

$$\begin{array}{rcl} X^e(\xi_0 + \Delta\xi, \eta_0 + \Delta\eta) & = & x_g \\ Y^e(\xi_0 + \Delta\xi, \eta_0 + \Delta\eta) & = & y_g \end{array} \tag{B.2}$$

Using a first order Taylor expansion, Eq. B.2 can be written as:

$$\begin{array}{rcl} x_g & = & X^e(\xi_0, \eta_0) + \Delta\xi \frac{\delta X^e(\xi_0,\eta_0)}{\delta\xi} + \Delta\eta \frac{\delta X^e(\xi_0,\eta_0)}{\delta\eta} \\ y_g & = & Y^e(\xi_0, \eta_0) + \Delta\xi \frac{\delta Y^e(\xi_0,\eta_0)}{\delta\xi} + \Delta\eta \frac{\delta Y^e(\xi_0,\eta_0)}{\delta\eta} \end{array} \tag{B.3}$$

Defining matrices A, D and X;

$$A = \begin{bmatrix} \frac{\delta X^e(\xi_0,\eta_0)}{\delta\xi} & \frac{\delta X^e(\xi_0,\eta_0)}{\delta\eta} \\ \frac{\delta Y^e(\xi_0,\eta_0)}{\delta\xi} & \frac{\delta Y^e(\xi_0,\eta_0)}{\delta\eta} \end{bmatrix} \tag{B.4}$$

$$D = \begin{bmatrix} \Delta\xi \\ \Delta\eta \end{bmatrix} \tag{B.5}$$

$$X = \begin{bmatrix} x_g - X^e(\xi_0, \eta_0) \\ y_g - Y^e(\xi_0, \eta_0) \end{bmatrix} \tag{B.6}$$

This system of equation can be solved to $\Delta\xi$ and $\Delta\eta$ using following Matrix equation:

$$[D] = [A]^{-1}[X] \tag{B.7}$$

As a Taylor expansion is used, an iterative procedure is used where (ξ_0, η_0) is updated by $(\xi_i, \eta_i) = (\xi_{i-1} + \Delta\xi, \eta_{i-1} + \Delta\eta)$ and $\Delta\xi, \Delta\eta$ is recalculated until $(\Delta\xi, \Delta\eta) \approx (0, 0)$. In that case:

$$\begin{array}{c} \xi^e(x_g, y_g) = \xi \approx \xi_i \\ \eta^e(x_g, y_g) = \eta \approx \eta_i \end{array} \tag{B.8}$$

Appendix C

Mesh sizes

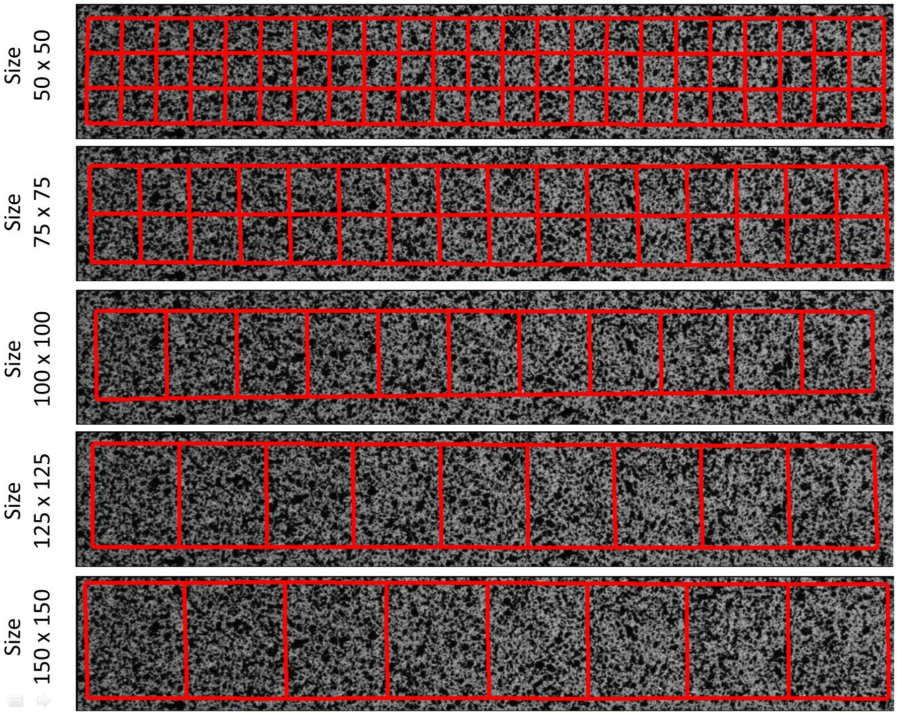

Figure C.1: Meshes with elements ranging from 50 to 150 pixels, used for the explanatory example.

Appendix D

Shape functions 6^{th} order element

In this appendix, some details are provided for calculating a sixth order element. The element is illustrated in Fig. D.1.

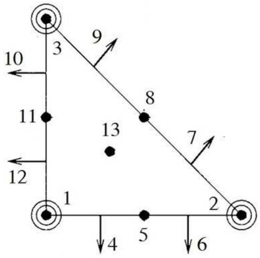

Figure D.1: Sixth order element.

For this sixth order element, a sixth order base β is defined:

$$\beta = \{1, x, y, x^2, xy, y^2, x^3, x^2y, xy^2, y^3, x^4, x^3y, x^2y^2, xy^3, \cdots$$
$$\cdots y^4, x^5, x^4y, x^3y^2, x^2y^3, xy^4, y^5, x^6, x^5y, x^4y^2, x^3y^3, x^2y^4, xy^5, y^6\} \quad \text{(D.1)}$$

Using this base the generalised Vandermonde matrix $L = \{L_i(g_j)\}_{i,j=1}^{N_p}$ can be written as:

$$L = \begin{bmatrix}
1 & x_1 & y_1 & x_1^2 & x_1y_1 & \cdots & x_1y_1^5 & y_1^6 \\
0 & 1 & 0 & 2x_1 & y_1 & \cdots & y_1^5 & 0 \\
0 & 0 & 1 & 0 & x_1 & \cdots & 5x_1y_1^4 & 6y_1^5 \\
0 & 0 & 0 & 2 & 0 & \cdots & 0 & 0 \\
0 & 0 & 0 & 0 & 0 & \cdots & 20x_1y_1^3 & 30y_1^4 \\
0 & 0 & 0 & 0 & 1 & \cdots & 5y_1^4 & 0 \\
0 & n_x^1 & n_y^1 & 2n_x^1x_4 & n_x^1y_4 + n_y^1x_4 & \cdots & n_x^1y_4^5 + 5n_y^1x_4y_4^4 & 6n_y^1y_4^5 \\
1 & x_5 & y_5 & x_5^2 & x_5y_5 & \cdots & x_5y_5^5 & y_5^6 \\
0 & n_x^1 & n_y^1 & 2n_x^1x_6 & n_x^1y_6 + n_y^1x_6 & \cdots & n_x^1y_6^5 + 5n_y^1x_6y_6^4 & 6n_y^1y_6^5 \\
\vdots & \vdots & \vdots & \vdots & \vdots & \ddots & \vdots & \vdots \\
1 & x_{11} & y_{11} & x_{11}^2 & x_{11}y_{11} & \cdots & x_{11}y_{11}^5 & y_{11}^6 \\
0 & n_x^3 & n_y^3 & 2n_x^3x_{12} & n_x^3y_{12} + n_y^3x_{12} & \cdots & n_x^3y_{12}^5 + 5n_y^3x_{12}y_{12}^4 & 6n_y^3y_{12}^5 \\
1 & x_{13} & y_{13} & x_{13}^2 & x_{13}y_{13} & \cdots & x_{13}y_{13}^5 & y_{13}^6
\end{bmatrix}$$

Resulting in the shape functions illustrated in Fig D.2.

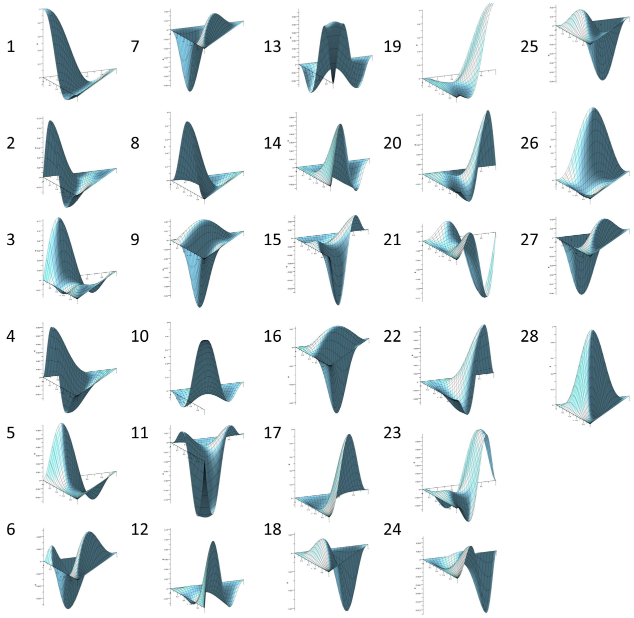

Figure D.2: Shape functions for a sixth order element.

Bibliography

[1] M Sutton, J Orteu, and H Schreier. *Image Correlation for Shape, Motion and Deformation Measurements.* Springer, 2009.

[2] B Szabo and I Babuska. *Finite Element Analysis.* Jhon Wiley & Sons, Inc, 1991.

[3] O.C Zienkiewicz and R.L Taylor. *The finite element method. Volume 1: The basis.* 2000.

[4] M Sutton, J.H Yan, V. Tiwari, H Schreier, and J Orteu. The effect of out-of-plane motion on 2d and 3d digital image correlation measurements. *Optics and Lasers in Engineering*, 46:746–757, 2008.

[5] B Pan, L yu, and D. Wu. High-accuracy 2d digital image correlation measurements with bilateral telecentric lens: error analysis and experimental verification. *Experimental Mechanics*, 53:1719 – 1752, 2013.

[6] P lava, W Van Paepegem, S Coppieters, De Baere I, Y Wang, and D Debruyne. Impact of lens distortions on strain measurements obtained with 2d digital image correlation. *Optics and Lasers in Engineering*, 51:576–584, 2013.

[7] P Zhou and K.E. Goodson. Subpixel displacement and deformation gradient measurement using digital image/speckle correlation. *Opt. Eng.*, 40:1613–20, 2001.

[8] M. Sjodahl and L.R. Benckert. Electronic speckle photography: analysis of an algorithm giving the displacement with subpixel accuracy. *Appl. Opt.*, 32:2278–84, 1993.

[9] MatchID. *MatchID 2D Software.* http://www.matchid.org.

[10] Dantec Dynamics. *Dantec DIC.*

[11] GOM optical measuring techniques. *Aramis 2D Software.* http://www.gom.com/EN/index.html.

[12] Correlated solutions Inc. *Vic-2D Software.* http://www.correlatedsolutions.com.

[13] LaVision. *Davis Software.* http://www.lavision.de/en/products/davis.php.

[14] W Tong. An evaluation of digital image correlation criteria for strain mapping applications. *Strain*, 41:167–175, 2005.

[15] B Pan. Recent progress in digital image correlation. *Experimental Mechanics*, 51:1223–1235, 2010.

[16] H Bruck, S. McNeill, M Sutton, and W. Peters. Digital image correlation using newton-raphson method for partial differential correction. *Experimental Mechanics*, 29:261–267, 1989.

[17] H Lu and P Cary. Deformation measurements by digital image correlation: Implementation of a second order deformation gradient. *Experimental Mechanics*, 40:393–400, 2000.

[18] P Lava, S Cooreman, and D Debruyne. Study of systematic errors in strain fields obtained via dic using heterogeneous deformation generated by plastic fea. *Opt. Las. Eng*, 48:457–468, 2010.

[19] B Pan, A Asundi, H Xie, and J Gao. Digital image correlation using iterative least squares and point wise least squares for displacement field and strain field measurements. *Optics and lasers in Engineering*, 45:865–874, 2009.

[20] B Pan, K Qian, H Xie, and A Asundi. Two-dimensional digital image correlation for in-plane displacement and strain measurement: a review. *Measurement Science and Technology*, 20:17, 2008.

[21] P Cheng, M.A Sutton, H.W Schreier, and S.R McNeill. Full-field speckle pattern image correlation with b-spline defromation function. *Experimental Mechanics*, 42:344–352, 2002.

[22] G Besnard, F Hild, and F. Hild. "finite-element" displacement field analysis from digital images. *Experimental Mechanics*, 46:789–803, 2006.

[23] O.C Zienkiewicz. Adaptivity and mesh generation. *International Journal for Numerical Methods in Engineering*, 32:783–810, 1991.

[24] Z.Y Wang, H.Q. Li, W Tong, and J.T. Ruan. Statistical analysis of the effect of intensity pattern noise on the displacement measurement precision of digital image correlation using self-correlated images. *Experimental Mechanics*, 47:701–707, 2007.

[25] F Hild, S Roux, R Gras, N Guerrero, M.E Marante, and J Florez-Lopezc. Displacement measurement technique for beam kinematics. *Optics and Lasers in Engineering*, 47:495–503, 2009.

[26] H Leclerc, J Perie, S Roux, and F Hild. Integrated digital image correlation for the identification of mechanical properties. *Computer Vision/Computer Graphics CollaborationTechniques*, 5496:161–171, 2009.

[27] M Langerholc, J Slavic, and Boltezar M. Absolute nodal coordinates in digital image correlation. *Experimental Mechanics*, 53:807–818, 2012.

[28] J Rethore, F Hild, and S Roux. Extended digital image correlation with crack shape optimization. *International Journal for Numerical Methods in Engineering*, 73:248–272, 2008.

[29] H Schreier, J Braasch, and M Sutton. Systematic errors in digital image correlation caused by intensity interpolation. *Optical Engineering*, 39:2915–2921, 2000.

[30] P Lava, S Cooreman, S Coppieters, M De Strycker, and D Debruyne. Assessment of measuring errors in dic using deformation fields generated by plastic fea. *Opt. Las. Eng.*, 47:747–753, 2009.

[31] H Schreier and M Sutton. Systematic errors in digital image correlation due to undermaunder subset shape functions. *JSME International Journal Series A*, 30:62–67, 2009.

[32] B Pan. Study on subset size selection in digital image correlation for speckle patterns. *Optics Express*, 16:7037–7048, 2008.

[33] S Yaofeng and J.H.L. Pang. Study of optimal subset size in digital image correlation of speckle pattern images. *Optics and Lasers in Engineering*, page DOI: 10.1016/j.optlaseng.2007.01.012, 2007.

[34] Y Wang, P Lava, S Coppieters, M De Strycker, P Van Houtte, and D Debruyne. Investigation of the uncertainty of dic under heterogeneous strain states with numerical tests. *Strain*, 48(6):453–62, 2012.

[35] Y Wang, M Sutton, H Bruck, and H Schreier. Quantitative error assessment in pattern matching: Effects of intensity pattern noise, interpolation, strain and image contrast on motion measurements. *Strain*, 45(2):160–178, 2009.

[36] S Yoneyama, H Kikuta, A Kitagawa, and K Kitamura. Lens distortion correction for digital image correlation by measuring rigid body displacements. *Optical Engineering*, 45, 2006.

[37] S Yoneyama, A Kitagawa, Kitamura K, and H kikuta. In-plane displacement measurement using digital image correlation with lens distortion correction. *JSME International Journal Series A*, 49:458–467, 2007.

[38] D.S. Zhang, M Luo, and D Arola. Displacement/strain measurements using an optical microscope and digital image correlation. *Optical Engineering*, 45, 2006.

[39] M Sutton, N. Li, D Garcia, N Cornille, J.J Orteu, S. McNeill, H Schreier, and X. Li. Metrology in a scanning electron microscope: theoretical developments and experimental validation. *Measurement Science and Technology*, 17, 2006.

[40] M Sutton, N. Li, D.C Joy, A.P. Reynolds, and X. Li. Scanning electron microscopy for quantitative small and large deformation measurements. part i. *Experimental Mechanics*, 47:775–787, 2007.

[41] M Sutton, N. Li, D.C Joy, A.P. Reynolds, and X. Li. Scanning electron microscopy for quantitative small and large deformation measurements. part i. *Experimental Mechanics*, 47:789–804, 2007.

[42] B Pan, L Yu, and D. Wu. High-accuracy 2d digital image correlation measurements using low-cost imaging lenses: implementation of a generalized compensation method. *Measurement Science and Technology*, 25, 2014.

[43] D. Lecompte, A. Smits, S. Bossuyt, H. Sol, J. Vantomme, D Van Hemelrijck, and A.M. Habraken. Quality assessment of speckle ppattern dor digital image correlation. *Optics and Lasers in Engineering*, 44:1132–1145, 2006.

[44] Evaluation of measurement data - guide to the expression of uncertainty in measurement jcgm 100:2008.

[45] J Abanto Bueno and J Lambros. Investigation of crack growth in functionally graded materials using digital image correlation. *Eng. Fract. Mech.*, 69:1695–711, 2002.

[46] J Perie, S Calloch, C Cluzel, and F Hild. Analysis of a multiaxial test on a c/c composite by using digital image correlation and a damage model. *Experimental Mechanics*, 42(3):318–328, 2002.

[47] L Chevalier, S Calloch, F Hild, and Y Marco. Digital image correlation used to analyze the multiaxial behavior of rubber-like materials. *European Journal of Mechanics*, 20(2):169–187, 2001.

[48] Chian. Micro-/nano-speckle method with applications to materials, tissue engineering and heart mechanics. *Experimental Analysis of Nano and Engineering Materials and Structures*, pages 7–8, 2007.

[49] G Vanoppen. 3d shape reconstructie: Digital image correlation vs. mycrona signum ha. Master's thesis, University of Leuven, 2013.

[50] A Dickinson, A Taylor, H Ozturk, and H Browne. Experimental validation of a finite element model of the proximal femur using digital image correlation and a composite bone model. *J Biomech Eng*, 133(1):014504, 2010.

[51] J.M. Considine, F Pierron, K.T. Turner, and D.W. Vahey. General anisotropy identification of paperboard with virtual fields method. *Experimental Mechanics*, 54(8):1395–1410, 2014.

[52] J Xavier, S Avril, F Pierron, and J Morais. Novel experimental approach for longitudinal-radial stiffness characterisation of clear wood by a single test. *Holzforschung*, 61(5):573–581, 2007.

[53] P. Wang, F Pierron, and O.T. Thomsen. Identification of material parameters of pvc foams using digital image correlation and the virtual fields method. *Experimental Mechanics*, 53(6):1001–1015, 2012.

[54] R..H. Pritchard, P Lava, D Debruyne, and E.M Terentjev. Precise determination of the poisson ratio in soft materials with 2d digital image correlation. *Soft Matter*, 9:6037–6045, 2013.

[55] S Cooreman. *Identification of the plastic material behaviour through full-field displacement measurements and inverse methods.* PhD thesis, University of Brussels (VUB), 2008.

[56] F Pierron and M Grediac. *The Virtual Fields Method: Extracting Constitutive Mechanical Parameters from Full-field Deformation Measurements.* Springer, 2012.

[57] B. Szabo and I. Babuska. *Finite element.* Jhon Wiley & Sons, 1991.

[58] F Hild and S Roux. Comparison of local and global approaches to digital image correlation. *Experimental Mechanics*, 52:1503–1519, 2011.

[59] F Mortazavi. *Development of a global digital image correlation approach for fast high-resolution displacement measurements.* PhD thesis, ECOLE POLYTECHNIQUE DE MONTREAL, 2013.

[60] I Babuska, J.R. Whiteman, and T Strouboulis. *Finite Elements. An introduction to the method and error estimation.* Oxford university press, 2011.

[61] J.E. Akin. *Finite element analysis. With error estimators.* Elsivier, 2005.

[62] B Szabo, A. Duster, and E Rank. The p-version of the finite element method. *Encyclopedia of Computational Mechanics*, 2004.

[63] H. Chongy. An inverse transformation for quadrilateral isoparametric elements. *Finite Elements in Analysis and Design*, 7(2):159–166, 1990.

[64] T Gratsch and K.J Bathe. A posteriori error estimation techniques in practical finite element analysis. *Computers and Structures*, 83:235–265, 2003.

[65] O.C Zienkiewicz and J.Z Zhu. The superconvergent patch recovery and a posteriori error estimates. *International Journal for Numerical Methods in Engineering*, 33(7):1331–1364, 1992.

[66] O.C Zienkiewicz, J.Z Zhu, and N.G Gong. Effective and practical h-p-version adaptive analysis procedures for the finite element method. *International Journal for Numerical Methods in Engineering*, 25(4):879–891, 1989.

[67] PTCUniversity. The h- and p-versions of finte elements. 2012.

[68] A Promwungkwa. *Data structure and error estimation for an Adaptive p-Version.* PhD thesis, State University Verginia, 1998.

[69] A Chrysochoos and Y Surrel. *Chapter 1. Basics of metrology and introduction to techniques.* Wiley, 2012.

[70] M Bornert, F Bremand, P Doumalin, J.C Dupre, M Fazzini, M Grediac, F Hild, S Roux, S Mistou, J Molimard, J.J Orteu, L Robert, P Surrel, Yand Vacher, and B Wattrisse. Assessment of digital image correlation measurement errors: Methodology and results. *Experimental Mechanics*, 49:353–370, 2009.

[71] M Grediac and F Sur. Effect of sensor noise on the resolution and spatial resolution of displacement and strain maps estimated with the grid method. *Strain*, 50(1):1–27, 2014.

[72] *ISO/IEC guide 99 - International vocabulary of metrology – Basic and general concepts and associated terms (VIM).* ISO, 2007.

[73] M Rossi, P Lava, F Pierron, D Debruyne, and M Sasso. Error assessment on combining dic and vfm to design an optimized experimental set-up for material identification. *Acceted - Strain*, 2015.

[74] S Avril, M Bonnet, A Bretelle, M Grediac, F Hild, P Ienny, F Latourte, D Lemosse, S Pagano, E Pagnacco, and F Pierron. Overview of identification methods of mechanical parameters based on full-field measurements. *Experimental Mechanics*, 48:381–402, 2008.

[75] T Kanade and M Okutomi. A stereo matching algorithm with an adaptive window: Theory and experiment. *TPAMI*, 16:920–9322, 1994.

[76] A Fusiello and V Roberto. Efficient stereo with multiple windowing. *CVPR*, pages 858–863, 1997.

[77] D Geiger, B Ladendorf, and A Yuille. Occlusions and binocular stereo. *IJCV*, 14:211–226, 1995.

[78] S Intille and A Bobick. Disparity-space images and large occlusion stereo. *ECCV94*, pages 179–186, 1994.

[79] S Kang, R Szeliski, and J Chai. Handeling occlusions in dense multi stereo view. *CVPR01*, pages 103–110, 2001.

[80] L Wittevrongel, P Lava, S.V. Lomov, and D Debruyne. A self adaptive global digital image correlation algorithm. *Experimental Mechanics*, pages DOI 10.1007/s11340–014–9946–3, 2014.

[81] K.J. Bathe. *Finite element procedures.* Asoke K. Ghosh, Prentice-Hall of India, 1996.

[82] S.M. Kleinendorst, J.P.M. Hoefnagels, C.V. Verhoosel, and A.P. Ruybalid. On the use of adaptive refinement in isogeometric digitalimage correlation. *Experimental Mechanics*, page DOI: 10.1002/nme.4952, 2015.

[83] Paval Solin. *Partial Differential Equations and the Finite Element Method.* John Wiley & Sons, 2006.

[84] S.-A. Papanicolopulos. Polynomial c1 shape functions on the triangle. *Computers and Structures*, 118:53–58, 2013.

[85] M.M. Hrabok and T.M. Hrudey. A review and cataloque of plate bending finite elements. *Computers and structures*, 19:479–495, 1984.

[86] SC. Jardin. A tirangular finite element with first-derivative continuity applied to fusion mhd applicaitons.

[87] P K Rastogi. *Photomechanics: Topics in applied physics.* Springer, 2000.

[88] M Rossi, P Lava, F Pierron, D Debruyne, and M Sasso. Effect of dic spatial resolution, noise and interpolation error on identification results with the vfm. *Strain Accepted*, 2015.

[89] Ma Qinwai and MA Shaopeng. Experimental investigation of th systematic error in photomechanics methods induced by camera self-heating. *Optics Express*, 6:7686, 2013.

[90] P Lava, S Coppieters, Y wang, P Van Houtte, and D Debruyne. Error estimation in measuring strain fields with dic on planar sheet metal specimens with a non-perpendicular camera alignment. *Optics and Lasers in Engineering*, 49:57–65, 2011.

[91] B Pan, L yu, D. wu, and L.Q. Tang. systematic errors in two-dimensional digital image correlation due to lens distortions. *Optics and Lasers in Engineering*, 52(2):140–147, 2013.

Curriculum Vitae

D.1 Personal

Name: Lukas Wittevrongel
Date of birth: 18-08-1990
Place of birth: Ghent, Belgium
Citizenship: Belgium

D.2 Education

2012-2013: Postgraduate program in Experimental Mechanics, University of Southampton, Summa cum laude
2011-2012: Master of Science in Industrial science: Electromechanics, KAHO Sint-Lieven Ghent, Summa cum laude
2008-2011: Bachelor of Science in Industrial science: Electromechanics, KAHO Sint-Lieven Ghent, Magna cum laude

D.3 Publications Peer Reviewed Journals

1. Wittevrongel L., Lava P., Lomov S.V. and Debruyne D. A Self Adaptive Digital Image Correlation Algorithm. *Experimental Mechanics,* 55(2): 361-378, 2015

2. Wittevrongel L., Debruyne D., Lomov S.V. and Lava P. Implementation of Convergence in Adaptive Global Digital Image Correlation. *Experimental Mechanics, submitted,* 2015

3. Wittevrongel L., Lava P., Lomov S.V. and Debruyne D. C^n continuity in Digital Image Correlation: Implementation and validation of C^{-1}, C^0 and C^1 algorithms. *Strain,* Published online DOI: 10.1111/str.12146, 2015

4. Wittevrongel L., Badaloni M., Balcaen R., Lava P. and Debruyne D. Evaluation of methodologies for compensation of out of plane motions in a 2D Digital image correlation set-up. *Strain,* 51(5): 357-369, 2015

D.4 Conference proceedings and abstracts

1. Wittevrongel L., Lava P., Debruyne D. and Lomov S.V. An adaptive DIC algorithm for measuring small strains in composites. *International Conference on Experiment Mechanics ICEM16, United Kingdom, Cambridge,* 7-11 July 2014

2. Wittevrongel L., Lava P., Debruyne D. and Lomov S.V. P-Adaptivity in Digital Image Correlation. *Young Stress Analyst Competition 2015 YSA14, United Kingdom, Cambridge,* 7-11 July 2014

3. Wittevrongel L., Lava P., Debruyne D. and Lomov S.V. Automatic Mesh Refinement In Global Digital Image Correlation. *Photomechanics, Netherlands, Delft,* 27-29 May 2015

4. Wittevrongel L., Lava P., Debruyne D. and Lomov S.V. Towards the development of a global Cn-continuous DIC procedure? *Annual Conference and Exposition on Experimental and Applied Mechanics SEM15, United States, Costa-Mesa,* 8-11 July 2015

5. Wittevrongel L, Lava P, Debruyne D and Lomov S.V. Local or global DIC: noise robustness versus spatial resolution. *Student Paper Competion SEM15 Annual Conference and Exposition on Experimental and Applied Mechanics, United States, Costa-Mesa,* 8-11 July 2015

6. Lava P., Wittevrongel L., Debruyne D. and Pierron F. Quantification of Resolution and Spatial Resolution in Local and Global DIC. *Annual Conference and Exposition on Experimental and Applied Mechanics SEM15, United States, Costa-Mesa,* 8-11 July 2015

7. Wittevrongel L., Lava P., Debruyne D. and Lomov S.V. Cn continuity in Digital Image Correlation. *10th International Conference on Advances in Experimental Mechanics BSSM15, United Kingdom, Edinbrough,* 1-3 September 2015

FACULTY OF ENGINEERING TECHNOLOGY
DEPARTMENT OF METALLURGY AND MATERIALS ENGINEERING
MECHANICS OF MATERIALS, PRODUCTS AND PROCESSES
Gebroerders Desmetstraat 1
B-9000 Ghent
lukas.wittevrongel@kuleuven.be
http://iiw.kuleuven.be/onderzoek/mem2p